

**GRB 221009A: The B.O.A.T. Burst that Shines in Gamma Rays**

M. Axelsson^{1,2,92} , M. Ajello³ , M. Arimoto⁴ , L. Baldini⁵ , J. Ballet⁶ , M. G. Baring⁷ , C. Bartolini^{8,9} ,
D. Bastieri^{10,11,12} , J. Becerra Gonzalez¹³ , R. Bellazzini¹⁴ , B. Berenji¹⁵ , E. Bissaldi^{8,16,91} , R. D. Blandford¹⁷ ,
R. Bonino^{18,19} , P. Bruehl^{20,91} , S. Buson²¹ , R. A. Cameron¹⁷ , R. Caputo²² , P. A. Caraveo²³ , E. Cavazzuti²⁴ ,
C. C. Cheung²⁵ , G. Chiaro²³ , N. Cibrario^{18,19} , S. Ciprini^{26,27} , G. Cozzolongo^{28,29} , P. Cristarella Orestano^{30,31} ,
M. Crnogorčević^{22,32} , A. Cuoco^{18,19} , S. Cutini³¹ , F. D'Ammando³³ , S. De Gaetano^{8,16} , N. Di Lalla^{17,91} , A. Dinesh³⁴ ,
R. Di Tria¹⁶ , L. Di Venere⁸ , A. Domínguez³⁴ , S. J. Fegan²⁰ , E. C. Ferrara^{22,32,35} , A. Fiori⁵ , A. Franckowiak³⁶ ,
Y. Fukazawa³⁷ , S. Funk²⁸ , P. Fusco^{8,16} , G. Galanti²³ , F. Gargano⁸ , C. Gasbarra^{26,38} , S. Germani^{31,39} ,
F. Giacchino^{26,27} , N. Giglietto^{8,16} , M. Giliberti^{8,16} , R. Gill^{40,41} , F. Giordano^{8,16} , M. Giroletti³³ , J. Granot^{41,42,43} ,
D. Green⁴⁴ , I. A. Grenier⁴⁵ , S. Guiriec^{22,43} , M. Gustafsson⁴⁶ , M. Hashizume³⁷ , E. Hays²² , J. W. Hewitt⁴⁷ ,
D. Horan²⁰ , T. Kayanoki³⁷ , M. Kuss¹⁴ , A. Laviron²⁰ , J. Li^{48,49} , I. Liodakis⁵⁰ , F. Longo^{51,52} , F. Loparco^{8,16} ,
L. Lorusso^{8,16} , B. Lott⁵³ , M. N. Lovellette⁵⁴ , P. Lubrano³¹ , S. Maldera¹⁸ , D. Malyshev²⁸ , A. Manfreda⁵ ,
G. Martí-Devesa⁵¹ , R. Martinelli⁵¹ , I. Martínez Castellanos^{22,32,35} , M. N. Mazziotta⁸ , J. E. McEnery^{22,32} , I. Mereu^{30,31} ,
M. Meyer⁵⁵ , P. F. Michelson¹⁷ , N. Mirabal^{22,56} , W. Mitthumsiri⁵⁷ , T. Mizuno⁵⁸ , P. Monti-Guarnieri^{51,52} ,
M. E. Monzani^{17,59} , T. Morishita³⁷ , A. Morselli²⁶ , I. V. Moskalenko¹⁷ , M. Negro⁶⁰ , R. Niwa³⁷ , N. Omodei^{17,91} ,
M. Orienti³³ , E. Orlando^{17,61} , D. Paneque⁴⁴ , G. Panzarini^{8,16} , M. Persic^{52,62} , M. Pesce-Rollins¹⁴ , V. Petrosian¹⁷ ,
R. Pilleri^{8,16,91} , F. Piron⁶³ , T. A. Porter¹⁷ , G. Principe^{33,51,52} , J. L. Racusin²² , S. Rainò^{8,16} , R. Rando^{10,11,12} ,
B. Rani^{22,56} , M. Razzano⁵ , S. Razzaque^{43,64} , A. Reimer⁶⁵ , O. Reimer⁶⁵ , F. Ryde^{1,2} , M. Sánchez-Conde^{66,67} ,
P. M. Saz Parkinson⁶⁸ , D. Serini⁸ , C. Sgrò¹⁴ , V. Sharma^{22,35,56} , E. J. Siskind⁶⁹ , G. Spandre¹⁴ , P. Spinelli^{8,16} ,
D. J. Suson⁷⁰ , H. Tajima^{71,72} , D. Tak⁷³ , J. B. Thayer¹⁷ , D. F. Torres^{74,75,76} , J. Valverde^{22,56} , G. Zaharijas⁷⁷ ,
(Fermi LAT collaboration)

and

S. Lesage^{78,79} , M. S. Briggs^{78,79} , E. Burns⁸⁰ , S. Bala⁸¹ , P. N. Bhat⁷⁹ , W. H. Cleveland⁸¹ , S. Dalesi^{78,82} ,
C. de Barra⁸³ , M. Gibby⁸⁴ , M. M. Giles⁸⁴ , R. Hamburg⁸⁵ , B. A. Hristov⁸² , D. Kocevski⁸⁶ , C. M. Hui⁸⁶ , B. Mailyan⁸⁷ ,
C. Malacaria⁸⁸ , S. McBreen⁸³ , S. Poolakkil^{79,89} , O. J. Roberts⁸¹ , L. Scotton^{78,79} , P. Veres^{79,89} , A. von Kienlin⁹⁰ ,
C. A. Wilson-Hodge⁸⁶ , and J. Wood⁸⁶

(Fermi GBM collaboration)

¹ Department of Physics, KTH Royal Institute of Technology, AlbaNova, SE-106 91 Stockholm, Sweden² The Oskar Klein Centre for Cosmoparticle Physics, AlbaNova, SE-106 91 Stockholm, Sweden³ Department of Physics and Astronomy, Clemson University, Kinard Lab of Physics, Clemson, SC 29634-0978, USA⁴ Faculty of Mathematics and Physics, Institute of Science and Engineering, Kanazawa University, Kakuma, Kanazawa, Ishikawa 920-1192, Japan⁵ Università di Pisa and Istituto Nazionale di Fisica Nucleare, Sezione di Pisa I-56127 Pisa, Italy⁶ Université Paris-Saclay, Université Paris Cité, CEA, CNRS, AIM, F-91191 Gif-sur-Yvette Cedex, France⁷ Rice University, Department of Physics and Astronomy, MS-108, P. O. Box 1892, Houston, TX 77251, USA⁸ Istituto Nazionale di Fisica Nucleare, Sezione di Bari, I-70126 Bari, Italy⁹ Università degli studi di Trento, via Calepina 14, 38122 Trento, Italy¹⁰ Istituto Nazionale di Fisica Nucleare, Sezione di Padova, I-35131 Padova, Italy¹¹ Dipartimento di Fisica e Astronomia "G. Galilei," Università di Padova, Via F. Marzolo, 8, I-35131 Padova, Italy¹² Center for Space Studies and Activities "G. Colombo," University of Padova, Via Venezia 15, I-35131 Padova, Italy¹³ Instituto de Astrofísica de Canarias and Universidad de La Laguna, Dpto. Astrofísica, 38200 La Laguna, Tenerife, Spain¹⁴ Istituto Nazionale di Fisica Nucleare, Sezione di Pisa, I-56127 Pisa, Italy¹⁵ California State University, Los Angeles, Department of Physics and Astronomy, Los Angeles, CA 90032, USA¹⁶ Dipartimento di Fisica "M. Merlin" dell'Università e del Politecnico di Bari, via Amendola 173, I-70126 Bari, Italy¹⁷ W. W. Hansen Experimental Physics Laboratory, Kavli Institute for Particle Astrophysics and Cosmology, Department of Physics and SLAC National Accelerator Laboratory, Stanford University, Stanford, CA 94305, USA¹⁸ Istituto Nazionale di Fisica Nucleare, Sezione di Torino, I-10125 Torino, Italy¹⁹ Dipartimento di Fisica, Università degli Studi di Torino, I-10125 Torino, Italy²⁰ Laboratoire Leprince-Ringuet, CNRS/IN2P3, École polytechnique, Institut Polytechnique de Paris, 91120 Palaiseau, France²¹ Institut für Theoretische Physik und Astrophysik, Universität Würzburg, D-97074 Würzburg, Germany²² Astrophysics Science Division, NASA Goddard Space Flight Center, Greenbelt, MD 20771, USA²³ INFN-Istituto di Astrofisica Spaziale e Fisica Cosmica Milano, via E. Bassini 15, I-20133 Milano, Italy²⁴ Italian Space Agency, Via del Politecnico snc, 00133 Roma, Italy²⁵ Space Science Division, Naval Research Laboratory, Washington, DC 20375-5352, USA²⁶ Istituto Nazionale di Fisica Nucleare, Sezione di Roma "Tor Vergata," I-00133 Roma, Italy²⁷ Space Science Data Center - Agenzia Spaziale Italiana, Via del Politecnico, snc, I-00133, Roma, Italy²⁸ Friedrich-Alexander Universität Erlangen-Nürnberg, Erlangen Centre for Astroparticle Physics, Erwin-Rommel-Str. 1, 91058 Erlangen, Germany²⁹ Friedrich-Alexander-Universität, Erlangen-Nürnberg, Schlossplatz 4, 91054 Erlangen, Germany³⁰ Dipartimento di Fisica, Università degli Studi di Perugia, I-06123 Perugia, Italy³¹ Istituto Nazionale di Fisica Nucleare, Sezione di Perugia, I-06123 Perugia, Italy³² Department of Astronomy, University of Maryland, College Park, MD 20742, USA³³ INFN Istituto di Radioastronomia, I-40129 Bologna, Italy³⁴ Grupo de Altas Energías, Universidad Complutense de Madrid, E-28040 Madrid, Spain³⁵ Center for Research and Exploration in Space Science and Technology, NASA/GSFC, Greenbelt, MD 20771, USA³⁶ Ruhr University Bochum, Faculty of Physics and Astronomy, Astronomical Institute (AIRUB), 44780 Bochum, Germany

- ³⁷ Department of Physical Sciences, Hiroshima University, Higashi-Hiroshima, Hiroshima 739-8526, Japan
³⁸ Dipartimento di Fisica, Università di Roma "Tor Vergata," I-00133 Roma, Italy
³⁹ Dipartimento di Fisica e Geologia, Università degli Studi di Perugia, via Pascoli snc, I-06123 Perugia, Italy
⁴⁰ Instituto de Radioastronomía y Astrofísica, Universidad Nacional Autónoma de México, Antigua Carretera a Pátzcuaro #8701, Ex-Hda, San José de la Huerta, Morelia, Michoacán, México C.P. 58089, Mexico
⁴¹ Astrophysics Research Center of the Open university (ARCO), The Open University of Israel, P.O Box 808, Ra'anana 43537, Israel
⁴² Department of Natural Sciences, Open University of Israel, 1 University Road, POB 808, Ra'anana 43537, Israel
⁴³ The George Washington University, Department of Physics, 725 21st Street NW, Washington, DC 20052, USA
⁴⁴ Max-Planck-Institut für Physik, D-80805 München, Germany
⁴⁵ Université Paris Cité, Université Paris-Saclay, CEA, CNRS, AIM, F-91191 Gif-sur-Yvette, France
⁴⁶ Georg-August University Göttingen, Institute for theoretical Physics - Faculty of Physics, Friedrich-Hund-Platz 1, D-37077 Göttingen, Germany
⁴⁷ University of North Florida, Department of Physics, 1 UNF Drive, Jacksonville, FL 32224, USA
⁴⁸ CAS Key Laboratory for Research in Galaxies and Cosmology, Department of Astronomy, University of Science and Technology of China, Hefei 230026, People's Republic of China
⁴⁹ School of Astronomy and Space Science, University of Science and Technology of China, Hefei 230026, People's Republic of China
⁵⁰ NASA Marshall Space Flight Center, Huntsville, AL 35812, USA
⁵¹ Dipartimento di Fisica, Università di Trieste, I-34127 Trieste, Italy
⁵² Istituto Nazionale di Fisica Nucleare, Sezione di Trieste, I-34127 Trieste, Italy
⁵³ Université Bordeaux, CNRS, LP2I Bordeaux, UMR 5797, F-33170 Gradignan, France
⁵⁴ The Aerospace Corporation, 14745 Lee Road, Chantilly, VA 20151, USA
⁵⁵ Center for Cosmology and Particle Physics Phenomenology, University of Southern Denmark, Campusvej 55, DK-5230 Odense M, Denmark
⁵⁶ Center for Space Science and Technology, University of Maryland Baltimore County, 1000 Hilltop Circle, Baltimore, MD 21250, USA
⁵⁷ Department of Physics, Faculty of Science, Mahidol University, Bangkok 10400, Thailand
⁵⁸ Hiroshima Astrophysical Science Center, Hiroshima University, Higashi-Hiroshima, Hiroshima 739-8526, Japan
⁵⁹ Vatican Observatory, Castel Gandolfo, V-00120, Vatican City State
⁶⁰ Department of physics and Astronomy, Louisiana State University, Baton Rouge, LA 70803, USA
⁶¹ Istituto Nazionale di Fisica Nucleare, Sezione di Trieste, and Università di Trieste, I-34127 Trieste, Italy
⁶² INFN-Astronomical Observatory of Padova, Vicolo dell'Osservatorio 5, I-35122 Padova, Italy
⁶³ Laboratoire Univers et Particules de Montpellier, Université Montpellier, CNRS/IN2P3, F-34095 Montpellier, France
⁶⁴ Centre for Astro-Particle Physics (CAPP) and Department of Physics, University of Johannesburg, PO Box 524, Auckland Park 2006, South Africa
⁶⁵ Institut für Astro- und Teilchenphysik, Leopold-Franzens-Universität Innsbruck, A-6020 Innsbruck, Austria
⁶⁶ Instituto de Física Teórica UAM/CSIC, Universidad Autónoma de Madrid, E-28049 Madrid, Spain
⁶⁷ Departamento de Física Teórica, Universidad Autónoma de Madrid, 28049 Madrid, Spain
⁶⁸ Santa Cruz Institute for Particle Physics, Department of Physics and Department of Astronomy and Astrophysics, University of California at Santa Cruz, Santa Cruz, CA 95064, USA
⁶⁹ NYCB Real-Time Computing Inc., Lattingtown, NY 11560-1025, USA
⁷⁰ Purdue University Northwest, Hammond, IN 46323, USA
⁷¹ Nagoya University, Institute for Space-Earth Environmental Research, Furo-cho, Chikusa-ku, Nagoya 464-8601, Japan
⁷² Kobayashi-Maskawa Institute for the Origin of Particles and the Universe, Nagoya University, Furo-cho, Chikusa-ku, Nagoya, Japan
⁷³ SNU Astronomy Research Center, Seoul National University, Gwanak-ro, Gwanak-gu, Seoul, Korea
⁷⁴ Institute of Space Sciences (ICE, CSIC), Campus UAB, Carrer de Magrans s/n, E-08193 Barcelona, Spain
⁷⁵ Institució Catalana de Recerca i Estudis Avançats (ICREA), E-08010 Barcelona, Spain
⁷⁶ Institut d'Estudis Espacials de Catalunya (IEEC), E-08034 Barcelona, Spain
⁷⁷ Center for Astrophysics and Cosmology, University of Nova Gorica, Nova Gorica, Slovenia
⁷⁸ Department of Space Science, University of Alabama in Huntsville, 320 Sparkman Drive, Huntsville, AL 35899, USA
⁷⁹ Center for Space Plasma and Aeronomic Research, University of Alabama in Huntsville, Huntsville, AL 35899, USA
⁸⁰ Department of Physics & Astronomy, Louisiana State University, Baton Rouge, LA 70803, USA
⁸¹ Science and Technology Institute, Universities Space Research Association, Huntsville, AL 35805, USA
⁸² Center for Space Plasma and Aeronomic Research, University of Alabama in Huntsville, 320 Sparkman Drive, Huntsville, AL 35899, USA
⁸³ School of Physics, University College Dublin, Belfield, Dublin, Ireland
⁸⁴ Jacobs Space Exploration Group, Huntsville, AL 35806, USA
⁸⁵ Université Paris-Saclay, CNRS/IN2P3, IJCLab, 91405 Orsay, France
⁸⁶ ST12 Astrophysics Branch, NASA Marshall Space Flight Center, Huntsville, AL 35812, USA
⁸⁷ Department of Aerospace, Physics and Space Sciences, Florida Institute of Technology, Melbourne, FL 32901, USA
⁸⁸ International Space Science Institute, Hallerstrasse 6, 3012 Bern, Switzerland
⁸⁹ Department of Space Science, University of Alabama in Huntsville, Huntsville, AL 35899, USA
⁹⁰ Max-Planck-Institut für extraterrestrische Physik, Giessenbachstrasse 1, D-85748 Garching, Germany

Received 2024 August 26; revised 2024 December 18; accepted 2024 December 22; published 2025 February 28

Abstract

We present a complete analysis of Fermi Large Area Telescope (LAT) data of GRB 221009A, the brightest gamma-ray burst (GRB) ever detected. The burst emission above 30 MeV detected by the LAT preceded, by 1 s, the low-energy (<10 MeV) pulse that triggered the Fermi Gamma-Ray Burst Monitor (GBM), as has been observed in other GRBs. The prompt phase of GRB 221009A lasted a few hundred seconds. It was so bright that

⁹¹ Corresponding authors: Elisabetta Bissaldi, Philippe Bruel, Niccolò Di Lalla, Nicola Omodei, Roberta Pillera.

⁹² Deceased 2022 July.



we identify a bad time interval of 64 s caused by the extremely high flux of hard X-rays and soft gamma rays, during which the event reconstruction efficiency was poor and the dead time fraction quite high. The late-time emission decayed as a power law, but the extrapolation of the late-time emission during the first 450 s suggests that the afterglow started during the prompt emission. We also found that high-energy events observed by the LAT are incompatible with synchrotron origin, and, during the prompt emission, are more likely related to an extra component identified as synchrotron self-Compton (SSC). A remarkable 400 GeV photon, detected by the LAT 33 ks after the GBM trigger and directionally consistent with the location of GRB 221009A, is hard to explain as a product of SSC or TeV electromagnetic cascades, and the process responsible for its origin is uncertain. Because of its proximity and energetic nature, GRB 221009A is an extremely rare event.

Unified Astronomy Thesaurus concepts: [Gamma-ray bursts \(629\)](#); [High energy astrophysics \(739\)](#); [Gamma-ray astronomy \(628\)](#)

1. Introduction

Gamma-ray bursts (GRBs) are extremely powerful events lighting up the gamma-ray sky approximately once per day, with the bulk of their emission extending from several keV to tens of MeV. They have been detected regularly since the late 1960s by many dedicated space missions, with a total of many thousands of events. The promptly emitted gamma-ray radiation on timescales of seconds is followed by a longer-lasting afterglow emission revealed at every wavelength (from radio to TeV gamma rays) on timescales extending to days, months, even years.

The Large Area Telescope (LAT; W. B. Atwood et al. 2009) on board the Fermi Gamma-ray Space Telescope, operating since 2008, opened a new window to explore GRB emission in the GeV domain, establishing important spectral and temporal properties of the high-energy (>0.1 GeV) burst emission (M. Ajello et al. 2019).

For almost a decade, GRB 130427A held many records among all LAT-detected GRBs (M. Ackermann et al. 2014), including the highest fluence ($1.3 \pm 0.2 \times 10^{-4}$ erg cm $^{-2}$ in the 0.1–100 GeV energy range), the highest-energy photon (94 GeV at $T_0 + 243$ s; with T_0 referring to the burst trigger), the largest number of >0.1 GeV photons recorded from a GRB (>600 , with 17 events above 10 GeV), and the longest high-energy duration 34.4 ± 0.3 ks (~ 10 hr). Despite its intensity and proximity at $z = 0.34$, no very-high-energy (VHE; >0.1 TeV) emission was detected by any ground-based experiment at the time. The VERITAS array reported bright moonlight conditions precluding observations at the time of trigger (E. Aliu et al. 2014), and follow-up could not be initiated until ~ 71 ks (~ 20 hr) after the onset of the burst, leading to upper limit derivations and constraints.

VHE emission was finally detected from a GRB a few years later, both at very early times (from 1–40 minutes after the GRB onset) as in the case of GRB 190114C ($z = 0.42$) observed by the MAGIC telescopes at energies 0.3 – 1 TeV (MAGIC Collaboration et al. 2019), as well as in the afterglow regime (~ 4 –10 hr after the GRB onset) for GRB 180720B ($z = 0.65$) and for GRB 190829A ($z = 0.078$), both observed by the H.E.S.S. telescopes at energies 0.1–0.44 TeV (H. Abdalla et al. 2019) and 0.18–3.3 TeV (H.E.S.S. Collaboration et al. 2021), respectively, or GRB 201216C observed by MAGIC at redshift $z = 1.1$ (H. Abe et al. 2024). All of these remarkable afterglow detections at TeV energies have been favored by the proximity of the bursts, preventing such high-energy emission from being severely attenuated by pair production against the extragalactic background light (EBL; J. D. Finke et al. 2010). Interestingly, none of these three breakthrough detections were accompanied by extraordinary MeV/GeV emission. In fact, the highest-energy photons detected by the LAT were 21 and 5 GeV for GRB 190114C and GRB 180720B, respectively, while the LAT detected no prompt or

afterglow high-energy emission in the case of GRB 190829A (F. Piron et al. 2019). The MeV emission is thought to arise mainly from synchrotron radiation of relativistic electrons in the jet plasma due to ultrarelativistic bulk motion. The same synchrotron component also likely dominates the LAT emission; however, an additional high-energy spectral component is typically needed to explain emission at energies $\gtrsim 10$ GeV that exceeds the maximum energy of synchrotron photons at late times (M. Ackermann et al. 2014; M. Ajello et al. 2020). Thus, Fermi-LAT covers the key energy band in which the transition of the GRB emission mechanism occurs.

Here we report the Fermi-LAT observation and interpretation of the highest-energy emission ever measured from a GRB. GRB 221009A is so bright that it allowed for a complete spectral and temporal analysis to be performed from keV to TeV energy from the triggering pulse to the late afterglow. For the first time, rapid spectral variability in the LAT during the prompt emission clearly revealed the simultaneous presence of the afterglow, which extended up to several TeV, with the prompt emission. The spectrum shows clear evidence of synchrotron self-Compton (SSC), and its evolution with time is presented in this paper. GRB 221009A broke many previous records, not only at high energies, but over many energy bands, quickly deserving the title of the “Brightest Of All Time,” or the “B.O.A.T.” GRB (E. Burns et al. 2023a).

This event was so strong and long-lived that it was detected by dozens of space- and ground-based observatories, caused even a sudden disturbance of the Earth’s ionosphere (P. W. Schnoor et al. 2022), and resulted in more than 120 rapid observation reports and communications on the General Coordinate Network (GCN) and via The Astronomer’s Telegram service. Over 100 publications, including the detection of gamma rays from AGILE (M. Tavani et al. 2023), discussions about X-ray polarization (M. Negro et al. 2023), radio observations (T. Laskar et al. 2023), and optical observations (M. D. Fulton et al. 2023), as well as several follow-up campaigns carried out by, e.g., VHE telescopes (F. Aharonian et al. 2023) and neutrino observatories (R. Abbasi et al. 2023), have been published to date.

The Fermi Gamma-Ray Burst Monitor (GBM) on board Fermi was the first detector to trigger on GRB 221009A on 2022 October 9, at 13:16:59.988 UT (trigger 221009553 / 687014224; S. Lesage et al. 2023). We will refer to this time as T_0 of the burst throughout the text. Unfortunately, prompt notices containing classification and localization information were not immediately distributed to the community through standard procedure due to issues in the ground segment (S. Lesage et al. 2023). Therefore, the LAT GRB pipeline, the so-called “LAT Transient Factory” (LTF; G. Vianello et al. 2015a) did not automatically receive and process this event.

About an hour after the trigger, at 14:10:17 UT ($T_0 + 3197$ s), the Swift Burst Alert Telescope (BAT) reported the detection of a very bright hard X-ray, soft X-ray, and UV/optical transient. BAT tentatively classified it as a new source called Swift J1913.1 + 1946 (S. Dichiara et al. 2022) with possible Galactic origin given the proximity (4°) to the Galactic plane. This trigger was successfully received by the LTF and the resulting preliminary analysis immediately revealed a high-energy detection with high significance (E. Bissaldi et al. 2022), with the highest-energy event being a 7.7 GeV photon detected 766 s after the BAT trigger. Meanwhile, the initial GBM trigger had been analyzed and found to be spatially consistent with the BAT and LAT localizations (S. Lesage et al. 2022). GBM data revealed a first emission episode with duration of ~ 40 s, followed by a second much longer and extremely bright emission episode, affected by strong pulse pileup and other systematic effects.⁹³ The preliminary GBM-reported peak flux and fluence clearly indicated that GRB 221009A was the most intense and fluent burst detected throughout the lifetime of the Fermi mission. Following the GBM notice, a new analysis was immediately initiated covering the first 3200s. This revealed an extremely bright and structured emission episode temporally coincident with the GBM main emission episode starting at $T_0 + 200$ s and a highest-energy photon of 99.3 GeV at $T_0 + 240$ s, which represented the highest photon energy ever detected by the LAT (R. Pilleri et al. 2022) associated with a GRB. However, as first reported in Z.-Q. Xia et al. (2022), LAT detected an even more energetic photon with an energy of 400 GeV ~ 9 hr after the GBM trigger (Z.-Q. Xia et al. 2024).

Over the following days, more than 100 different teams reported follow-up observations and different preliminary analyses of GRB 221009A. The first redshift measurement of $z = 0.151$ was provided by the X-shooter/VLT Team 11.5 hr after the GBM trigger (A. de Ugarte Postigo et al. 2022), and a spectroscopic redshift confirmation ($z = 0.1505$) came from the 10.4 m Gran Telescopio de Canarias (A. J. Castro-Tirado et al. 2022). Another remarkable feature of the burst afterglow was promptly detected in the Swift X-ray Telescope (XRT) analysis, which produced a stacked image in the 0.3–10 keV energy band, showing a complex system of expanding dust-scattering rings with radii from about 2.5–7.5 (A. Tiengo et al. 2023; G. Vasilopoulos et al. 2023), a system that was also observed by the Imaging X-ray Polarimetry Explorer (M. Negro et al. 2023) and the X-ray Multi-Mirror Mission (A. Tiengo et al. 2023).

Searches for neutrino and gravitational-wave counterparts around the time of the burst did not result in detections (KM3Net Collaboration 2022; S. Ai & H. Gao 2023; R. Abbasi et al. 2023). Additionally, the full Moon on the night of 2022 October 9 prevented all major IACT telescopes (MAGIC; H.E.S.S., and VERITAS) from immediately following up the event. The High-Altitude Water Cherenkov Observatory (HAWC) reported no detection in the burst region ~ 8 hr after the GBM trigger (H. Ayala & HAWC Collaboration 2022).

Two unexpected discoveries were announced by ground-based experiments a couple of days after the trigger. First, the Large High Altitude Air Shower Observatory (LHAASO) collaboration reported the detection of >500 GeV photons within 2000 s of the GBM trigger, with a significance greater than 100 standard deviations by the WDCA instrument.

Moreover, LHAASO-KM2A observed a record-breaking 18 TeV photon coming from the direction of GRB 221009A with a significance of 10 standard deviations (Y. Huang et al. 2022). However, in a subsequent reanalysis, the LHAASO Collaboration reported the detection of gamma rays up to just 13 TeV (Z. Cao et al. 2023a, 2023b). Following the LHAASO announcement, an even more remarkable claim was made by the Carpet-2 air-shower array collaboration, reporting the unprecedented detection of a 250 TeV photon-like air shower at $T_0 + 4536$ s (D. D. Dzheppuev et al. 2022); but, to date, no confirmation of it has been published in the literature.

In the months following the revelation of the B.O.A.T., dozens of highly significant articles were published, addressing various phenomenological and theoretical aspects of the GRB. Here we wish to mention a few relevant ones, that we will revisit later in our work. Z.-H. An et al. (2023) reported the observations of the B.O.A.T. with Insight-HXMT and GECAM-C, providing very accurate measurement of the emission during the first ~ 1800 s of the burst in the hard X-ray to soft gamma-ray band (~ 10 keV to ~ 6 MeV). Based on the GECAM-C unsaturated data of the main emission, they measured an isotropic equivalent energy of $\sim 1.5 \times 10^{55}$ erg. Moreover, B. O'Connor et al. (2023) presented multiwavelength observations of GRB 221009A, covering the first 3 months of its afterglow evolution, and attributed the behavior of the X-ray brightness decay to a shallow energy profile of a relativistic structured jet. Another remarkable work regarding multiwavelength observations of the burst's afterglow is the one by D. A. Kann et al. (2023), which presented observations in the X-ray and optical domains obtained by the GRANDMA and Insight Collaborations. They show that the afterglow of GRB 221009A is not extraordinarily luminous, highlighting that some aspects of this burst do not deviate from the global known sample. Finally, the discovery of a MeV emission line in the spectrum of GRB 221009A was announced by M. E. Ravasio et al. (2024), and will be also discussed later in this paper.

This paper is organized as follows: In Section 2 we present the LAT analysis, including the special treatment of the data during the bad time interval (BTI). In Section 3 we collect the results of the analysis of the triggering pulse, of the prompt emission and on the temporally extended emission. In Section 4 we model the high-energy emission from prompt to afterglow, disentangling the contribution from internal dissipation regions from that of the external shock, that was responsible for the late-time emission. In this section we also present a broadband modeling of the prompt emission combining LAT and GBM data, which indicates the presence of an extra high-energy component needed to describe the data. Finally, we compare GRB 221009A with the other LAT-detected GRBs. Summary and conclusions are drawn in Section 5. Additionally, Appendix A presents the details of the analysis performed to measure the flux during the brightest part of the GRB, and Appendix B collects additional information on the GBM–LAT joint fit.

2. Analysis Methods and Procedures

The LAT instrument (W. B. Atwood et al. 2009) comprises three subsystems: a tracker with 18 (x, y) tracking planes of silicon strip detectors interleaved with tungsten layers, a segmented calorimeter made of CsI(Tl) crystals and an anticoincidence detector (ACD) made of plastic scintillator tiles. The tracker induces e^+e^- pair conversion of the incident

⁹³ <https://fermi.gsfc.nasa.gov/ssc/data/analysis/grb221009a.html>

gamma-ray and measures its direction. The energy of the electromagnetic shower induced by the e^+e^- pair is measured in the calorimeter. The energy of the incident gamma-ray is estimated using information from both the tracker and calorimeter. The role of the ACD is to reject the charged cosmic-ray background. Due to the peculiar brightness of this GRB, the X-ray and soft gamma-ray ($E \lesssim 30$ MeV) flux was so intense during the brightest part of the emission that it produced a very high level of additional hits and energy deposits in all three subsystems (N. Omodei et al. 2022). Because the instrument and the event reconstruction were not designed to deal with such conditions, we have to carefully identify the time interval (flagged as BTI) during which standard analysis methods cannot be used, either *fermitools*⁹⁴ or the LAT Low Energy Event (LLE) technique (V. Pelassa et al. 2010; M. Ajello et al. 2014), which require that the standard instrument response functions (IRFs) correctly model the instrument response.

2.1. Dedicated Data Analysis of the Brightest Part of the GRB Prompt Emission

Shortly after launch, it was realized that a significant fraction of the recorded events⁹⁵ contained, in addition to the signals due to the triggering particle, the remnants of the signals due to a particle that passed through the instrument a few microseconds before the trigger was issued (M. Ackermann et al. 2012). Part of the Pass 8 effort (W. Atwood et al. 2013) to improve the event reconstruction was dedicated to mitigate the effect of these so-called ghost signals. It required modifying the instrument simulation to correctly take into account the presence of these spurious out-of-time signals. Together with the electronic noise, they constitute the background noise with respect to the signals of the triggering particle. Hence, we refer to these spurious out-of-time signals as an additional noise. This noise was actually captured with events that are recorded independently of the activity in the instrument thanks to a 2 Hz PERIODIC trigger (PT). Almost all of these ghosts correspond to only one out-of-time particle. Therefore, the event reconstruction and selection were designed to be as insensitive as possible to this additional noise.

Figure 1 shows the number of fired strips in the tracker as a function of time for events with at least one track that passed the main gamma-ray trigger and onboard filter, as well as for the PT events⁹⁶. Both before ($T_0 + \sim 217$ s) and after ($T_0 + \sim 280$ s) the main episode of the GRB, there are a few PT events with more than 10 strips that correspond to the remnants of out-of-time cosmic rays, but most of the PT events contain <10 strips (the majority of them having no signal in the tracker), which characterizes normal conditions of data taking.

On the contrary, during most of the time interval [$T_0 + \sim 217$ s, $T_0 + \sim 280$ s], the number of fired strips in PT events is >10 , and it can even exceed 100. Due to the very high deadtime, only a few PT events could be recorded during the brightest parts of the burst. However, we can use the bottom edge of the main-trigger event distribution (black dots in Figure 1) to estimate the noise in the tracker as a function of time: it exceeds 100 during two peaks of activity, for $T - T_0$

between 225 and 236 s and between 257 and 265 s. The intense X-ray and soft gamma-ray flux of the GRB also affected the calorimeter and the anticoincidence detector. As a consequence, the event reconstruction and selection are strongly impacted, and the standard IRFs cannot be expected to be valid during all of the prompt emission.

A detailed assessment of the effect of the X-ray and soft gamma-ray flux on the LAT is presented in Appendix A, as well as the dedicated analysis that we develop to be able to measure the flux of the GRB during its brightest period, which includes a special event reconstruction and selection. Here we summarize the main findings. In the following, because we need to follow the 1 s binning of the information stored in the LAT pointing and live-time history file, and because the GRB happened to reach the LAT out of phase by 0.4 s with respect to this 1 s binning, the times with respect to the GRB trigger are given with a decimal part of 0.6 s.

Regarding the standard energy measurement, we find that the noise contamination is >10 MeV during almost all of the time interval [$T_0 + 217.6$ s, $T_0 + 273.6$ s] and that it is beyond 100 MeV during [$T_0 + 225.6$ s, $T_0 + 235.6$ s] and [$T_0 + 257.6$ s, $T_0 + 264.6$ s]. We use the fraction of events with some fired strips in the tracker top corner facing the GRB direction to monitor the level of noise. It is 2% during normal conditions, and we use the times when it becomes $>3.5\%$ and then $<3.5\%$ to define the start and end of the BTI: [$T_0 + 216.6$ s, $T_0 + 280.6$ s].

As explained in Appendix A, to overcome the impact of the extra noise during this time interval, we use an energy estimator based only on the tracker information around the track. We select events passing the trigger and the onboard filter, with at least one track. Thanks to Earth-limb data and multiphoton simulations, we estimate the selection efficiency as a function of the noise level, and thus as a function of time. We require the event energy to be >160 MeV so that the false-positive rate is low enough. We calculate the GRB flux in 5 s intervals by fitting the distribution of the angular separation to the GRB with templates based on data and simulation.

2.2. The Fitting Procedure

To perform all of the fits in this analysis, except during the BTI, we used *ThreeML* (G. Vianello et al. 2015b), a python-based software package for parameter inference using the maximum likelihood formalism (with Bayesian posterior sampling supported as well). The likelihood calculation, including an interface to instrument response files and reading in data, is encapsulated in plug-ins, each corresponding to a certain instrument or data format, allowing joint likelihood fits of data sets recorded by different instruments. GBM and LLE data can be imported in *ThreeML* using the *OGIPLike* plug-in, which supports any type of file format based on an *OGIP*⁹⁷ standard, while for the LAT data set we used two different plug-ins, *FermiLATLike* for unbinned analysis (which interfaces with *gtburst*,⁹⁸ part of the *fermitools*), and *FermipyLike* for binned likelihood analysis via an interface to *fermipy* (M. Wood et al. 2017). Depending on the instrumental conditions and on the viewing angle of

⁹⁴ <https://fermi.gsfc.nasa.gov/ssc/data/analysis/software/>

⁹⁵ Each time the LAT instrument triggers on an incident particle and the corresponding signals in the subdetectors are measured, all of the related information is recorded, and it is named an event.

⁹⁶ See also <https://fermi.gsfc.nasa.gov/ssc/data/analysis/grb221009a.html>.

⁹⁷ OGIP stands for the Office of Guest Investigators Program, which established conventions for FITS files for high-energy astrophysics projects.

⁹⁸ <https://fermi.gsfc.nasa.gov/ssc/data/analysis/scitools/gtbust.html>

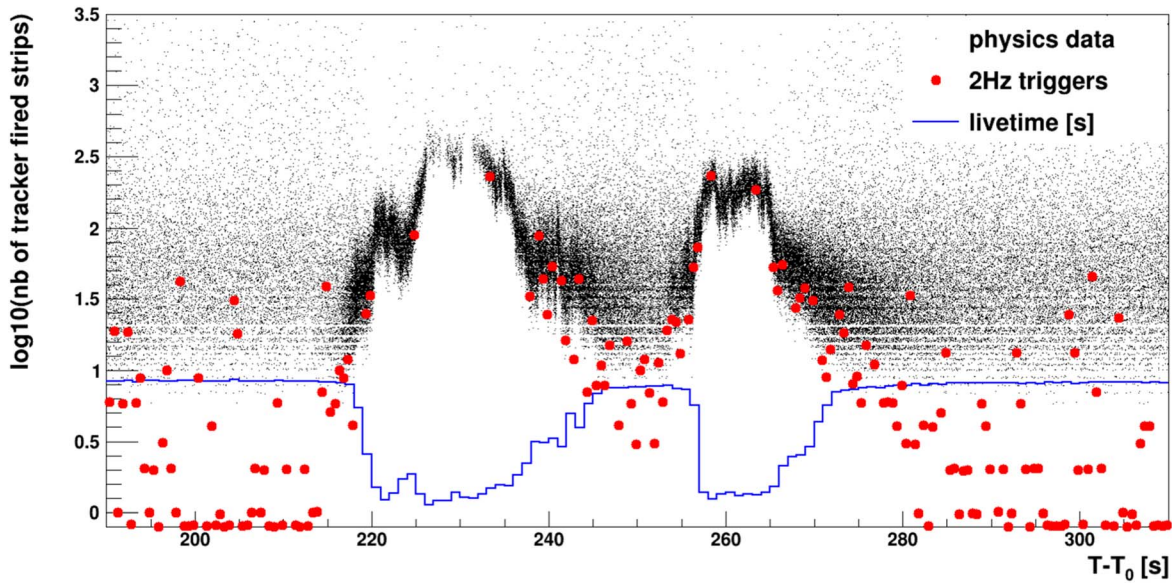


Figure 1. Number of hit strips in the tracker in the events with at least one track that pass the gamma-ray main trigger and onboard filter as a function of time since the GBM trigger (black dots). The red dots correspond to events triggered with a 2 Hz cadence to monitor the noise (both electronic and physical) in the instrument. For clarity's sake, events with no hit strips are plotted with $y = -0.1$. The blue histogram shows the live time recorded in the 1 s spacecraft file. During normal data-taking conditions (before $T_0 \sim 217$ s and after $T_0 + \sim 280$ s), the noise in the tracker can be very low (at most one strip), while during the brightest part of the GRB prompt emission, it is never empty and can reach more than 100 strips. We note that, because of the very high deadtime during the burst, which is a consequence of the extremely high GRB flux, the periodic trigger 2 Hz cadence could not be sustained.

GRB 221009A, we combine different data sets and use different plug-ins. In all of our analyses, we use the best-known localization R.A. = $288^\circ.264587$, decl. (J2000) = $19^\circ.773397$ reported by P. Atri et al. (2022).

3. Results

Figure 2 shows the Fermi broadband light curve, with two NaI detectors (n4, n7), a BGO detector (b1), the LLE and LAT light curves, as well as the LAT TRANSIENT_010E events with energies >100 MeV. We identify as the triggering pulse the emission episode from T_0 to $T_0 + 20$ s (left panel), while the entire prompt emission lasting approximately 10 minutes is shown in the right panel.

3.1. The Triggering Pulse

We first subdivide this interval by performing a Bayesian Blocks analysis (J. D. Scargle et al. 2013) on LLE data (V. Pelassa et al. 2010; M. Ajello et al. 2014), obtaining three time intervals. In order to perform a spectral analysis over a wider energy range, we also included low-energy (<10 MeV) data collected by the GBM and followed the prescriptions of the GBM Team (S. Lesage et al. 2023) in terms of detectors and data format selection, avoiding data types possibly affected by pulse pileup effects. We used data from detectors n4, n7, and b1, which have the best viewing angles with respect to the source, and are not affected by any blockage by the spacecraft or solar panels, in their nominal energy ranges. In particular, we analyzed time-tagged event (C. Meegan et al. 2009) data in the time interval prior to the main emission episode (from $T_0 - 0.69$ s to $T_0 + 19.95$ s, the triggering pulse analysis). We used detector response files specifically produced by the GBM Team for GRB 221009A (S. Lesage et al. 2023). For the spectral analysis of the triggering pulse, we used LLE data

from 30–100 MeV, and TRANSIENT_010E (>100 MeV) event class LAT data.⁹⁹

First, we tested different phenomenological spectral models, including a simple power law (PL), with $F(E) \propto E^{\Gamma_{\text{ph}}}$, Band, a power law with exponential cutoff (CPL)—the COMP model defined in the GBM GRB spectral catalog (S. Poolakkil et al. 2021)—and a double smoothly broken power law (2SBPL; M. E. Ravasio et al. 2018). We also tested for the presence of an extra PL for the CPL, Band, and 2SBPL models. To compare different models, we used the Bayesian information criterion (BIC), defined as $\text{BIC} = k \ln(N) - 2 \ln(\mathcal{L})$, where k is the number of free parameters of the model, N is the number of data points (equivalent to the number of spectral bins in a binned analysis or to the number of events in an unbinned analysis), and \mathcal{L} is the value of the likelihood. In Table 1 we summarize the values for the BIC of the different models tested. The models that best describe the triggering pulse with the lowest BIC are CPL and Band, but the parameters of the Band model are not well constrained in all time intervals. In particular, the first two time bins result in a Band parameter β value of -4.0 , which is extremely soft, and an unconstrained E_{peak} . In the last interval, the value of β is compatible with the results for the CPL model. As a result of this comparison, we conclude that CPL is the preferred model for describing the triggering pulse.

We further divided the last two intervals based on the GBM count rate in order to track the parameters of the CPL model on a finer timescale. In the left panel of Figure 3, we show the temporal evolution of the photon index and E_{peak} over the GBM and LAT LLE light curves. The values are listed in Table 2. In Appendix B, we show the spectral fits for all time bins. The emission is very energetic in the first temporal bin with a very high E_{peak} and a hard spectral index, and becomes

⁹⁹ We use the P8R3_TRANSIENT010E_V3 instrument response functions.

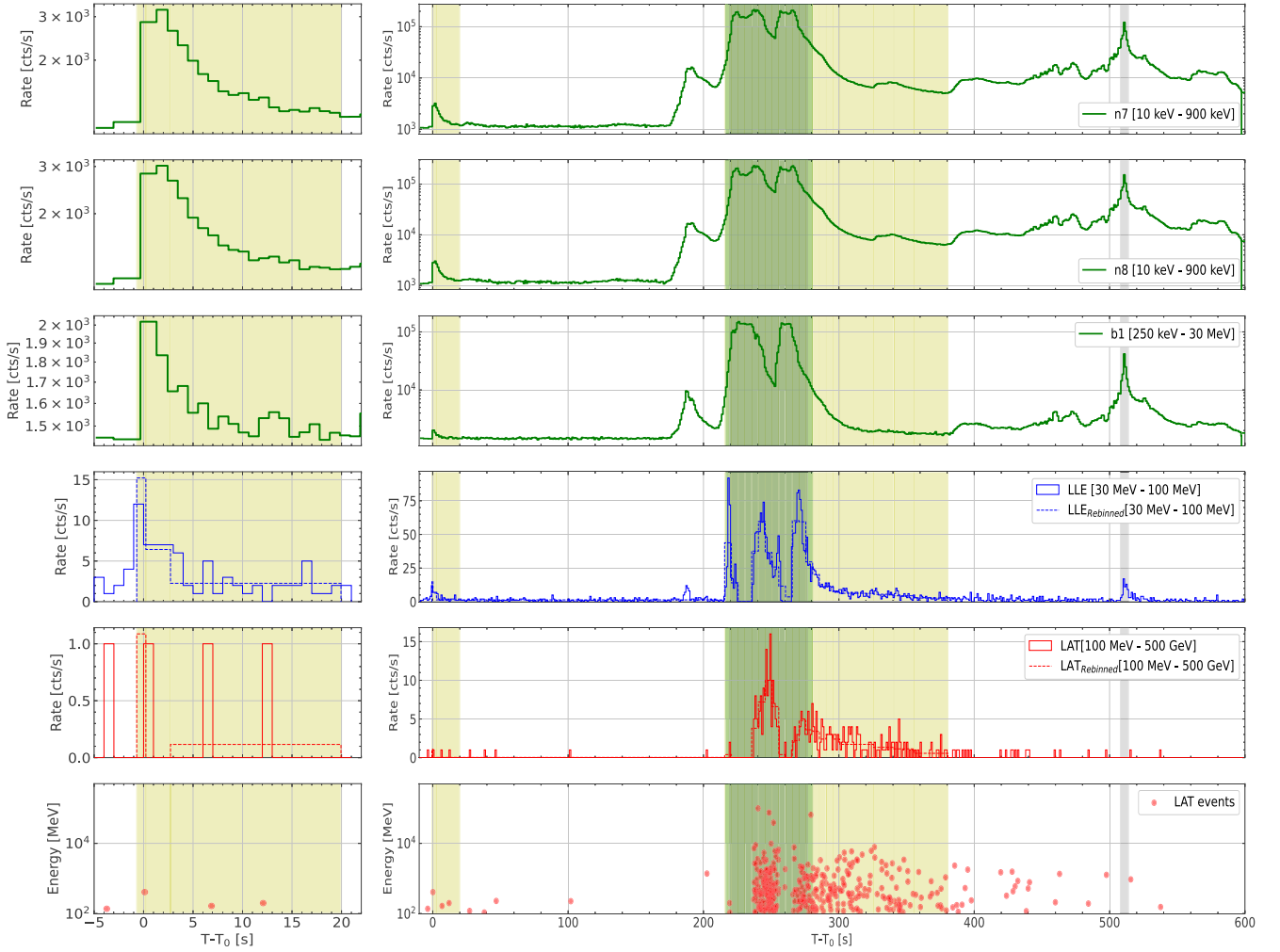


Figure 2. Left: light curve of the first 20 s after the GBM trigger (T_0) demonstrating the bright triggering pulse. Right: light curve of the entire 600 s interval after T_0 showing the main emission across the broad gamma-ray band including the shaded regions indicating the BTI: green indicates the LAT BTI; additionally, the two gray areas, one partially overlapping the green area, are the GBM BTIs (S. Lesage et al. 2023). Yellow shows the intervals selected for joint spectral analysis of the triggering pulse, and of the prompt emission (numerical values in Table 3). In both panels, the LAT and the LLE light curves are also shown rebinned using these intervals (blue and red dashed line, respectively) while, in the last panel, the reconstructed event energy is displayed as a function of the arrival time. The GBM light curves (first three panels) are not corrected for the pulse pileup effects.

Table 1
Values for the BIC Model Selection Estimator for the Three Time Intervals of the Triggering Pulse Obtained with Bayesian Blocks Analysis

Interval (s) (seconds from T_0)	BIC Values						
	PL	CPL	Band	2SBPL	CPL+PL	Band+PL	2SBPL+PL
−0.69–0.23	798	742	749	767	754	761	781
0.23–2.72	2182	1927	1928	...	1937	1939	...
2.72–19.95	4032	3913	3918	...	3922	3928	...

Note. In bold, we highlight the values for the lowest BIC in each interval. The CPL model is preferred in all intervals.

softer at later times. The right panel of Figure 3 shows the spectral evolution of the model. From $T_0 + 19.95$ to $T_0 + 175$ s, there is no detection of the GRB in neither standard LAT nor LLE data, and therefore, we derive a flux upper limit using standard LAT TRANSIENT_010E event class (Table 3).

3.2. The Prompt Phase

During the prompt phase (from $T_0 + 175$ s to $T_0 + 600$ s), we used data from different detectors for different time

intervals. From $T_0 + 175$ s to $T_0 + 215.6$ s and from $T_0 + 280.6$ s to $T_0 + 435$ s, we used LLE data from 30–100 MeV and TRANSIENT_010E above 100 MeV. We jointly fitted them using unbinned likelihood for the standard LAT event class with ThreeML. During [$T_0 + 215.6$ s, $T_0 + 280.6$ s], corresponding to the BTI, we apply the analysis described in Appendix A. At $T_0 + 435$ s, the GRB has a large incidence angle ($\sim 80^\circ$), and, even if the pulse at $T_0 + 510$ s is clearly visible in the LLE event selection, the instrument responses are not well modeled, so we did not perform any spectral analysis.

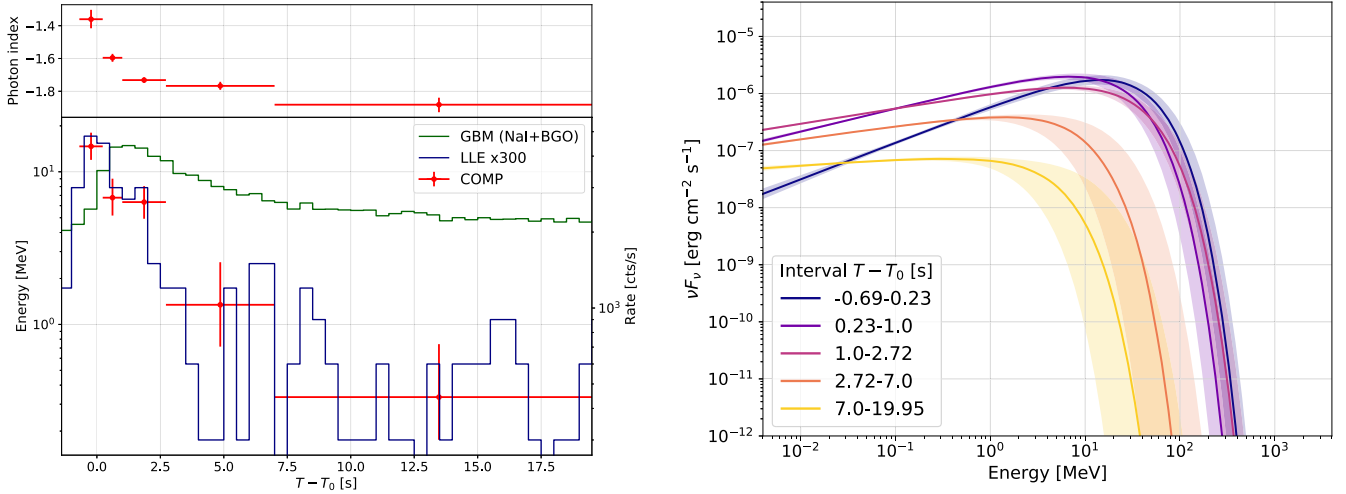


Figure 3. Left: temporal evolution of the spectral fit parameters during the triggering pulse. Top panel: low-energy power-law index; bottom panel: E_{peak} . The GBM and LLE light curves are also displayed and referenced to the right-hand y-axis. Right: time-resolved $\nu F(\nu)$ spectrum from -0.69 to 19.95 s with shaded regions representing the 68% confidence levels. The emission is extremely energetic in the first temporal bin, featuring a very high E_{peak} and a hard spectral index, and it softens over time.

Table 2

Parameter Values for the CPL Model in Each Interval of the Triggering Pulse

Interval	Index	E_{peak} (MeV)
-0.69 to 0.23	-1.36 ± 0.06	15 ± 3
0.23 – 1.00	-1.60 ± 0.02	7 ± 2
1.00 – 2.72	-1.73 ± 0.02	6 ± 2
2.72 – 7.00	$-1.77^{+0.03}_{-0.02}$	$1.3^{+0.6}_{-1.2}$
7.00 – 19.95	$-1.88^{+0.04}_{-0.05}$	$0.33^{+0.02}_{-0.04}$

In each of these time windows, we divided and analyzed the data into several intervals. Figure 4 shows the flux light curve in the 0.1 – 100 GeV energy band, and Table 3 lists the best model used (CPL or PL), the type of data used (GBM, LLE, and standard LAT analysis), the numerical values for the energy flux, the estimated photon index Γ_{ph} , and the value of the test statistic (TS). Since the TS is defined as $-2 \times (\log(\mathcal{L}_0) - \log(\mathcal{L}_1))$, with \mathcal{L}_1 the value of the likelihood and \mathcal{L}_0 the value of the likelihood when the source (in this case, the GRB) is removed, it is only available when the null hypothesis is defined. This is the case for LAT-only analysis, for which we modeled the background components, and not in case of GBM- or LLE-only analysis, where background-subtracted data were analyzed.

The first GBM BTI ($[T_0 + 219 \text{ s}, T_0 + 277 \text{ s}]$) is similar to the LAT BTI. During this main part of the GRB prompt phase, the emission in the GBM energy range exhibits two very bright peaks at about $T_0 + 230 \text{ s}$ and $T_0 + 260 \text{ s}$ (S. Lesage et al. 2023), which is confirmed by the noise monitoring in the LAT instrument reported in Appendix A.2.1. The GECAM-C observations (Z.-H. An et al. 2023), which were less impacted by the pulse pileup effect than the GBM data, provided more precise information on the flux and spectral properties of these two peaks, with the first one being about twice as bright as the second one. The emission above $\sim 100 \text{ MeV}$, on the other hand, has only one peak, whose maximum occurred during $[T_0 + 245 \text{ s}, T_0 + 250 \text{ s}]$, with a spectral index $\Gamma_{\text{ph}} = -1.6 \pm 0.1$. After this peak, the emission became softer ($\Gamma_{\text{ph}} \sim -3$) for 15 s and then, between $T_0 + 270 \text{ s}$ and $T_0 + 435 \text{ s}$, the power law became quite hard again, compared to other Fermi-LAT GRBs,

peaking at $\Gamma_{\text{ph}} = -1.6 \pm 0.1$ between $T_0 + 325 \text{ s}$ to $T_0 + 355 \text{ s}$. This rapid variation of the spectral index during the prompt emission and the striking variability observed in the LAT flux, with multiple episodes up to 400 s after T_0 , is a new feature not observed in other LAT-detected GRBs, and clearly indicates the detection of the prompt emission at high energies.

The probability that an event is spatially and spectrally associated with the GRB was calculated following M. Ajello et al. (2019), by using `gtsrcprob` after running the unbinned likelihood analysis in each time bin. During the BTI, we only used events with energies $> 1 \text{ GeV}$ to limit the effect of the noise induced by low-energy events. Four events with reconstructed energy greater than 10 GeV and probability ~ 1 were recorded by the LAT and are summarized in the first part of Table 4. The highest-energy event had an energy of 99 GeV , the highest photon energy recorded so far by the LAT during the prompt emission of a GRB. Measurement of the energies of these events, each of which was $> 10 \text{ GeV}$, was unaffected by the extra noise in the calorimeter, for which the average energy deposition per event was $< 100 \text{ MeV}$ (see Appendix A.1.1 and Figure 14).

3.3. Late-time Emission

For the late-time emission, we started our analysis at $T_0 + 3917.6 \text{ s}$, when the GRB reentered the LAT field of view. First, we computed the exposure as a function of time. Considering that the typical decay time for GRB gamma-ray emission goes as t^{-1} , where, in our convention, $t = (T - T_0)$, we multiplied the exposure by $(T - T_0)^{-1}$, providing us with a proxy for defining a temporal binning with an approximately constant number of expected events. Until $T_0 + 40 \text{ ks}$, we performed unbinned likelihood analysis with `P8_TRANSIENT010E` class events, while between $T_0 + 40 \text{ ks}$ and $T_0 + 10^6 \text{ s}$, given the longer exposures, we switched to binned likelihood analysis using `fermipy` in `ThreeML` with `P8_SOURCE` class events, which has a lower contamination from misclassified cosmic rays. In each time bin, we included all of the 4FGL (S. Abdollahi et al. 2020) sources with a predicted number of events > 1 , estimated by using the photon flux above 100 MeV in the 4FGL catalog multiplied by the bin exposure (in $\text{cm}^2 \text{ s}$). We left their

Table 3
Results of the Time-resolved Spectral Analysis from the GRB Onset to $T_0 + 500$ ks

Interval ($T-T_0$) (s)	Best Model	GBM	Data Used LLE	LAT	Flux (erg cm $^{-2}$ s $^{-1}$) 0.1–100.0 GeV	Γ_{ph}	TS
Triggering pulse							
–0.69 to 0.23	CPL	X	X	X	$<1.0 \times 10^{-8}$...	0.0
0.23–2.72	CPL	X	X	X	$<2.0 \times 10^{-9}$...	0.0
2.72–19.95	CPL	X	X	X	$<1.0 \times 10^{-9}$...	5.0
19.95–175.00	PL			X	$<3.2 \times 10^{-8}$	–2.5 (fixed)	7.8
Prompt							
175.6–215.6	PL		X	X	$<8.0 \times 10^{-10}$	<-5	0.0
215.6–220.6	PL			X †	$(4 \pm 2 \text{ }^{+0.06}_{-0.04} \text{ sys}) \times 10^{-7}$	-3.7 ± 0.4	83.4
220.6–225.6	PL			X †	$(5 \pm 1 \text{ }^{+0.5}_{-0.4} \text{ sys}) \times 10^{-6}$	-3.5 ± 0.3	260.8
225.6–230.6	PL			X †	$(7 \pm 4 \text{ }^{+4}_{-2} \text{ sys}) \times 10^{-6}$	-3.7 ± 0.4	59.6
230.6–235.6	PL			X †	$(2 \pm 1 \text{ }^{+0.7}_{-0.5} \text{ sys}) \times 10^{-5}$	-2.6 ± 0.3	181.1
235.6–240.6	PL			X †	$(2.8 \pm 0.9 \text{ }^{+0.3}_{-0.2} \text{ sys}) \times 10^{-5}$	-2.2 ± 0.1	965.4
240.6–245.6	PL			X †	$(5 \pm 2 \text{ }^{+0.2}_{-0.2} \text{ sys}) \times 10^{-5}$	-1.9 ± 0.1	1346.3
245.6–250.6	PL			X †	$(9 \pm 3 \text{ }^{+0.1}_{-0.1} \text{ sys}) \times 10^{-5}$	-1.63 ± 0.09	1539.8
250.6–255.6	PL			X †	$(2.4 \pm 0.9 \text{ }^{+0.06}_{-0.04} \text{ sys}) \times 10^{-5}$	-1.9 ± 0.1	828.1
255.6–260.6	PL			X †	$(4 \pm 2 \text{ }^{+0.4}_{-0.3} \text{ sys}) \times 10^{-6}$	-3.1 ± 0.3	220.7
260.6–265.6	PL			X †	$(1.8 \pm 0.5 \text{ }^{+0.3}_{-0.3} \text{ sys}) \times 10^{-5}$	-3.1 ± 0.2	405.4
265.6–270.6	PL			X †	$(5 \pm 1 \text{ }^{+0.3}_{-0.2} \text{ sys}) \times 10^{-6}$	-2.8 ± 0.2	485.3
270.6–275.6	PL			X †	$(1.5 \pm 0.5 \text{ }^{+0.03}_{-0.02} \text{ sys}) \times 10^{-5}$	-2.1 ± 0.1	807.8
275.6–280.6	PL			X †	$(6 \pm 2 \text{ }^{+0.09}_{-0.07} \text{ sys}) \times 10^{-6}$	-2.2 ± 0.2	466.3
280.6–285.6	PL		X	X	$(1.0 \pm 0.4) \times 10^{-5}$	-2.1 ± 0.1	204.0
285.6–290.6	PL		X	X	$(1.2 \pm 0.6) \times 10^{-5}$	-1.9 ± 0.1	138.0
290.6–295.6	PL		X	X	$(9 \pm 4) \times 10^{-6}$	-2.0 ± 0.1	178.0
295.6–300.6	PL		X	X	$(1.4 \pm 0.7) \times 10^{-5}$	-1.8 ± 0.1	148.0
300.6–325.6	PL		X	X	$(9 \pm 2) \times 10^{-6}$	-1.82 ± 0.06	505.0
325.6–340.6	PL		X	X	$(2.0 \pm 0.8) \times 10^{-5}$	$-1.63^{+0.08}_{-0.09}$	263.0
340.6–355.6	PL		X	X	$(1.2 \pm 0.6) \times 10^{-5}$	-1.7 ± 0.1	172.0
355.6–380.6	PL		X	X	$(5 \pm 3) \times 10^{-6}$	-1.7 ± 0.1	139.0
380.6–435.6	PL		X	X	$(2 \pm 1) \times 10^{-6}$	-1.8 ± 0.2	42.0
Extended							
3930–5010	PL			X	$(1.7 \pm 0.6) \times 10^{-8}$	$-2.1^{+0.2}_{-0.1}$	116.3
5010–6810	PL			X	$(1.0 \pm 0.3) \times 10^{-8}$	$-2.2^{+0.1}_{-0.2}$	100.0
9630–15,870	PL			X	$(4 \pm 1) \times 10^{-9}$	-2.2 ± 0.2	75.8
15,870–27,810	PL			X	$(3 \pm 1) \times 10^{-9}$	-2.1 ± 0.2	67.6
27,810–51,090	PL			X	$(1.3 \pm 0.6) \times 10^{-9}$	-2.0 ± 0.2	33.4
51,090–90,570	PL			X *	$(4 \pm 2) \times 10^{-10}$	-2.6 ± 0.4	13.4
90,570–164,130	PL			X *	$<2.0 \times 10^{-10}$	–2.0 (fixed)	5.2
164,130–284,490	PL			X *	$(2.0 \pm 0.8) \times 10^{-10}$	-2.5 ± 0.3	10.0
284,490–495,330	PL			X *	$<8.0 \times 10^{-11}$	–2.0 (fixed)	3.1

Note. The table includes the best model (CPL or PL), the data used in the fit, the energy flux, the photon index Γ_{ph} (only for the PL model), and the test statistic (TS). Upper limits are at 95% confidence. For the entries marked with † , the results were obtained with the special analysis described in Appendix A. For the entries marked with * , we used the ThreeMLfermipy plug-in with SOURCE class.

normalizations free to vary.¹⁰⁰ Three events with energies >10 GeV arrived during this phase, as summarized in Table 4 and in Figure 5. In particular, the LAT recorded an event with an energy of 400 GeV (Z.-Q. Xia et al. 2022) arriving 33 ks after the GBM trigger. Its origin and association with GRB 221009A will be discussed in Section 4.7. The light curve for GRB 221009A is displayed in logarithmic scale in Figure 5 with numerical values in the last part of Table 3.

To compute the onset time and the duration of the 100 MeV–100 GeV flux light curve, we used the same algorithm developed in M. Ajello et al. (2019): First, we calculated the probability for each photon to be associated with the GRB using the result of the likelihood analysis (using gtsrcprob).

The onset time $T_{\text{LAT},0}$ corresponds to the time when the first photon with probability $p > 0.9$ to be associated with the GRB is detected, while $T_{\text{LAT},1}$ corresponds to the last photon with $p > 0.9$. $T_{\text{LAT},100}$ of the signal is simply $T_{\text{LAT},1} - T_{\text{LAT},0}$. To estimate the uncertainty on $T_{\text{LAT},1}$ ($\delta T_{\text{LAT},1}$) for an event with n detected photons with probability $p > 0.9$, we define $\Delta t_{n-1,n}$ as the time interval between the second-to-last and the last event. Assuming Poisson statistics, the probability of measuring an event between t and $t + dt$ is $P(t, t + dt) = \lambda dt$, where λ is the rate: in our case $\lambda = 2/\Delta t_{n-1,n}$. Therefore, we conservatively compute the uncertainty as $\delta T_{\text{LAT},1} = 1/\lambda = \Delta t_{n-1,n}/2$. Similarly, considering the first two events with probability $p > 0.9$, we define the uncertainty on $T_{\text{LAT},0}$ as $\delta T_{\text{LAT},0} = \Delta t_{1,2}/2$. The error on $T_{\text{LAT},100}$ follows using standard error propagation. The arrival times of the first and last events of

¹⁰⁰ In our analysis, we used the 4FGL-DR3 release of the 4FGL catalog.

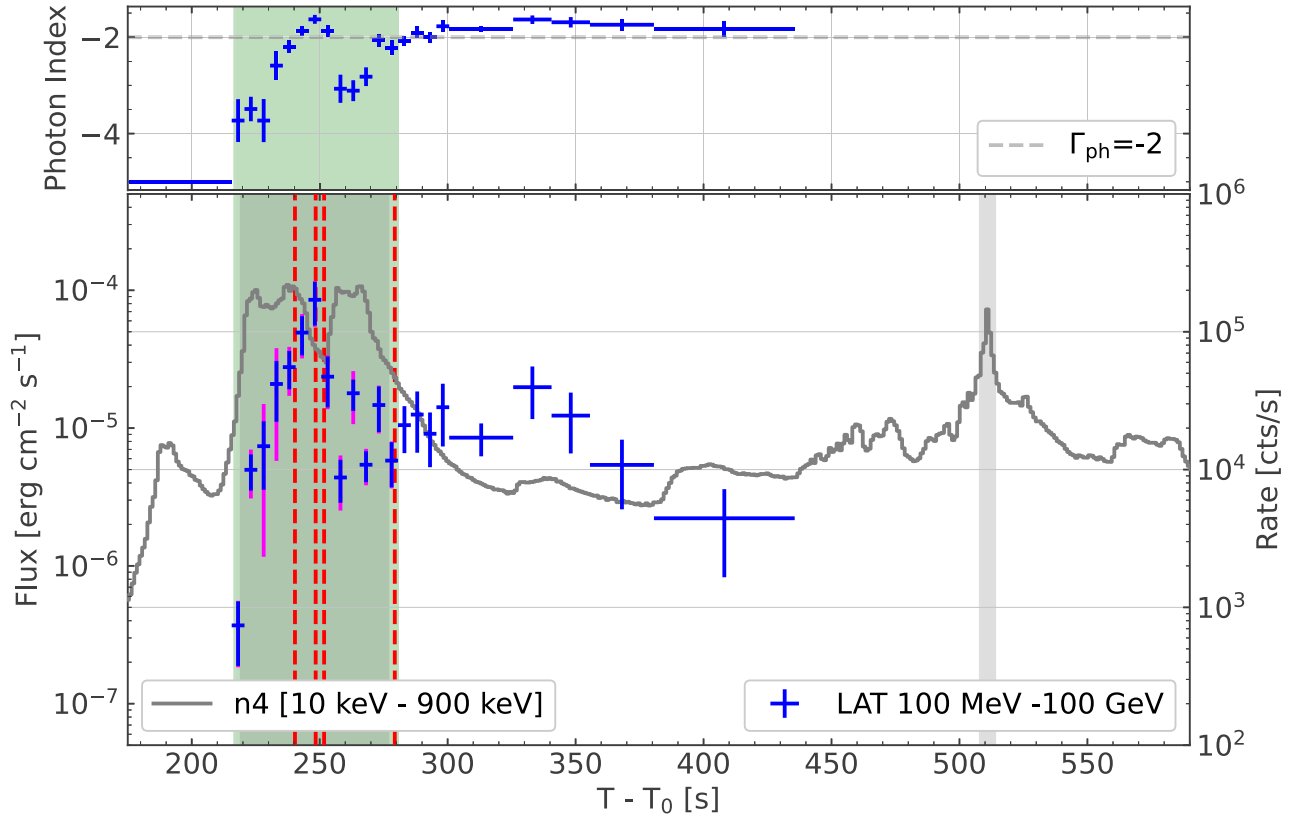


Figure 4. Fermi high-energy emission between 175 s and 590 s displaying the photon index (top panel) and the flux between 100 MeV and 100 GeV measured by the Fermi-LAT (bottom panel). Magenta error bars indicate the sum of the statistical and systematic uncertainties estimated during the BTI. The gray curve is the rate of events in the GBM detector n4 (not corrected for pulse pileup effects) with numerical values on the right-hand vertical axis. The vertical red dashed lines correspond to the arrival times of the >10 GeV photons, while the shaded regions indicate the BTI: green indicates the LAT BTI, and the two gray areas are the GBM BTIs (S. Lesage et al. 2023).

Table 4
Fermi-LAT Events with Energies >10 GeV that Arrived within 1° ROI
Centered at the Position of the GRB Optical Counterpart

$T - T_0$ (s)	Energy (GeV)	Prob.	Conv. Type.	Ang. Sep. (deg)
Prompt				
240.336	99	...	Back	0.70^\dagger
248.427	75	1.000	Back	0.05
251.724	39	1.000	Back	0.25
279.342	65	1.000	Front	0.19
Extended				
10475.104	24	0.998	Front	0.10
16176.428	15	0.993	Front	0.16
33552.966	398	1.000	Back	0.02

Note. For the 99 GeV event, the angular separation from the GRB localization is marked with a \dagger because the high level of noise in the tracker affected the direction reconstruction. We checked this event carefully, and we concluded that its origin is compatible with the GRB location.

GRB 221009A with $p > 0.9$ are $T_{\text{LAT},0} = T_0 + 6.86$ s and $T_{\text{LAT},1} = T_0 + 176,673.012$ s. The uncertainties estimated with the procedure described above, are $\delta T_{\text{LAT},0} = 106.22$ s and $\delta T_{\text{LAT},1} = 2822.44$ s, which lead to $T_{\text{LAT},100} = 176 \pm 3$ ks. The first event arrived during the triggering pulse. The second event associated with GRB 221009A arrived ~ 200 s later, emphasizing the separate nature of the triggering pulse with the bulk of the GRB emission. The last events arrived more than 2 days

after the GBM trigger, setting a new record on the duration of LAT-detected GRBs.

4. Discussion

The results presented in Section 3 allowed us to put some constraints on the modeling and to discuss possible scenarios responsible for the emission at high energies.

4.1. Modeling the High-energy Light Curve

We modeled the 100 MeV–100 GeV energy flux light curve as the sum of multiple functions. First, we modeled the entire light curve with a smoothly broken power law (f_0) representing the typical forward shock emission for which we adopted the definition presented in E. Nakar & T. Piran (2004):

$$f_0(T) = K \left(\frac{1}{2} \left(\frac{T - T_{\text{on}}}{\tau} \right)^{-\xi\alpha_1} + \frac{1}{2} \left(\frac{T - T_{\text{on}}}{\tau} \right)^{-\xi\alpha_2} \right)^{-\frac{1}{\xi}}, \quad (1)$$

where α_1 and α_2 are the values of the early and late-time indexes, τ is a scale parameter, and ξ defines how smooth the transition is. Note that $T_{\text{on}} \neq T_0$; therefore, the light curve does not exhibit the typical two-segment power-law behavior (two straight lines on a log–log scale) that would otherwise be expected. For our analysis, to limit the number of parameters, we fixed $\xi = 2$ and $\alpha_1 = 3$ as predicted by the standard afterglow model (E. Nakar & T. Piran 2004). The time T_p of the

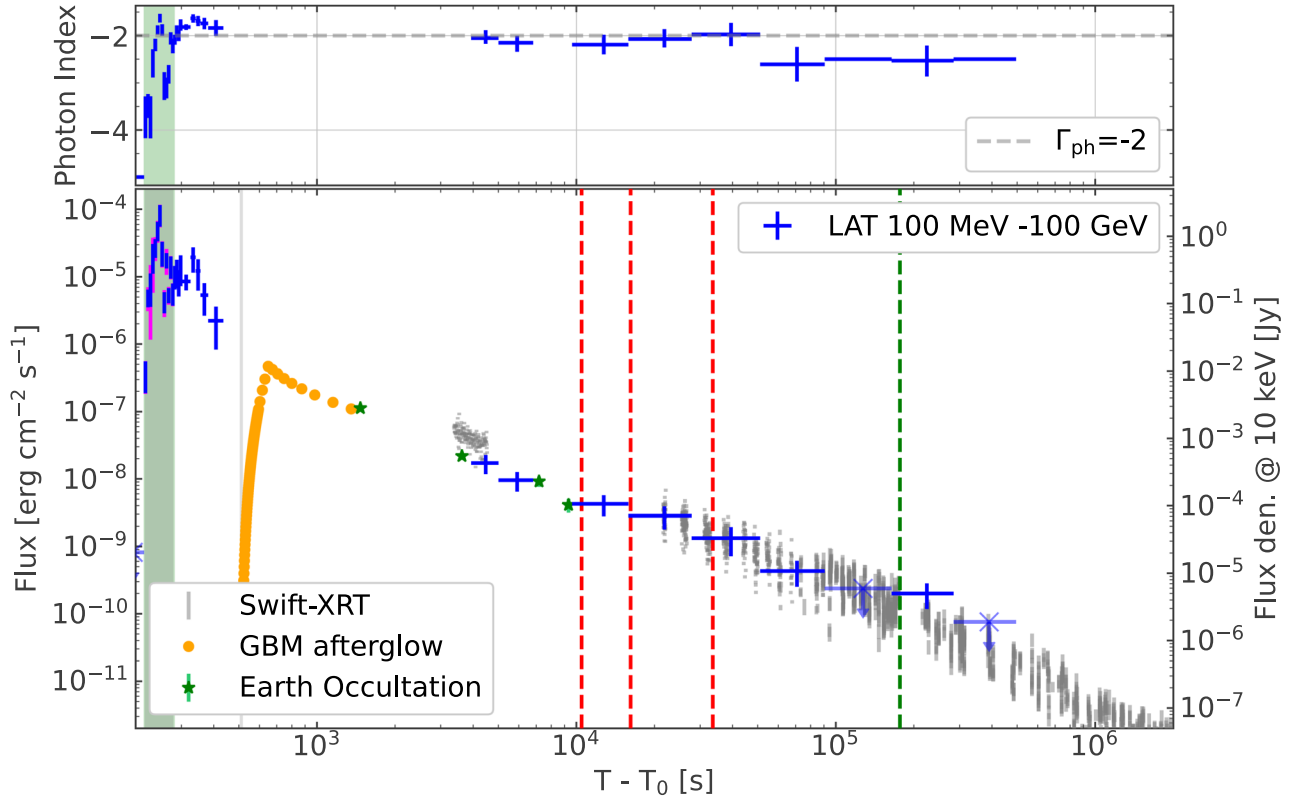


Figure 5. Late-time emission observed by Fermi and Swift. Top panel: photon index of the LAT emission, in blue. Bottom panel: flux between 100 MeV and 100 GeV (blue) with, in magenta, the sum of the statistical and systematic uncertainties during the BTI. Orange points, green stars, and gray dots are the Fermi-GBM and Swift-XRT afterglow measurements (flux density at 10 keV) obtained by S. Lesage et al. (2023) with values reported on the right-hand vertical axis. The vertical red dashed lines correspond to the arrival times of the >10 GeV photons, while the green dashed line is the arrival time of the last event with a probability >0.9 to be associated with GRB 221009A. As in the previous figure, the shaded regions indicate the BTIs.

peak of the afterglow relative to onset time T_{on} is

$$T_p = \tau \left(-\frac{\alpha_2}{\alpha_1} \right)^{\frac{1}{\xi(\alpha_2 - \alpha_1)}}. \quad (2)$$

After performing the fit with $f_0(T)$, we repeated the fit adding one, two, or three pulses using the pulse shape described in J. P. Norris et al. (2005) and J. Hakkila & R. D. Preece (2014) with the following functional form:

$$f_i(T) = K_i \begin{cases} \exp\left(\frac{T - T_{p,i}}{\tau_i}\right), & \text{for } T < T_{p,i}, \\ \exp\left(\frac{T_{p,i} - T}{\xi_i \tau_i}\right), & \text{for } T > T_{p,i}, \end{cases} \quad (3)$$

where τ_i is the rise time of the i th pulse, and $\xi_i \neq 1$ for asymmetric pulses.

The best-fit parameters are summarized in Table 5, and the best-fit models are displayed in Figure 6. The LHAASO-WCDA light curve (Z. Cao et al. 2023a) is also displayed (but is not used in the fitting procedure). The LAT light curve clearly shows multiple emission episodes, and the preferred model fit (with the lowest value of the BIC) is the one with three components. A single emission episode described by f_0 fails to reproduce the complex behavior of the flux during the prompt emission, even if it is consistent with the flux observed at high energy by LHAASO-WCDA. In order to obtain a significantly better fit of the LAT data, two additional pulses are required, one describing the pulse at 350 s after the trigger,

and another one describing the narrow feature observed during the BTI, at ~ 250 s. Adding more pulses increases the BIC value (indicating that the increased complexity of the model is not justified).

4.2. Internal versus External Emission

GRB 221009A is a complex burst in which multiple emission mechanisms from multiple radii from the central engine could be at play simultaneously. The nature of the late-time LAT emission during $\sim T_0 + 4 \times 10^3 \text{ s} - \sim T_0 + 3 \times 10^5 \text{ s}$ is similar to the extended emission detected by the LAT from other GRBs, and the emission is due to the synchrotron process from an external forward shock (see, e.g., P. Kumar & R. Barniol Duran 2009; G. Ghisellini et al. 2010; M. Ackermann et al. 2010; S. Razzaque 2010; A. Corsi et al. 2010). The temporal decay of the flux during this time is $F_\nu \propto (T - T_0)^{-1.27 \pm 0.05}$, or $(T - T_0)^{-1.35 \pm 0.03}$, depending on the model, which is between the flux decay $F_\nu \propto t^{-1}$ and $F_\nu \propto t^{-10/7}$ expected for an adiabatic blast wave and a radiative blast wave, respectively. However, an adiabatic blast wave is favored by previous LAT detections (M. Ajello et al. 2019). The onset time T_{on} ranges from $213 \pm 1 \text{ s}$ to $214 \pm 1 \text{ s}$, slightly before the onset time T measured by LHAASO, while the peak T_p of the afterglow from the onset time ranges from $23 \pm 4 \text{ s}$ to $17 \pm 4 \text{ s}$, with the value for the best-fit model being 18_{-3}^{+4} s being consistent with the value derived by LHAASO for the 0.3–5 TeV light curve. The two emission episodes at $T_0 + 330 \text{ s}$ and $T_0 + 250 \text{ s}$ described by f_1 and f_2 , respectively,

Table 5
Parameters of the Best-fit Models for f_0 , f_1 , f_2 , and f_3 and Derived Quantities T_p , Γ , Fluence, and E_{iso}

	f_0	$f_0 + f_1$	$f_0 + f_1 + f_2$	$f_0 + f_1 + f_2 + f_3$
K_0 [erg cm $^{-2}$ s $^{-1}$]	$(1.8 \pm 0.3) \times 10^{-5}$	$(1.6 \pm 0.3) \times 10^{-5}$	$(1.3 \pm 0.3) \times 10^{-5}$	$(1.1^{+0.4}_{-0.2}) \times 10^{-5}$
α_1	3.0 (fixed)	3.0 (fixed)	3.0 (fixed)	3.0 (fixed)
α_2	-1.35 ± 0.03	-1.31 ± 0.04	-1.27 ± 0.05	$-1.25^{+0.06}_{-0.05}$
ξ	2 (fixed)	2 (fixed)	2 (fixed)	2 (fixed)
τ [s]	20 ± 2	18^{+3}_{-2}	17^{+4}_{-3}	15^{+4}_{-3}
T_{on} [s]	213 ± 1	214 ± 1	215 ± 2	215 ± 2
K_1 [erg cm $^{-2}$ s $^{-1}$]	...	$(1.7^{+1}_{-0.6}) \times 10^{-5}$	$(1.7^{+0.6}_{-0.5}) \times 10^{-5}$	$(1.7^{+0.7}_{-0.4}) \times 10^{-5}$
$T_{p,1}$ [s]	...	330 ± 10.0	333 ± 2	333 ± 2
τ_1 [s]	...	22^{+10}_{-8}	25^{+9}_{-6}	25^{+8}_{-5}
ξ_1	...	$1.1^{+1}_{-0.6}$	1.1 ± 0.4	$1.0^{+0.4}_{-0.3}$
K_2 [erg cm $^{-2}$ s $^{-1}$]	$(1.2^{+0.7}_{-0.4}) \times 10^{-4}$	$(1.2^{+0.6}_{-0.4}) \times 10^{-4}$
$T_{p,2}$ [s]	247.4 ± 0.9	247.3 ± 0.9
τ_2 [s]	4^{+2}_{-1}	4^{+2}_{-1}
ξ_2	$0.5^{+0.3}_{-0.2}$	$0.5^{+0.3}_{-0.2}$
K_3 [erg cm $^{-2}$ s $^{-1}$]	$(1.1^{+4}_{-0.9}) \times 10^{-5}$
$T_{p,3}$ [s]	263^{+3}_{-2}
τ_3 [s]	$0.6^{+0.2}_{-0.1}$
ξ_3	3^{+3}_{-1}
BIC	69.2	64.9	62.6	71.2
Δ_{BIC}	0	-4.3	-2.3	8.6
T_p	21^{+3}_{-2}	23 ± 4	18^{+4}_{-3}	17 ± 4
Γ (wind)	240 ± 7	237 ± 10	250 ± 10	$250.0^{+20.0}_{-10.0}$
Γ (ISM)	490 ± 20	480 ± 30	520 ± 40	$530.0^{+50.0}_{-40.0}$
Fluence [erg cm $^{-2}$]	$(1.4 \pm 0.1) \times 10^{-3}$	$(2.2 \pm 0.3) \times 10^{-3}$	$(2.6 \pm 0.4) \times 10^{-3}$	$(2.7 \pm 0.4) \times 10^{-3}$
E_{iso} [erg]	$(9 \pm 0.8) \times 10^{52}$	$(1 \pm 0.2) \times 10^{53}$	$(2 \pm 0.3) \times 10^{53}$	$(2 \pm 0.3) \times 10^{53}$

Note. Both calculated between 100 MeV and 100 GeV from the onset time T_{on} and 300 ks. The value of the BIC and its increase (or decrease) with respect to that with one less component is also shown.

are very unlikely to have originated from the afterglow forward shock emission. Although we could not perform a detailed joint spectral analysis of the first pulse, basically due to the presence of BTIs in both the Fermi-LAT and GBM, a detailed joint fit of GBM and LAT data is presented in Section 4.4, including information from LHAASO-WCDA, too.

Generally speaking, synchrotron emission from the reverse shock cannot extend to the GeV energy range, since no new electrons are accelerated after reverse shock crossing (S. Kobayashi 2000). Such a synchrotron component has maximum energy, which is related to the adiabatically cooled maximum electron Lorentz factor due to synchrotron cooling. Even if we extend the emission from the reverse shock to higher energies, the temporal flux decay $F_\nu \propto (T - T_0)^{-(73p+21)/96}$ for a thick shell and $F_\nu \propto (T - T_0)^{-(27p+7)/35}$ for a thin shell (S. Kobayashi 2000), can explain flux decaying as $F_\nu \propto (T - T_0)^{-2.1}$ only for $p = 2.5$ and is also very unlikely to produce exponentially decaying emission. Finally, even the high-latitude emission from a shell, a so-called “naked GRB” (P. Kumar & A. Panaitescu 2000) with $F_\nu \propto (T - T_0)^{-(2-\beta)} \propto (T - T_0)^{-3}$ for the spectral index $\beta = -1$, is unable to produce this steep flux decay detected by the LAT. Therefore, the most natural explanation is that the LAT detected prompt internal emission until at least $\sim T_0 + 380$ s. Our model suggests that during the prompt emission, the afterglow is subdominant to the prompt emission, at least in the energy range below 100 GeV, while it becomes dominant at higher energies, in agreement with the LHAASO-WCDA light curve. A combination of shells ejected earlier in the burst with higher bulk Lorentz factors could

initiate an afterglow even while shells with lower bulk Lorentz factors continue to produce prompt emission. Therefore, the afterglow onset time could lie between $\sim T_0 + 215$ s, i.e., the beginning of the bright emission detected by the LAT, and $\sim T_0 + 600$ s, when the afterglow-like feature was detected in X-rays by Konus-Wind (D. Frederiks et al. 2023). Using the values of the best-fit model ($f_0 + f_1 + f_2$), the onset of f_0 ($T_{\text{on}} = 215 \pm 2$ s) and its peak ($T_p = 18^{+4}_{-3}$ s) do indeed suggest that the afterglow peaks at early times. By identifying the peak time with the deceleration time of the afterglow, and using the kinetic energy E_K from S. Lesage et al. (2023), we can derive the Lorentz factor, as in, e.g., F. Nappo et al. (2014) and G. Ghirlanda et al. (2018):

$$\Gamma = \left[\left(\frac{17 - 4s}{16\pi(4 - s)} \right) \left(\frac{E_K}{n_0 m_p c^{5-s}} \right) \right]^{\frac{1}{8-2s}} \left(\frac{T_p}{1 + z} \right)^{-\frac{3-s}{8-2s}}, \quad (4)$$

where T_p is the peak time in seconds, m_p is the mass of a proton, and c is the speed of light. We considered both a constant density interstellar medium (ISM) ($s = 0$) and a wind density profile ($s = 2$). For the first case, we assumed density $n_0 = 1$ cm $^{-3}$, while for the second case, we assumed $n(r) = n_0 r^{-2}$ with $n_0 = 3.2 \times 10^{35}$ cm $^{-1}$.

The derived values for Γ (wind) and Γ (ISM) are summarized in Table 5. For the best-fit model, using $T_p = 18^{+4}_{-3}$, we obtained $\Gamma = 250 \pm 10$ for the wind scenario ($s = 2$) and $\Gamma = 520 \pm 40$ for the constant density ISM ($s = 0$). Assuming the derivation from R. Sari & T. Piran (1999) instead, also applied by Z. Cao et al. (2023a), we obtain their

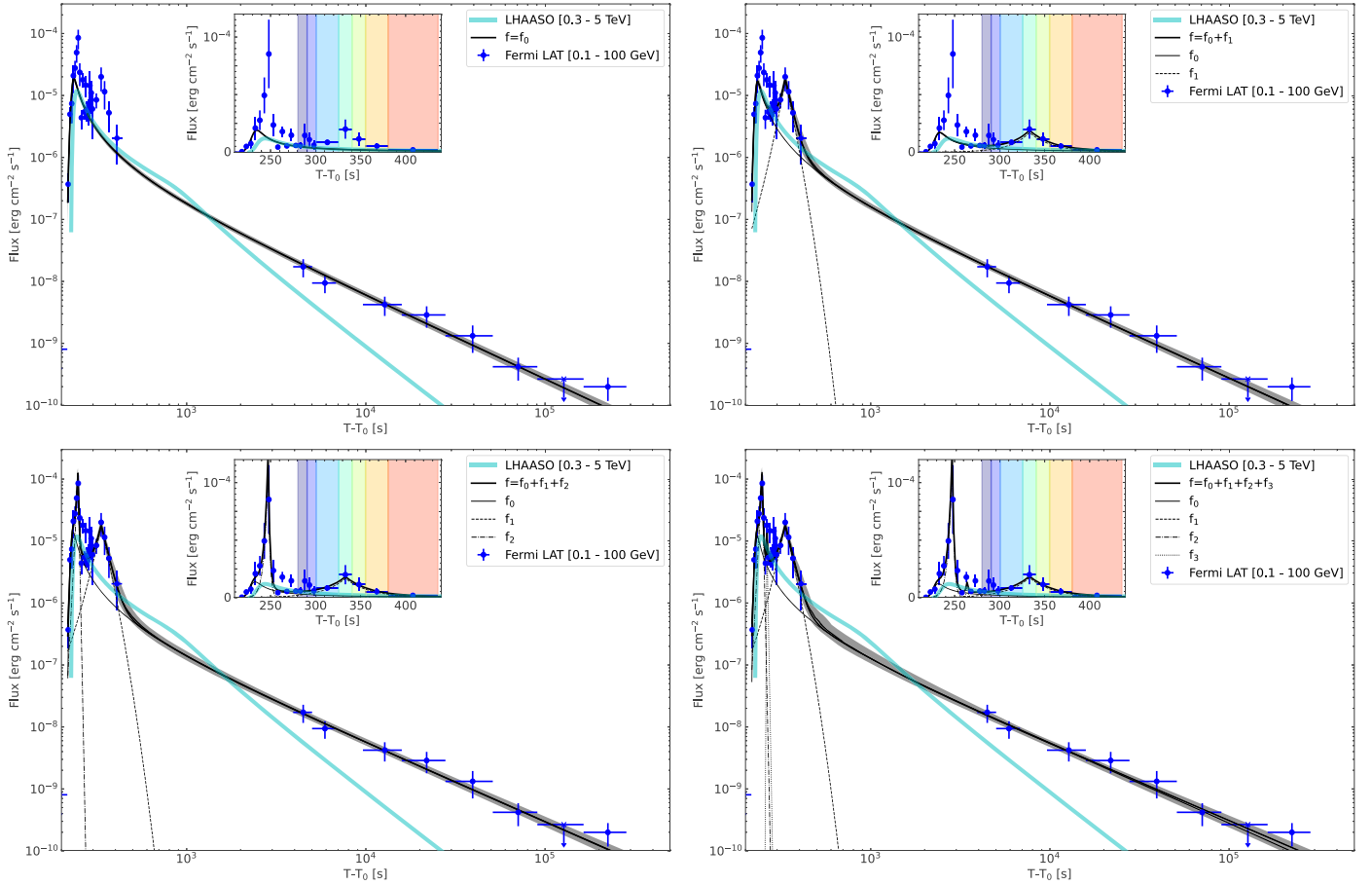


Figure 6. Model (and the components) used to describe the >100 MeV flux light curve as a function of time. Top left: model with one component describing a pure afterglow emission (f_0). Top right: $f_0 + f_1$. Bottom left: the best-fit model: $f_0 + f_1 + f_2$. Bottom right: $f_0 + f_1 + f_2 + f_3$ models including both afterglow emission and one, two, or three pulses. In each panel, the gray band displays the 68% contour levels, obtained by sampling the posterior distribution. The cyan curve is the LHAASO-WCDA 300 GeV–5 TeV light curve (Z. Cao et al. 2023a). In the inset plots, the prompt emission (in linear y-scale) is shown. The seven colored bands highlight the time intervals used in the combined Fermi-GBM, Fermi-LAT, and LHAASO fit displayed in Figure 8.

exact same value of $\Gamma = 440$. If we adopt the equation proposed by B. Zhang (2019), we obtain a value of $\Gamma = 600$, as also reported in B. Zhang et al. (2024). These values represent lower limits on the outflow Lorentz factor, which can be significantly higher for a relativistic reverse shock (i.e., a “thick shell,” which is likely the case for this GRB).

To estimate the released energy of GRB 221009A, we integrated the best-fit model in time between the onset time T_{on} and 300 ks. The last two rows of Table 5 show the values for each model. For the best-fit model, we obtained a fluence of $(2.6 \pm 0.4) \times 10^{-3}$ erg cm $^{-2}$, which corresponds to an isotropic energy $E_{\text{iso}} = (2 \pm 0.3) \times 10^{53}$ erg, both calculated between 100 MeV and 100 GeV.

4.3. Estimation of the Bulk Lorentz Factor from Pair Opacity

The bulk Lorentz factor can be directly estimated by measuring the spectral cutoff in the high-energy band due to the pair opacity (G. Vianello et al. 2018; M. Ajello et al. 2020; M. Arimoto et al. 2020). We tested the presence of a spectral cutoff during the prompt phase by comparing the fit with a simple power law with one that has an additional exponential cutoff at high energies. We found that the model with a cutoff was not preferred in any of the time intervals; thus, we can set a

lower limit on the bulk Lorentz factor, $\Gamma_{\text{bulk,min}}$:

$$\Gamma_{\text{bulk,min}} = 500 \left[N \left(\frac{1+z}{1.151} \right)^{-\Gamma_{\text{ph}}} \left(\frac{L_0}{6 \times 10^{52} \text{ erg s}^{-1}} \right) \times \left(\frac{99.3 \text{ GeV}}{E_{\text{max,obs}}} \right)^{1+\Gamma_{\text{ph}}} \left(\frac{-\Gamma_{\text{ph}}}{1.9} \right)^{-5/3} \left(\frac{0.1 \text{ s}}{t_v} \right) \right]^{1/(2-2\Gamma_{\text{ph}})} \quad (5)$$

where the luminosity $L_0 = 4\pi d_L^2 (1+z)^{-\Gamma_{\text{ph}}-2} F_0$, with d_L the luminosity distance (in centimeters) and F_0 the energy flux in νF_ν at 511 keV. N is a numerical parameter of the order of unity obtained from previous studies (G. Vianello et al. 2018), while $E_{\text{max,obs}}$ is the energy of the highest-energy photon, observed at $T_0 + 240.3$ s by the LAT (Table 4). In the interval containing this event [$T_0 + 244$ s, $T_0 + 255$ s], the LAT emission above 100 MeV can be well fitted by a single power-law function with a photon index of $\Gamma_{\text{ph}} = -1.9 \pm 0.1$ (see Table 3). For the minimum variability timescale t_v , we cannot use LAT data because the intense flux of hard X-rays constitutes a major source of noise in every LAT subsystem (see Appendix A for details). Instead, we used $t_v \sim 0.1$ ms obtained from the GBM data (S. Lesage et al. 2023). To estimate the density of target photons at 511 keV, we first

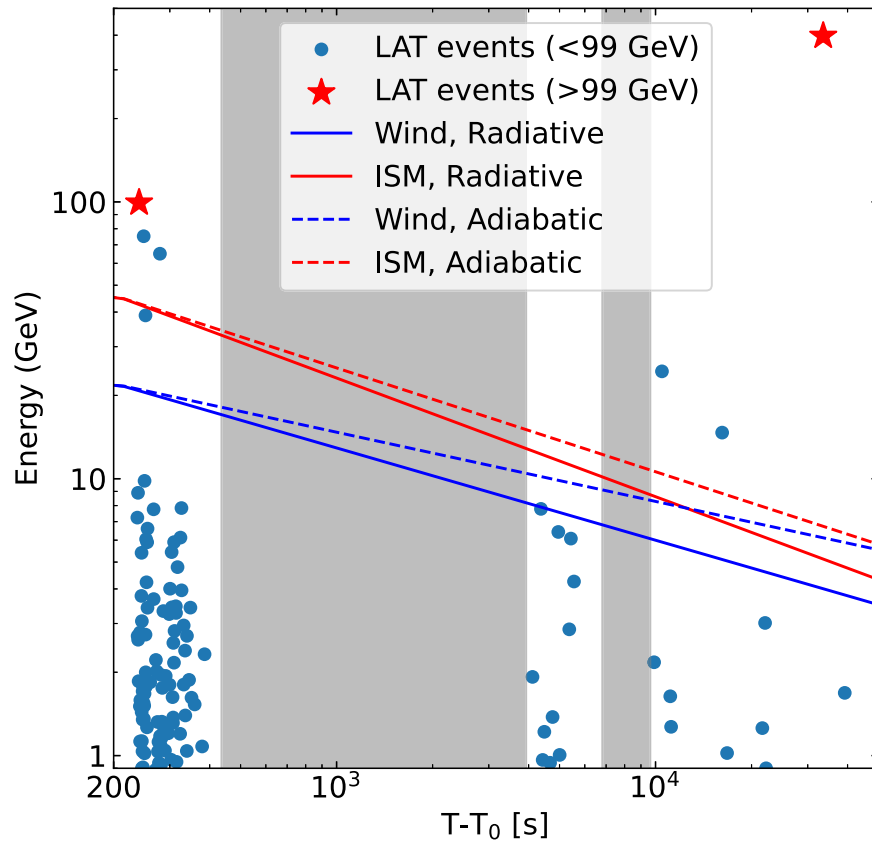


Figure 7. Observed LAT photons with $>90\%$ probabilities of being associated with GRB 221009A. Red stars highlight events above 99 GeV. The lines show the highest possible energies for synchrotron photons based on the synchrotron shock model of the adiabatic/radiative expansion of a fireball in a circumburst medium with an ISM or wind profile, using the initial bulk Lorentz factors calculated from Equation 4 and displayed in Table 5. Photons with energies above these lines exceed the maximum energy allowed by synchrotron emission. The gray shaded areas represent intervals in which GRB 221009A was not in the LAT field of view. Note that such intervals are not displayed for times greater than $T_0 + 10^4$ s.

assumed that low-energy events and high-energy events come from the same physical place (so that the \sim MeV photons that we see are the same that could absorb the GeV events), and, using the results of the analysis presented in S. Lesage et al. (2023), we obtained a value of $\nu F_\nu \sim 10^{-3} \text{ erg cm}^{-2} \text{ s}^{-1}$, which implies $\Gamma_{\text{bulk,min}} \sim 550$. If instead we assume that the high-energy spectral component is separated from the low-energy spectral component, we can use the value of F_0 estimated by extrapolating the LAT power law to 511 keV, obtaining $F_0 \sim 10^{-6} \text{ erg cm}^{-2} \text{ s}^{-1}$ and a value for $\Gamma_{\text{bulk,min}} = 170$. These values obtained taking into account the angular, temporal, and spatial dependencies of the radiation field, are a factor of 2 lower than the values obtained in S. Lesage et al. (2023), which were derived using the assumption of a single zone model. The estimates of the bulk Γ obtained in this analysis are consistent with those obtained using the deceleration timescale (see Section 4.2, Equation (4), and Table 5). Additionally, considering the uncertainties of the model, we cannot firmly establish if the preferred density is a constant ISM as opposed to a wind profile.

However, from the estimated bulk Lorentz factor, we can constrain the maximum synchrotron photon energy (with electrons shock accelerating over the Larmor time and then cooling over the synchrotron cooling time) under the assumption that the extended gamma-ray emission originates from the external forward shock. Figure 7 shows the gamma-ray photons

detected by the LAT compared with the predicted maximum synchrotron photon energy when using $\Gamma = 250$ for the wind case scenario and $\Gamma = 520$ for the ISM case, for both radiative and adiabatic expansion of the fireball. High-energy gamma rays detected by the LAT are in tension with the maximum synchrotron energy during both the prompt and afterglow phases, suggesting that their energies are boosted by inverse Compton scattering.

4.4. Synchrotron, Synchrotron Self-Compton?

To study the spectral evolution of GRB 221009A after the BTI, where the high-energy emission is prominent, we jointly fitted GBM¹⁰¹, LLE, and LAT data. We analyzed the time intervals after the first GBM BTI [$T_0 + 280$ s, $T_0 + 435$ s], using the same binning as in Table 3. In our analysis, we included detectors n7, n8, and b1, which all have a good viewing angle during the interval. In addition, we added LLE and LAT (TRANSIENT_010E) data using the ThreeMLO-GIPLike and FermiLATlike plug-ins. We also calculated the predicted intrinsic spectrum during the various time intervals from the LHAASO analysis to constrain the best-fit model. To this end, we used the best-fit model for the light curve $N(t)$ described in Table S3 of the supplementary material in Z. Cao et al. (2023a; Fit [30, $+\infty$), combined with equation S3 for the evolution of the spectral index $\Gamma_{\text{ph}}(t)$. For a set of

¹⁰¹ We used CSPEC (Continuous Spectroscopy) GBM data.

Table 6Decrement of the Bayesian Evidence ($\Delta \log Z$) with Respect to the Best-fit Model

Interval (seconds from T_0)	SBPL			SBPL +G		
	SBPL	SBPL+G	+PL	+PL	+SBPL	+SBPL
280.6–290.6	413.0	413.1	155.4	143.8	10.9	0.0
290.6–300.6	156.0	155.9	91.4	73.2	18.9	0.0
300.6–325.6	161.5	144.4	146.1	118.7	26.5	0.0
325.6–340.6	137.8	137.9	88.9	89.0	30.8	0.0
340.6–355.6	203.4	203.5	72.9	69.8	5.6	0.0
355.6–380.6	186.2	185.9	63.9	61.1	2.7	0.0
380.6–435.6	472.6	472.7	173.7	173.9	0.4	0.0

Note. For example, the decrease of $\Delta \log Z$ obtained by removing a Gaussian line from the SBPL+G+SBPL model (passing from SBPL+G+SBPL to SBPL+SBPL) can be read in the second-to-last column, while the decrease obtained by removing a second break in the high-energy component (from SBPL+G+SBPL to SBPL+G+PL) can be read in the third-to-last column.

100 energy points from 300 GeV to 5 TeV, we computed the fluxes by randomly sampling the model parameters within their errors and integrating in time. The 16th and the 84th percentiles of the flux distribution define the 68% contour level. Finally, we used the *ThreeML* plug-in *XYLike* that allows flux errors (assumed to be Gaussian) to be taken into account in the fit by computing the χ^2 relative to the assumed model. To find the model that best fits the data, we started from the same model adopted in M. E. Ravasio et al. (2024) for a similar time interval (SBPL). Similarly to M. E. Ravasio et al. (2024), we modeled the spectrum at low energy by adding a Gaussian line (G) with a peak free to vary between 1 MeV and 20 MeV, and a width between 1 MeV and 10 MeV. The decision of whether to add the Gaussian feature was based on minimization of the residuals.

At high energy, we also added an additional PL or a second smoothly broken power law SBPL to mimic the typical “two-hump” SSC spectrum. Given the increase in the number of parameters, we used the Bayesian inference analysis available in *ThreeML* to explore the parameter space, selecting *multinest* (F. Feroz et al. 2009) as a sampler. The combination of these components resulted in six different models, and we used the Bayesian evidence $\log Z$ to compare models¹⁰². The decrease of $\log Z$ with respect to the best-fit model is shown in Table 6. The model with the highest value of $\log Z$ is SBPL+G+SBPL for every time interval. Nevertheless, according to Jeffreys’ scale (H. Jeffreys 1939), the Gaussian line is strongly favored ($\Delta \log Z > 5$) only in the first five intervals, while there is only moderate evidence ($2.5 < \Delta \log Z < 5$) in the sixth interval, and no evidence in the last interval. With the same criterion, but now looking in Table 6 at the values of $\Delta \log Z$ in the SBPL+G+PL column, a break at high energies is always strongly favored.

Figure 8 shows the temporal evolution of the model. The Gaussian peak progressively shifts to lower energies with time, except in the last interval, although then the presence of the Gaussian line component is less significant. If associated with a blueshifted electron–positron annihilation line (M. E. Ravasio et al. 2024), the Doppler factor δ_{ann} implied by the line energy lies in the ~ 10 –20 range. If the annihilation region is proximate

to the prompt continuum emission region, the line’s evolution with time indicates a rapid deceleration of the jet, as suggested in Y.-Q. Zhang et al. (2024). In this scenario, the relatively slow bulk Lorentz factor ($\Gamma \sim 10$ –20) needed to boost the 511 keV line to ~ 5 –10 MeV energies, compared to the much larger value obtained from GeV and TeV observations, suggests that the emission line is probably related to a slower component of the jet or a more slowly evolving shell, as also proposed by M. E. Ravasio et al. (2024).

Such a slow region could be envisaged as connecting to the familiar spine-sheath morphology of extragalactic radio jets emanating from supermassive black holes (SMBHs). Evidence for such lateral structure comes from limb brightening of radio galaxy jets revealed in parsec-scale VLBI observations (e.g., R. A. Laing & A. H. Bridle 2002; M. Giroletti et al. 2004). This has driven the paradigm (e.g., G. Ghisellini et al. 2005) of a mildly relativistic, outer jet, a dense sheath that carries most its kinetic energy and that entrains the external medium, surrounding a highly relativistic, lower-density inner jet (spine) that possesses most of the jet’s angular momentum. Both decelerate rapidly through the drag imposed by entrained circumjet material. When such a configuration is employed in hydrodynamic simulations, with density ratios in the 10–100 range, the spine-sheath structure is preserved uninterrupted despite the generation of extensive turbulence in the shear layer between the two zones (e.g., Z. Meliani et al. 2008). In the GRB context, bulk motions are on average much faster than for SMBH jets. The rate of pair annihilation would be much greater in a denser and slower periphery than in a more tenuous and faster spine, which is consistent with the disparity in bulk motions inferred for the line and from the pair creation transparency arguments in Section 4.3.

Alternatively, it could be argued that the markedly sub-GeV value of the line energy measures Doppler factors that are much lower than the jet Lorentz factor, i.e., $\delta_{\text{ann}} \ll \Gamma$. In this interpretation, proposed by A. Pe’er & B. Zhang (2024), high-latitude (i.e., remote from the jet axis/core) annihilation zones provide a plausible explanation for the observed line energies. This scenario does not require the presence of a slow emission region, but instead relies on a unique combination of high luminosity and a jet Lorentz factor that need to be constrained within fairly narrow ranges of values to account for the observed emission-line fluxes and energies. Consequently, this picture suggests that visibility of such annihilation lines would be rare among the GRB population.

A break in the spectrum at ~ 10 GeV is required to jointly fit LAT and LHAASO-WCDA data in each time bin. The extra component at high energy could be responsible for producing TeV photons, the detection of which within the first 500 s after the trigger was indeed reported by the LHAASO experiment (Y. Huang et al. 2022). The required presence of the extra power law suggests that the high-energy gamma-ray emission is either SSC during the internal dissipation regions or SSC during the external shock in the early phase of the afterglow. In Appendix B, we summarize the results in every time bin for the LAT+GBM analysis, showing numerical values of the best-fit models (Table 9) and the residuals for the SBPL, SBPL+G, and SBPL+G+PL models (figures in Appendix B).

4.5. Is GRB 221009A Really the B.O.A.T.?

To answer this question, we need to put GRB 221009A in the context of other LAT GRBs, comparing some of its

¹⁰² In the statistical literature this term, which is the normalization integral on the right-hand-side of Bayes’ theorem, is often called “marginal likelihood.”

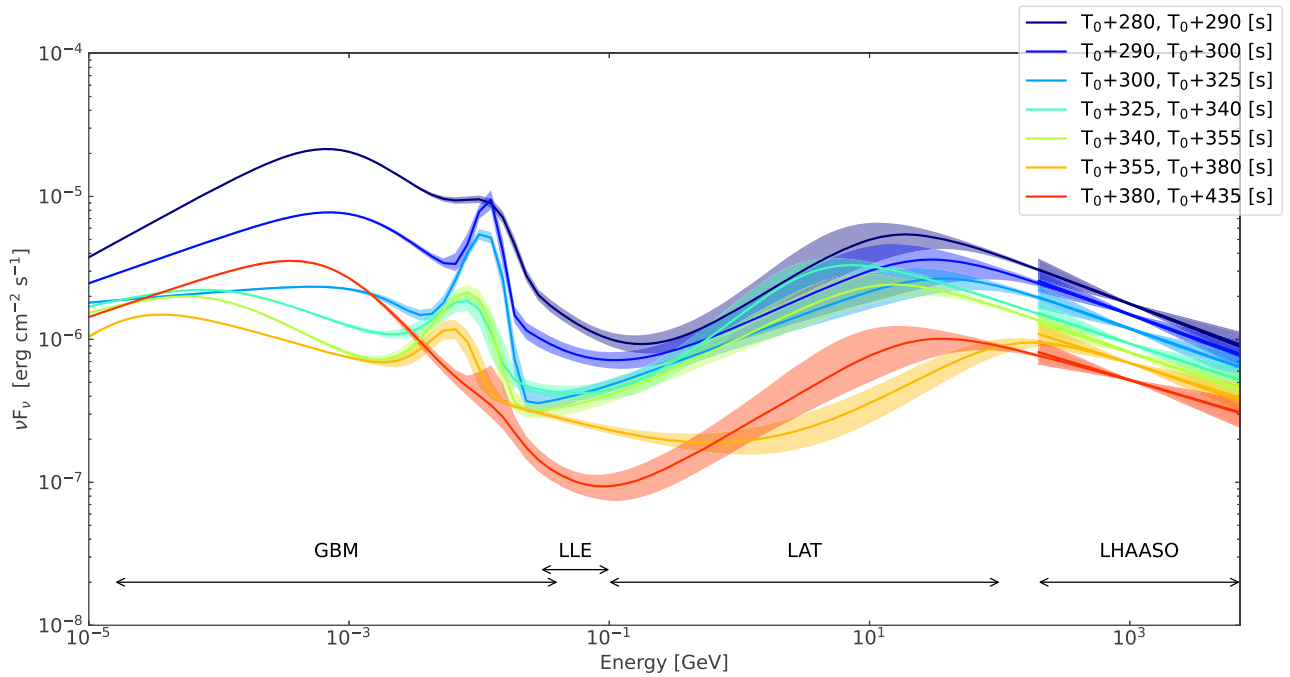


Figure 8. Best-fit model (SBPL+G+SBPL) for the time-resolved joint analysis with 68% confidence level. The arrows at the bottom of the plot indicate the energy band covered by each of the detectors. The overall spectrum exhibits a characteristic two-bump structure typical of synchrotron and SSC, where the first bump corresponds to the synchrotron emission, and the second bump corresponds to the SSC emission. In addition, a Gaussian line is statistically significant in the first five intervals, and only marginally significant (or not significant) in the last two.

Table 7

Fermi-LAT Events with Energies > 100 GeV that Arrived since the Beginning of the Mission within 1° of the Position of the GRB Optical Counterpart

UTC (s)	Energy (GeV)	R.A. (J2000, deg)	Decl. (J2000, deg)	Conv. Type.	Ang. Sep. (deg)
2009-11-01 06:21:03.90	118	288.9	20.0	Back	0.63
2010-03-10 17:30:57.05	107	288.5	19.5	Back	0.31
2015-11-04 12:22:50.10	103	287.7	19.2	Front	0.76
2016-05-01 20:04:42.40	140	287.7	20.6	Front	0.99
2016-12-21 08:42:19.47	268	288.5	20.1	Front	0.38
2017-06-30 08:24:03.47	113	287.4	20.0	Front	0.85
2020-12-30 00:39:41.05	300	287.3	19.9	Front	0.93
2022-10-09 22:36:17.96	398	288.2	19.8	Back	0.02
2023-04-19 10:54:13.46	665	288.3	19.0	Front	0.77

Note. “Back” stands for events converting in the lower part of the tracker as opposed to “Front” events converting in the upper part of the tracker. At these energies, $\Delta E/E \lesssim 10\%$.

characteristics with those in the Second Fermi-LAT GRB Catalog 2FLGC (M. Ajello et al. 2019). Figure 9 shows the fluence and luminosity as a function of time for GRB 221009A and for all of the GRBs detected by the LAT that have known redshifts. We also highlight a few previous record holders: GRB 090510 is still the brightest short¹⁰³ GRB ever detected by the LAT, and still the one whose fluence peaks earliest. GRB 130427A was the previous record holder in terms of both fluence and highest-energy event, while GRB 190114C, also very bright, is the first detection announced at TeV energies. When comparing the two panels of Figure 9, GRB 221009A is an outlier if we consider the fluence light curve, which has an extremely intense pulse lasting several hundred seconds during the prompt phase, as well as late-time emission being on the brightest side of the GRB distribution. On the other hand, if we

take into account its distance, the luminosity of GRB 221009A is comparable with other bright LAT-detected GRBs.

The estimated isotropic energy between 100 MeV and 100 GeV E_{iso} can also be compared with that reported in the 2FLGC (Figure 10, left). Given its proximity, GRB 221009A is surprisingly more energetic than other GRBs at similar redshifts, and it is as energetic as other GRBs at redshift $\gtrsim 2$. Considering the difference in comoving volume confined within $z = 0.151$ and $z \gtrsim 2$, this unequivocally demonstrates that GRB 221009A is an extremely rare event and will likely remain unparalleled in our lifetimes. The right panel of Figure 10 shows the maximum photon energy recorded by the LAT for each GRB and its arrival time. We have indicated both the highest-energy events from GRB 221009A during the prompt emission as well as the 400 GeV event arriving 33 ks after T_0 . An interesting coincidence: for the previous record holder, GRB 130427A (redshift $z = 0.34$; A. J. Levan et al. 2013), the highest-energy event was a 94 GeV photon arriving

¹⁰³ “Short” GRBs have a duration in the MeV energy range of < 2 s; the other ones are classified as “long.”

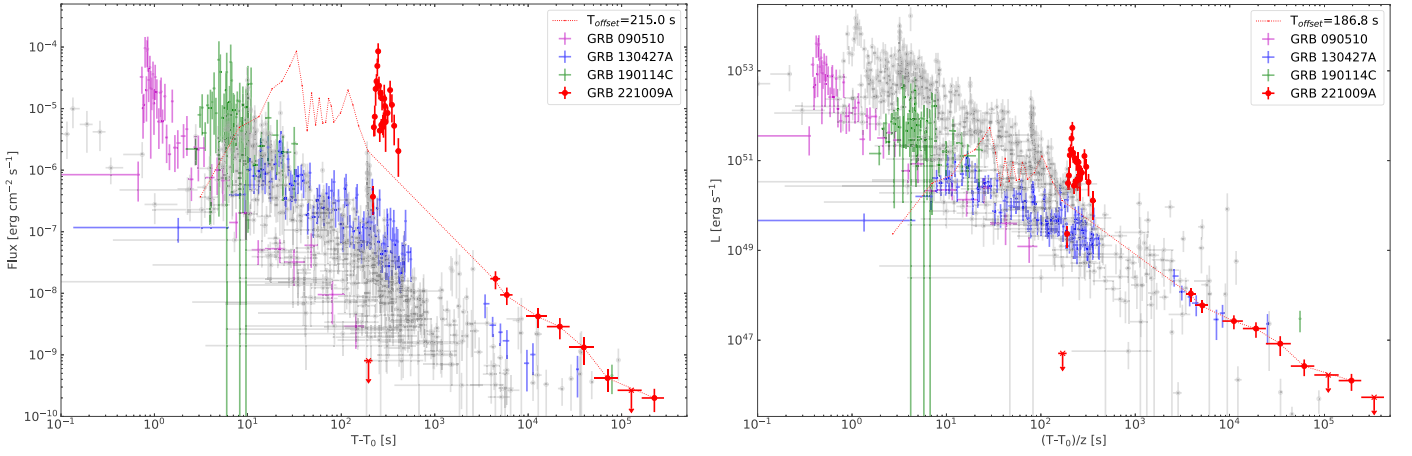


Figure 9. Flux light curves (left panel) and rest-frame luminosity light curves (right panel) in the 100 MeV–100 GeV rest-frame energy range for GRB 221009A (red) and for other LAT-detected GRBs with redshifts included in the 2FLGC (gray). Three previous record-holder GRBs are highlighted in different marker colors. The red dashed line, which indicates the light curve of GRB 221009A shifted by 215 s (i.e., the estimated onset time T_{on}), shows how the light curve would look if the GBM had triggered on the beginning of the bright pulse, and it is shown only for comparison with the other GRBs for which the triggering pulse could have been below the threshold. GRB 221009A is particularly bright thanks to its proximity.

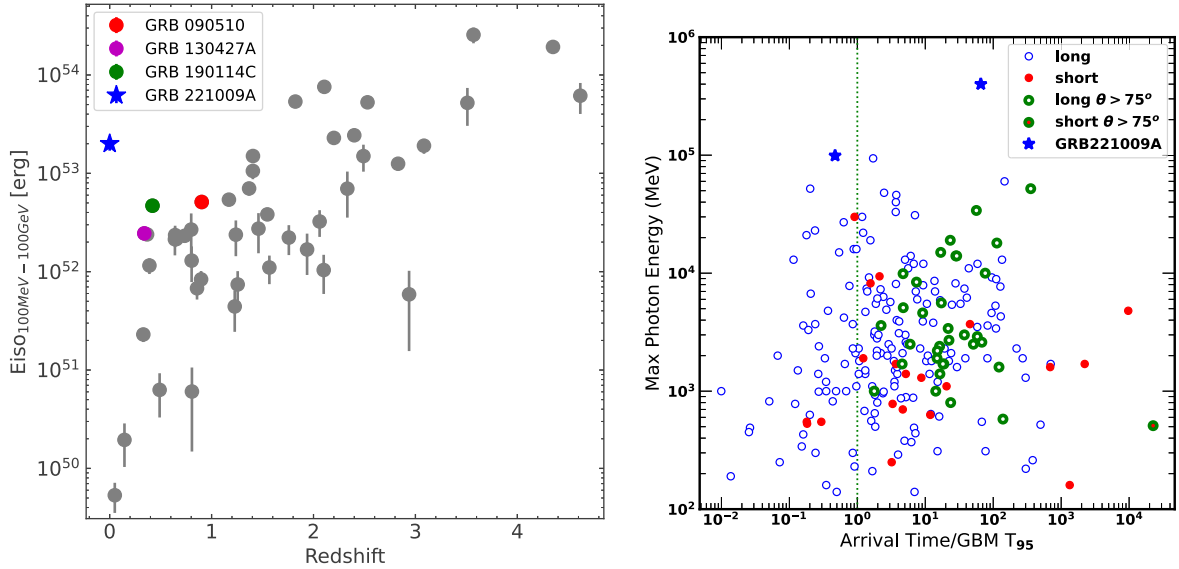


Figure 10. Left: distribution of the isotropic equivalent energies between 100 MeV and 100 GeV (E_{iso}) as a function of redshift for the sample of Fermi-LAT detected GRBs. The blue star highlights GRB 221009A. As in Figure 9, we have highlighted the previous record holders with different marker colors. In terms of E_{iso} , GRB 221009A is clearly an outlier among GRBs at $z < 2$. Right: maximum photon energy vs. arrival time for LAT GRB photons normalized to the GRB T_{95} , the total duration of the burst (the dashed vertical line indicates unity). Blue circles/red filled circles are long/short GRBs, and green circles highlight LAT-detected GRBs that were outside the field of view at the time of the GBM trigger. For GRB 221009A, we display both the highest-energy event during the prompt emission (at 99 GeV) and the highest-energy event during the temporally extended emission (at 400 GeV).

at 243.13 s after the trigger, almost exactly the same numbers as for the 99 GeV event from GRB 221009A. With respect to the population of LAT GRBs, the 400 GeV photon possibly associated with GRB 221009A clearly stands out. The association of this event with GRB 221009A will be discussed in detail in Section 4.7.

By two other measures, GRB 221009A can be classified as the B.O.A.T.: the fluence integrated over the entire emission and the estimated duration $T_{\text{LAT},100}$. Figure 11 shows the fluence from 0.1–100 GeV measured by the LAT as a function of the 10 keV–1 MeV fluence measured by the GBM (left panel), and as a function of $T_{\text{LAT},100}$ (right panel). The ratio of the 0.1–100 GeV to the 10 keV–1 MeV fluence is close to 0.1, compatible with the rest of the long GRB population. In the fluence-duration scatter plot, GRB 221009A clearly stands out

as the longest (with $T_{\text{LAT},100} \sim 1.8 \times 10^5$ s) and the brightest GRB yet observed by the LAT.

4.6. Closure Relation and Density Profile

During the temporally extended emission, the observed LAT photon index is $\Gamma_{\text{ph}} \sim -2.2$, while the observed temporal index $\alpha_{\text{LAT}} = -1.2 \pm 0.1$. Considering the spectral index $\beta = -\Gamma_{\text{ph}} - 1$, we can test the closure relations (D. Tak et al. 2019). In particular, for $\nu_{\text{obs}} > \nu_c$, with ν_c the synchrotron cooling frequency, $\alpha = (3/2)\Gamma_{\text{ph}} + 2 \sim -1.3$ for both the ISM case and the wind profile, which is compatible with α_{LAT} . For $\nu_{\text{obs}} < \nu_c$, $\alpha = (3/2)(\Gamma_{\text{ph}} + 1) \sim -1.8$ for the ISM case while $\alpha = (3/2)\Gamma_{\text{ph}} + 1 \sim -2.3$ for the wind case, where both are in tension with the observed LAT photon index.

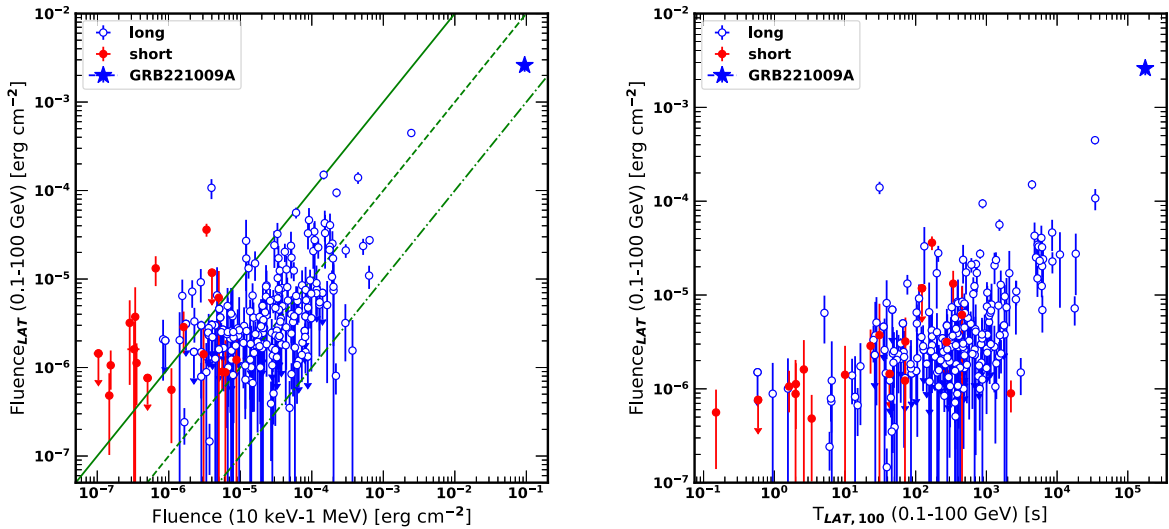


Figure 11. Left: fluence in the 0.1–100 GeV energy range integrated over the entire duration of the high-energy emission detected by the LAT compared to the 10 keV–1 MeV fluence, as measured by the GBM (S. Lesage et al. 2023). The green lines correspond to the fluence in the 0.1–100 GeV energy range being 1 (solid), 0.1 (dashed), and 0.01 (dotted–dashed) times the fluence in the lower-energy band. Right: fluence in the 0.1–100 GeV energy band as a function of the GRB duration estimated using the $T_{\text{LAT},100}$ parameter as in M. Ajello et al. (2019). In both panels, GRB 221009A is marked with a blue star.

The derived spectral index from Swift-XRT in the 0.3–10 keV band from 1 ks to 6.3 ks from T_0 is $\Gamma_{\text{ph,XRT}} = -1.91 \pm 0.09$, while the combined Swift, MAXI, and NICER light curve can be fitted with a broken power law with indices $\alpha_{1,X} = -1.498 \pm 0.004$ and $\alpha_{2,X} = -1.672 \pm 0.008$, with a break at $T = T_0 + (7.9 \pm 1.1) \times 10^4$ s (M. A. Williams et al. 2023). For $\nu_{\text{obs}} > \nu_c$, both the ISM and wind scenario predict an expected decay index $\alpha = -0.85$, and for $\nu_{\text{obs}} < \nu_c$ $\alpha = -1.35$ for the ISM case scenario and $\alpha = -1.85$ for the wind case. As also noted by M. A. Williams et al. (2023), standard closure relations (J. L. Racusin et al. 2009) fail to reproduce the behavior of the X-ray afterglow emission, and the density profile cannot be firmly constrained.

4.7. The 400 GeV Event

The highest-energy event detected with a direction compatible with the location of GRB 221009A is a 400 GeV photon, which is converted in the lower part of the tracker, where the thicker tungsten converter layers cause a slightly worst point-spread function (PSF). It arrived approximately 33 ks after the GBM trigger time.

We performed a series of statistical tests of significance of this event.¹⁰⁴ First, we examined the LAT mission data set from the beginning of the mission until 2024 October, extracting all SOURCE events within a region of interest (ROI) of 1° radius centered at the optical location of the GRB with energies >100 GeV. Table 7 shows the arrival time, the energy, the reconstructed direction, and the conversion type for each of these events, and Figure 12 shows their arrival directions and times. The highest-energy event ever detected by LAT in this ROI is a 665 GeV front-converting event, which arrived 191.9 days after the GBM trigger. This event is 0.77° off the optical localization of GRB 221009A, not quite compatible if we consider the PSF of the event. In contrast, the 400 GeV back-converting aligns well with the optical position.

Comparing T_{off} , the accumulated time that the ROI was in the LAT field of view (approximately 5.1 yr) and T_{in} , the accumulated time from T_0 to the detection of the 400 GeV (approximately 3.8 hr), the probability p of observing $N_{\text{sig}} = 1$ event above 100 GeV during the T_{in} when $N_{\text{bkg}} = 8$ events have been detected during T_{off} is calculated using the method described in T. P. Li & Y. Q. Ma (1983) and corresponds to $p = 2.1 \times 10^{-4}$ (3.5σ). This probability is slightly lower ($p = 3.3 \times 10^{-5}$, or 4.0σ) if we consider that only one event ($N_{\text{bkg}} = 1$) is compatible with the 95% containment radius, and it becomes $p = 7.6 \times 10^{-6}$ (4.3σ) considering that no other events at 400 GeV or above are consistent with GRB 221009A ($N_{\text{bkg}} \rightarrow 0$).

On the assumption that the 400 GeV event indeed came from the GRB, we performed a second test to check if this event is compatible with the low-energy part of the spectrum. To do so, we repeated the spectral analysis between 27.81 ks and 51.09 ks, selecting this time only the events with energies <100 GeV. The derived photon index is $\Gamma_{\text{ph}} = -2.5 \pm 0.3$. Then we computed the exposure above 400 GeV during the same time interval and assumed the spectral index Γ_{ph} . The number of expected events N_{exp} is given by the product of the integrated flux and the exposure.

The number of expected events above 400 GeV varies from $N_{\text{exp}} = 4.3 \times 10^{-6}$ to $N_{\text{exp}} = 5.8 \times 10^{-4}$ (at 68% confidence level, c.l.), which corresponds to a probability ranging from 4.4σ to 3.2σ to observe at least one event.

If we lower the threshold to 360 GeV, which results from a 10% energy resolution at 400 GeV, the number of expected events above this threshold now ranges from $N_{\text{exp}} = 7.3 \times 10^{-6}$ to $N_{\text{exp}} = 1.0 \times 10^{-3}$ or probabilities from 4.3σ to 3.1σ .

Finally, a similar approach that allows us to take into account the uncertainty on the flux with its probability density function is to compute the upper bound of the flux, by increasing the c.l. until $N_{\text{exp}} = 1$. The corresponding c.l. is 0.999970, or a probability of 3.1×10^{-5} (4.0σ) or a probability of 4.7×10^{-5} (3.9σ) for the lower-energy threshold.

¹⁰⁴ With “event,” we mean the classification of the trigger as a gamma ray.

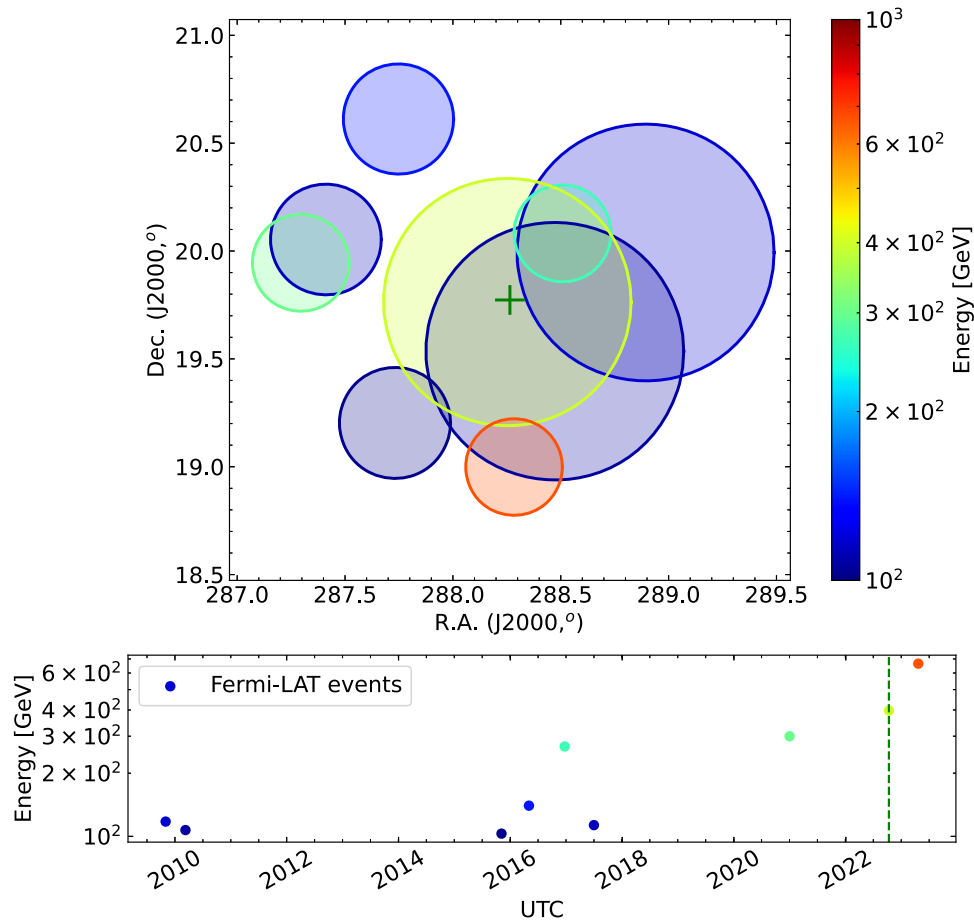


Figure 12. Top: arrival directions of all events with energies >100 GeV within 1° of the GRB location (green marker). The circles' radii are equal to the 95% containment PSF radius, and their colors represent their energies. Bottom: arrival times of these events (for precise arrival times, see Table 7). The green dashed line corresponds to the Fermi-GBM trigger time.

In summary, considering the entire Fermi mission elapsed time, the chance probability that an event above 100 GeV is detected within 33 ks after the GBM trigger, in spatial coincidence with the GRB, is approximately 4σ , indicating that we cannot firmly exclude that the photon is a background event. If the photon was indeed a background event, given the proximity to the Galactic plane and the absence of nearby point sources, it would likely be associated with diffuse emission from the Milky Way or from the unresolved population of blazars that constitute the majority of the extragalactic gamma-ray background (M. Ackermann et al. 2016).

On the other hand, if we assume that the 400 GeV event is indeed associated with the GRB, the probability that the event is generated from the high-energy extrapolation of the low-energy part of the spectrum is relatively low (between 3.1σ and 4.4σ), suggesting that this is unlikely to be the case. A preliminary HAWC upper limit (H. Ayala & HAWC Collaboration 2022) was calculated during a time interval that included the high-energy event, concluding that no bright emission was detected at TeV energies. A more in-depth analysis is currently underway and will help to assess the origin of this event.

Electromagnetic cascades from high-energy cosmic-ray interactions with the magnetic fields of the host galaxies or TeV photons interacting with the EBL could, in principle,

explain such a delayed emission. In the latter scenario, the resulting electron–positron pairs would in turn interact with the cosmic microwave background via the inverse Compton (IC) process, leading to a secondary cascade of multi-GeV photons, which could be delayed with respect to the GRB depending on the intergalactic magnetic field strength (see, e.g., A. Neronov & D. V. Semikoz 2009). As a first estimate, producing a 400 GeV cascade photon would require a ~ 23 TeV primary photon assuming an equal distribution of energy among the pairs, while a 33 ks delay implies a $\sim 2 \times 10^{-18}$ G magnetic field. The exceptionally high energies reported by LHAASO would make this scenario feasible, but incompatible with intergalactic magnetic field limits derived from blazar observations ($B > 3 \times 10^{-16}$ G for conservative blazar duty cycles; M. Ackermann et al. 2018). This tension could be alleviated if plasma instabilities in voids dominate particle cascade losses instead of IC, preventing persistent pair-beams induced by blazars from radiating at GeV energies (A. E. Broderick et al. 2012). However, cascade emission would suggest an additional smooth component alongside the afterglow (S. Razzaque et al. 2004; K. Murase et al. 2009), without a significant bump around 9.3 hr. Estimates of these cascade components as produced by GRBs are highly uncertain and require a complete multiwavelength characterization (P. Da Vela et al. 2023).

5. Summary and Conclusions

GRB 221009A is by far the brightest GRB ever detected by the LAT. In this analysis, we presented a comprehensive examination of this unique and intense burst.

The Fermi-GBM instrument was triggered by an initial pulse, which was also observable in LAT data. This triggering pulse was well fitted by a CPL model with a particularly high peak energy of ~ 15 MeV, which decreased to roughly 300 keV within the first 20 s. The high-energy emission observed by the LAT during the triggering pulse preceded the low-energy emission observed by the GBM, which is an uncommon feature in LAT-detected GRBs (M. Ajello et al. 2019).

During the prompt phase, we identified a 64 s long BTI, [$T_0 + 216.6$ s, $T_0 + 280.6$ s], during which extremely high fluxes of X-rays and soft gamma rays created an additional noise in all of the LAT subsystems. Thanks to a special analysis, including a dedicated event reconstruction and selection, we were able to successfully analyze the LAT data and derive the GRB light curve during the BTI.

During the first 450 s, the >100 MeV flux was rapidly variable with several pulses closely spaced in time. We were able to clearly characterize the two brightest ones, the first peaking at $T_0 + 247.4 \pm 0.9$ s and the second at $T_0 + 330 \pm 10$ s, although other less-significant pulses are visible in the LAT light curve. The peak of the LAT emission is not synchronized with either of the two bright pulses at ~ 230 s and ~ 270 s in the GBM light curve. This can be explained by the rapid variability of the spectral index, a typical signature of internal shock emission. We performed a time-resolved spectral analysis after the LAT BTI, combining data from GBM and LAT, and incorporating the results of the LHAASO-WCDA analysis. This study showed that a broken smoothly joined power law, which we interpreted as the synchrotron self-Compton component, is required to describe the high-energy part of the emission. The presence of a ~ 10 MeV line was also statistically favored and, if associated with a blueshifted electron-positron annihilation line (M. E. Ravasio et al. 2024), suggests that the emission line is probably related to a slower component of the jet or a slower-evolving shell, as also proposed by M. E. Ravasio et al. (2024), and its evolution with time indicates a rapid deceleration of this component, as suggested in Y.-Q. Zhang et al. (2024).

The late-time emission decayed as a power law, but extrapolation of the late-time emission during the first 450 s showed that this component, which is commonly associated with the afterglow, was only a subdominant component. This suggests that the afterglow began during the prompt emission. A fit of the light curve required multiple components, two of which were necessary to reproduce the general behavior during the prompt phase, and the third was needed to reproduce the late-time emission. This last component could peak as early as $T_0 + 230$ s (rest frame), which corresponds to a deceleration time of 24 s. According to the standard fireball model, this corresponds to a bulk Lorentz factor of 230 (400) in the wind (ISM) case scenario. Under the assumption of radiative or adiabatic expansion, high-energy events observed by the LAT are incompatible with a synchrotron origin, as seen also in GRB 130427A (M. Ackermann et al. 2014) and in GRB 190114C (M. Ajello et al. 2020). In addition, the joint analysis of GBM and LAT data showed the presence of an additional component at high energies with a photon index Γ_{ph} ranging from -1.7 to -1.4 . This suggests that high-energy

events were more likely to be related to this extra component identified as SSC, as also suggested by M. Tavani et al. (2023) from the analysis of AGILE data. In this scenario, the keV to MeV afterglow observed by the GBM up to $\sim 10^4$ s would be the synchrotron emission, although whether this emission could extend up to ~ 33 ks to explain the 400 GeV event detection is not clear. However, the absence of MeV synchrotron emission disfavors an interpretation of the late-time high-energy events as due to SSC. A broadband study of the afterglow at >0.5 day after the GBM trigger of GRB 221009A using optical, X-ray, and gamma-ray data is presented in D. Tak et al. (2025), and confirms that the synchrotron process can explain the multi-wavelength afterglow emission and its late-time evolution. A spectral cutoff of 4.5 GeV is also found in the time integrated spectra between 1.2 and 2.1 days after the trigger, showing the important contribution of Fermi-LAT in the study of GRB afterglow emission models. On the other hand, interpreting these events as TeV electromagnetic cascades from TeV events interacting with the EBL is difficult because of the particularly low magnetic fields that would be required to explain the 33 ks delay. We cannot definitively say whether these events originate from external Compton emission or from another source. Overall, GRB 221009A stands out compared to other LAT GRBs, and its energetic nature, given its proximity, confirms that it is extremely rare (E. Burns et al. 2023b).

Acknowledgments

We dedicate this paper to the memory of our colleague Magnus Axelsson, who passed away prematurely in 2022 July. Magnus's kindness, competence, and helpfulness made him one of our most valued colleagues. He played a central role in Fermi GRB science, and his presence on the Fermi team is greatly missed. More than a colleague, he was a friend.

The Fermi-LAT Collaboration acknowledges generous ongoing support from a number of agencies and institutes that have supported both the development and the operation of the LAT as well as scientific data analysis. These include the National Aeronautics and Space Administration and the Department of Energy in the United States, the Commissariat à l'Energie Atomique and the Centre National de la Recherche Scientifique / Institut National de Physique Nucléaire et de Physique des Particules in France, the Agenzia Spaziale Italiana and the Istituto Nazionale di Fisica Nucleare in Italy, the Ministry of Education, Culture, Sports, Science and Technology (MEXT), High Energy Accelerator Research Organization (KEK) and Japan Aerospace Exploration Agency (JAXA) in Japan, and the K. A. Wallenberg Foundation, the Swedish Research Council and the Swedish National Space Board in Sweden.

Additional support for science analysis during the operations phase is gratefully acknowledged from the Istituto Nazionale di Astrofisica in Italy and the Centre National d'Études Spatiales in France. This work performed in part under DOE contract DE-AC02-76SF00515.

W. M. is funded by National Research Council of Thailand (NRCT): High-Potential Research Team Grant Program (N42A650868).

This work made use of data supplied by the UK Swift Science Data Centre at the University of Leicester.

Appendix A

Flux Measurement during the BTI

The LAT energy range defines the part of the GRB emission that is considered as a signal for the LAT. In contrast, the intense emission of GRB 221009A below ~ 30 MeV is actually a source of noise in the instrument. For clarity's sake, we name the GRB emission below and above ~ 30 MeV the low-energy (LE) and high-energy (HE) emissions, respectively, keeping in mind that this denomination does not imply that these two parts of the GRB emission are not due to the same physical process.

During the brightest part of the prompt emission of GRB 221009A, the extra noise produced by the LE emission is so important that it severely impacts the standard event reconstruction, preventing us from performing a standard data analysis. To overcome this limitation and to be able to measure the GRB HE emission, we have modified the event reconstruction and devised a new event selection, as well as original analysis and validation methods.

In this appendix, we first quantify the effect of the extra noise on the instrument and then present our dedicated data analysis to characterize the HE emission of GRB 221009A. To do so, we make extensive use of simulations of photons in the LAT based on the Geant4 Monte Carlo toolkit (S. Agostinelli et al. 2003; J. Allison et al. 2006), including the simulation of photons between 10 MeV and 10 GeV produced for the LLE analysis. All time intervals are indicated in seconds with respect to the GRB trigger T_0 .

A.1. Effect of the Intense X-Ray and Soft Gamma-Ray Flux on the LAT Instrument

A.1.1. Energy Estimation

Below ~ 10 GeV, the standard Pass 8 energy reconstruction (W. Atwood et al. 2013) makes use of the tracker and the calorimeter information, the former being critical for gamma rays below ~ 1 GeV. We estimate the energy deposited in the tracker from the number of strips fired in the thin and thick sections of the tracker. For the calorimeter, we perform a clustering of the energy deposits and use the highest-energy cluster to compute the event energy.

Because the numbers of fired strips are computed in the whole tracker, they include the strips due to the extra noise. In order to quantify this noise contribution to the energy estimation, we design an alternative way to count the fired strips, namely within a cone around the event track axis ($d < 20 + 0.1 \times l$, where d and l are the distance in millimeters to and along the track axis, respectively, with $l = 0$ at the conversion point and only $l > 0$ is considered). Using simulations, we find that the cone selection reduces the number of fired strips included in the tally by $\sim 40\%$, and the resulting energy estimation is thus affected by a negative bias that ranges from 40% at 60 MeV to 10% at 1 GeV. We correct for this bias to compute the alternative energy estimator E_{cor} .

The difference between the standard and modified energies corresponds to the additional equivalent energy due to the extra noise in the tracker induced by the GRB LE flux. Figure 13 shows the average of this difference as a function of time for events with at least one track passing the trigger and gamma filter. Before 218 s and after 290 s, the extra energy is close to 0, as during normal conditions, but during most of the time interval [218 s, 290 s], the extra energy is clearly not negligible. As a consequence, the standard energy evaluation is strongly

biased, and we need to develop a new event energy estimation. One can see two peaks of activity, P1 around 230 s and P2 around 260 s, that match the double-peak structure of the GBM light curve reported in S. Lesage et al. (2023). In the interpeak (IP) period, the extra energy reduces almost to 0, which means that the impact of the GRB LE flux during the IP period is very much reduced compared to P1 and P2.

Regarding the impact of the extra noise on the calorimeter reconstruction, it must be noted first that this impact is naturally mitigated by the clustering introduced in Pass 8. The calorimeter is much denser than the tracker, so the X-rays and soft gamma rays deposit their energy over shorter distances. During the prompt phase, the $-Y$ face of the LAT¹⁰⁵ faced the GRB, and the noise-induced clusters are expected to lie close to the $-Y$ edge of the calorimeter. This is what we observe, as can be seen in Figure 14, for events with at least one track passing the trigger and gamma filter. During P1 and P2, most events have at least one cluster in the calorimeter, and its position lies in the $-Y$ half of the instrument. Comparing the energies of the clusters close to the $-Y$ edge and the $+Y$ edge allows us to quantify the additional energy due to the extra noise in the calorimeter: it is, most of the time, above 10 MeV and can reach 100 MeV. The situation is very different for the IP interval, during which the extra energy is < 10 MeV.

Because the first cluster energy information cannot be used during P1 and P2, we choose to rely only on the tracker information to estimate the event energies during the BTI. As described above, we use the number of fired strips within a cone around the event track axis to compute E_{tkr} . In order to characterize the performance of this energy estimator and especially to check the energy range in which it is usable, we look at the true energy median and the true energy 68% containment interval as a function of E_{tkr} . They are shown in Figure 15 for a simulation of a power-law spectrum, for two spectral indices (-2.5 and -1.5). One can see that the E_{tkr} energy estimator does rather poorly at low energies: the true energy median is almost constant for $E_{\text{tkr}} < 100$ MeV, and therefore E_{tkr} can only be used above 100 MeV.

A.1.2. Estimation of the Trigger and Onboard Filter Efficiency

In addition to creating extra noise in the tracker and the calorimeter, the GRB LE flux also produced signals in the ACD. Since the ACD is instrumental to the trigger and the onboard filter selection, we must check whether the extra noise in the ACD significantly changed the trigger and filter efficiency.

To be recorded, an incoming photon must trigger the LAT and pass the onboard gamma-ray filter. The LAT trigger system defines several sets of conditions that are called trigger engines (M. Ackermann et al. 2012). Two trigger engines are designed to accept gamma rays. Trigger engine 6 requires at least one calorimeter CsI crystal with more than 1 GeV, which corresponds to relatively high-energy gamma rays (~ 5 GeV). Lower-energy gamma rays, which do not pass this condition, are accepted by trigger engine 7, which requires a trigger signal from one tracker tower and no signal above the veto threshold (~ 0.45 of the signal of a minimum ionizing particle) in any of the ACD tiles above the tracker tower. The onboard gamma-ray

¹⁰⁵ The z -axis of the instrument reference frame corresponds to the LAT boresight.

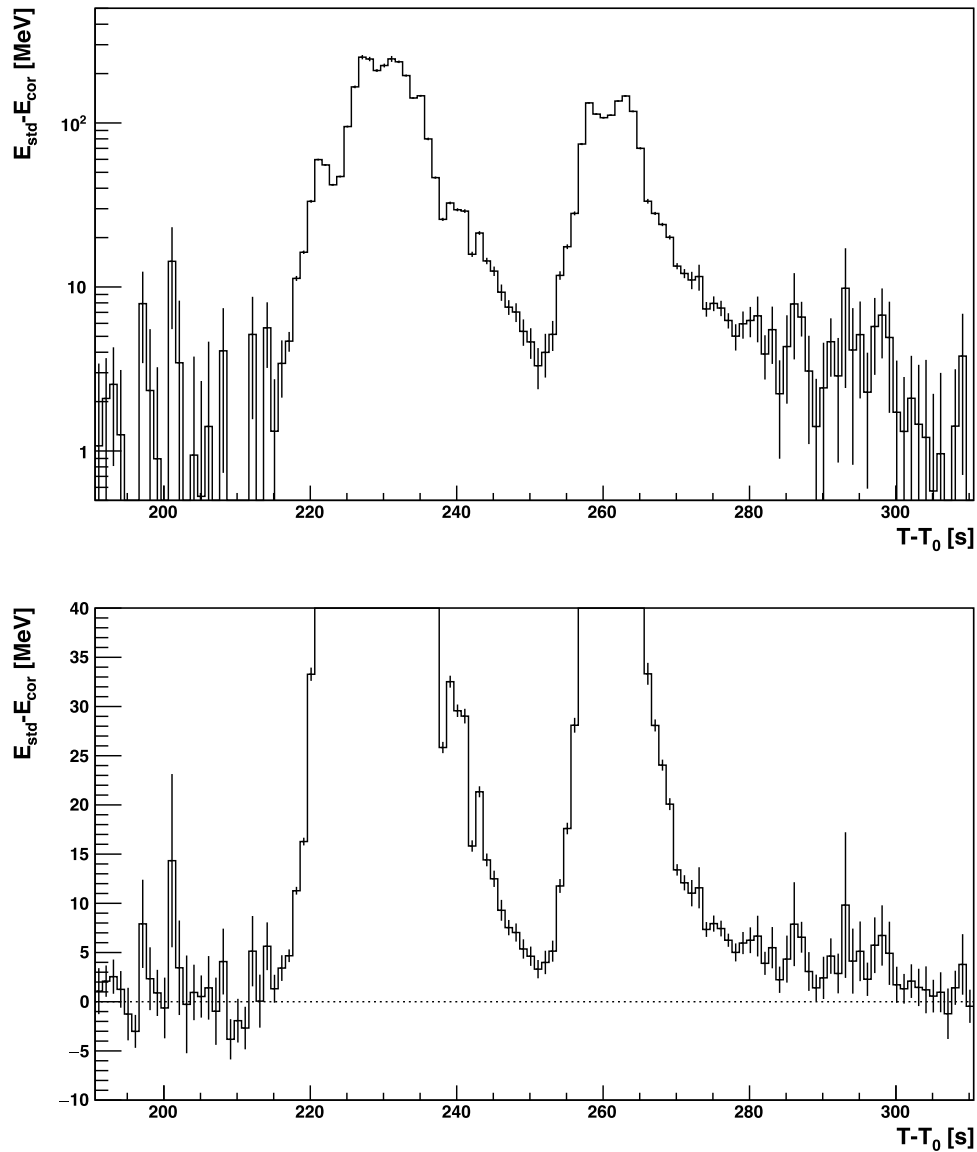


Figure 13. Average difference as a function of time since the GBM trigger between the reconstructed energy using the standard algorithm and the new modified energy estimator in log scale (top) and linear scale (bottom). This difference corresponds to the additional equivalent energy due to the extra noise in the tracker induced by the GRB LE flux.

filter performs a sequence of veto tests that depend on the event topology. An important case is trigger engine 7 events without any calorimeter CsI crystal collecting more than 100 MeV: one ACD tile above the veto threshold is enough to reject these events.

Verifying a selection efficiency implies comparing it with a reference. Very fortunately, the Earth limb came into the LAT field of view at about the time of the GBM trigger, providing a reference signal that we use to check the trigger and gamma filter efficiencies. The Earth-limb signal in the LAT depends on the position and orientation of the spacecraft. We have selected a reference data set including about 60 hr¹⁰⁶ in which the satellite has a position/orientation very close to that between 100 and 1000 s after the GRB trigger. Using the reference data set, we prepared the live-time corrected zenith angle θ_{zen}

distribution for a set of bins in geocentric longitude and latitude (the longitude and latitude bin widths are 10° and 0.5° , respectively). Then, for a given time interval during the GRB emission, we construct the reference θ_{zen} template by adding the θ_{zen} distributions scaled by the live time in each of the geocentric longitude and latitude bins during the time interval.

For the verification of trigger and gamma filter efficiencies, we use trigger engine 7 events that passed the gamma filter, with at least one track and without any calorimeter CsI crystal collecting more than 100 MeV. The latter condition allows the selection to be sensitive to the presence of any ACD tile veto. To increase the significance of the Earth-limb signal, we also require that $E_{\text{tkr}} > 125$ MeV.

Figure 16 (left) shows the reference distribution for the time interval [600.6, 650.6]. The Earth-limb peak is clearly visible on top of a broader background distribution due to charged cosmic rays as well as celestial gamma rays. Above 80° zenith angle, the background distribution is assumed to be a piecewise

¹⁰⁶ Between 2020 September 1, at 04:09:09.000 UTC and 2022 November 20, at 14:35:11.000 UTC.

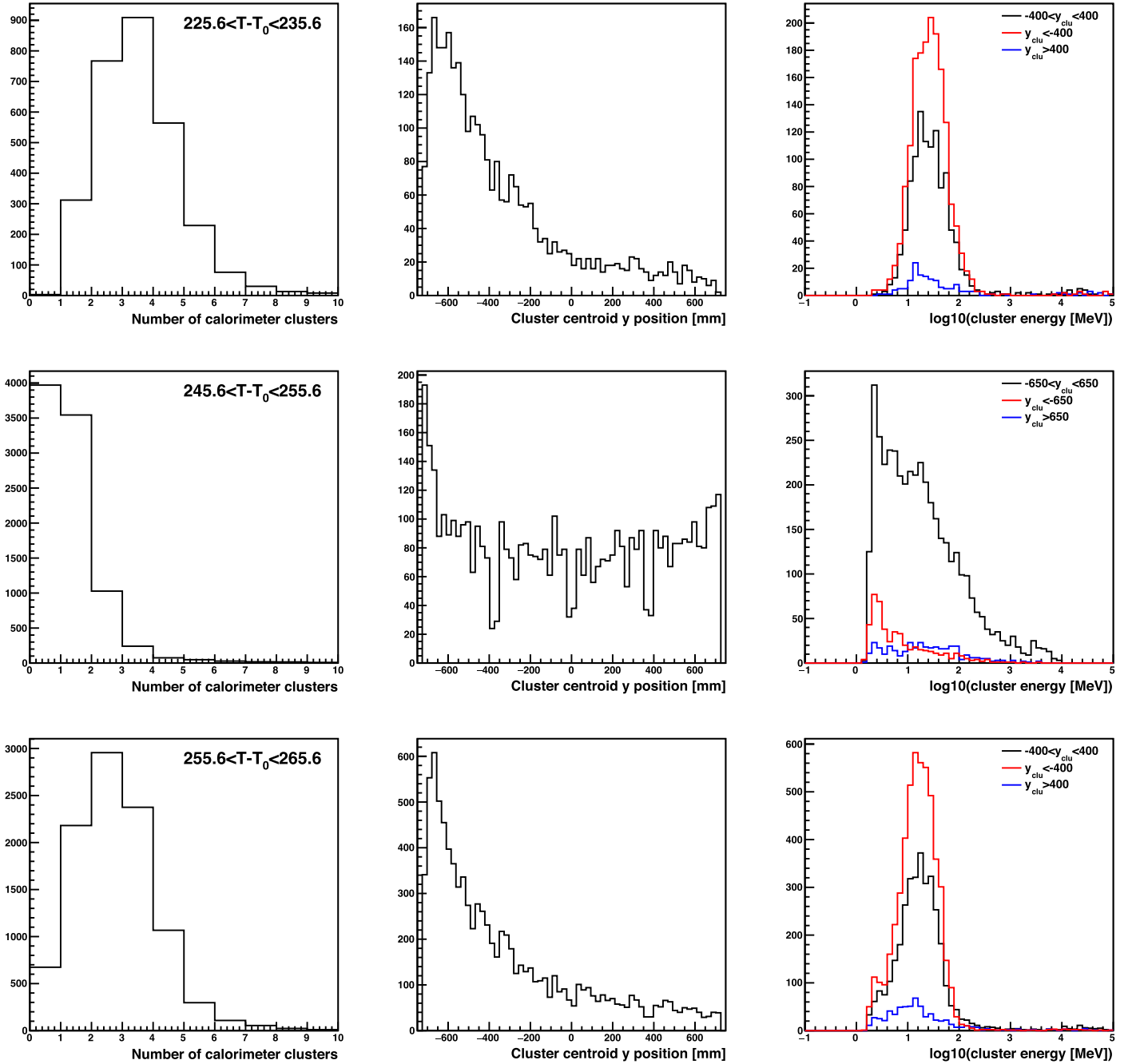


Figure 14. The number of calorimeter clusters (left), the y -position of the highest-energy cluster (center), and its energy depending on whether or not it is close to the $-Y$ face (right) for events with at least one track passing the trigger and gamma filter in the time interval [225.6 s, 235.6 s] (top), [245.6 s, 255.6 s] (middle), and [255.6 s, 265.6 s] (bottom). The distributions of the y -position of the highest-energy cluster show that the extra noise induced in the calorimeter by the GRB LE flux is located in the $-Y$ face of the calorimeter. Comparing the energy distribution of the clusters close to the $-Y$ and $+Y$ faces (red and blue histograms, respectively) allows for an estimation of the equivalent additional energy due to the extra noise in the calorimeter.

linear function defined by four parameters b_{80} , b_{100} , b_{116} , and b_{132} , the background levels at $\theta_{\text{zen}} = 80, 100, 116$, and 132° , respectively, with b_{132} fixed to 0. The Earth-limb peak is modeled as a sum of two Gaussians centered on $\sim 113^\circ$. Fitting several reference templates of 50 s time intervals above 80° , we find that the background ratio b_{116}/b_{100} fluctuates between 0.25 and 0.5. As a consequence, we assume two hypotheses for the background distribution: $b_{116} = b_{100}/4$ and $b_{100}/2$. For each background hypothesis, the fit of the reference distribution allows us to derive the reference background template, as shown in Figure 16 (left). The signal template is simply defined

by subtracting the background template from the reference distribution.

For any time interval during the GRB emission, we fit the θ_{zen} distribution with the sum of the background and signal templates, weighted by the free parameters of the fit, f_b and f_s , respectively. The relative efficiency with respect to normal conditions is directly given by f_s . The result of the fit for the time interval [600.6, 650.6] is shown in Figure 16 (right). For each background hypothesis, the fit gives f_s and δf_s , its uncertainty. To combine the results of the two background hypotheses, we use the minimum of $f_s - \delta f_s$ and the maximum

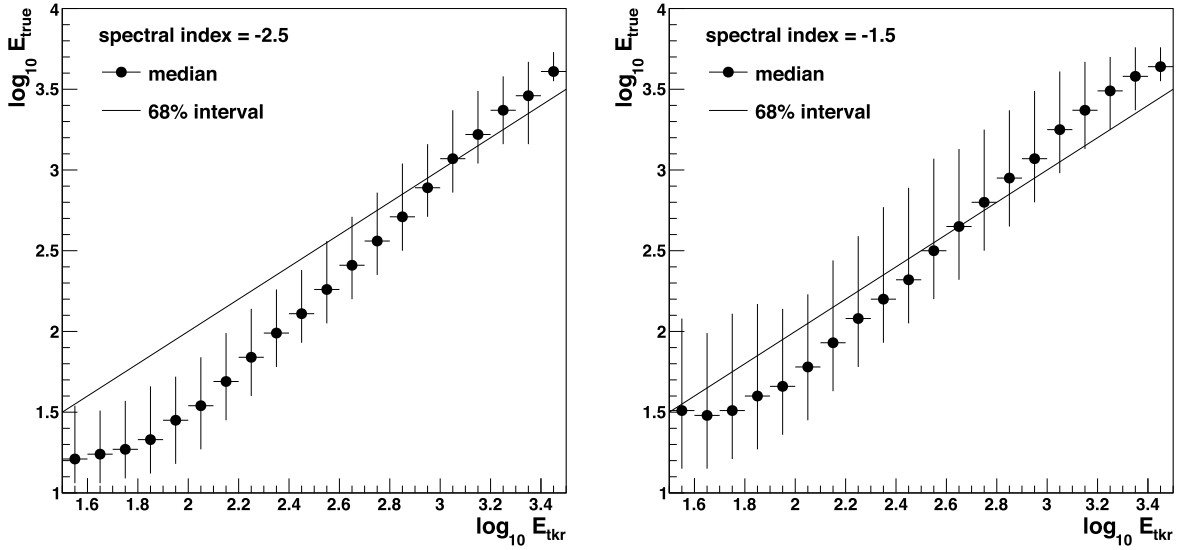


Figure 15. Characterization of the energy estimator E_{tkr} . Left: true energy median (dots) and 68% interval (vertical bars) as a function of $\log_{10} E_{\text{tkr}}$ for a simulation of a gamma-ray source with a spectral index of -2.5 . The dashed line corresponds to equality between the true energy median and E_{tkr} . Right: same but with a spectral index of -1.5 . For $E_{\text{tkr}} < 100$ MeV, the true energy median is almost constant, and therefore E_{tkr} can only be used above 100 MeV.

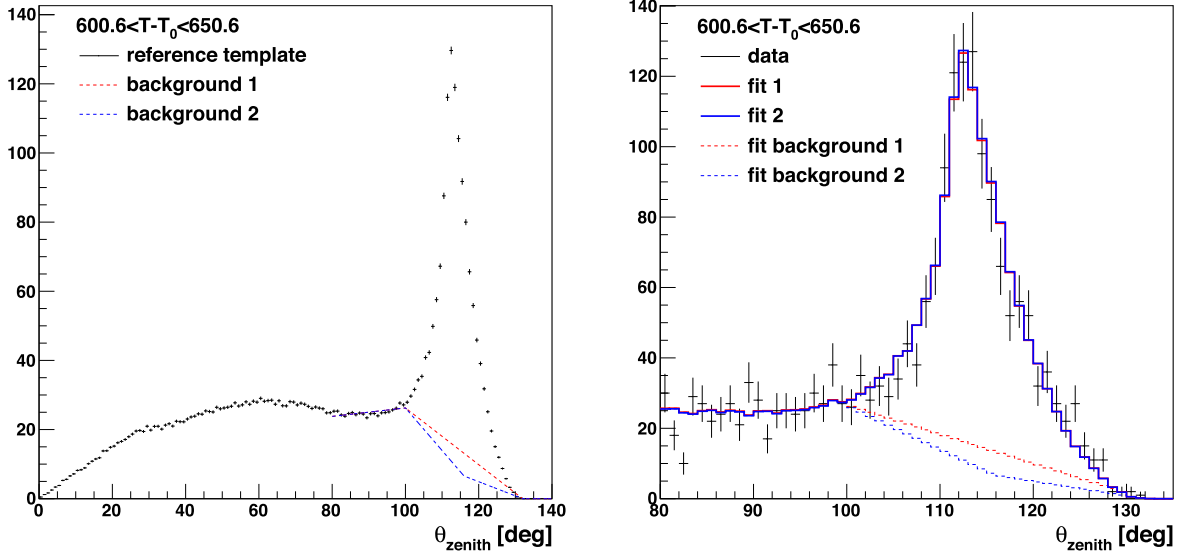


Figure 16. Left: reference θ_{zen} template for the time interval $[600.6, 650.6]$. The Earth-limb peak is centered at about 113° . The red and blue dashed curves correspond to the background template for the two background hypotheses, $b_{116} = b_{100}/2$ (background 1) and $b_{100}/4$ (background 2), respectively. Right: θ_{zen} distributions for the $[600.6, 650.6]$ time interval (black). The solid red and blue curves (barely distinguishable) correspond to the signal+background distribution predicted by the fits for the two background hypotheses, while the dashed red and blue curves show the corresponding background contributions.

of $f_s + \delta f_s$ of the two background hypotheses to define a 68% confidence interval, from which we derive the combined relative efficiency and its uncertainty.

To verify the method, we compute the relative efficiency for 50 s time intervals using several 900 s subsets of the reference data set. For each subset, we do not use the subset to build the reference template, and the times are computed with respect to T_{ref} , the time for which the satellite is at the same position/orientation as at the time of the GRB trigger. The results are shown in Figure 17 (left). The uncertainties, not shown in the figure for the sake of clarity, are of the order of 0.05. The average efficiencies of the subsets vary between 0.93 and 1.05, and the reduced χ^2 of a fit by a constant is ~ 1 , which proves that, when taking into account the average shift of each subset, the uncertainty on the relative efficiency is correctly estimated.

The relative efficiency for 50 s time intervals from 100–1000 s after the GBM trigger, except during the BTI, is shown in Figure 17 (right). A fit by a constant gives an average of 0.97 and a reduced χ^2 of 1.

The results of the fit of the θ_{zen} distributions for the time intervals $[225.6 \text{ s}, 235.6 \text{ s}]$ and $[245.6 \text{ s}, 255.6 \text{ s}]$, roughly corresponding to P1 and IP, are shown in Figure 18. The Earth-limb peak is clearly visible for IP but not for P1, which is consistent with the derived relative efficiencies: 0.13 ± 0.12 , 0.92 ± 0.10 for P1 and IP, respectively. We also note that the two θ_{zen} distributions both peak at about 40° , which corresponds to events coming from the GRB direction.

To derive the GRB light curve, we apply the same method to 5 s time intervals between 200 s and 300 s. The results are shown in Figure 19 (left), for three $\log_{10} E_{\text{tkr}}$ thresholds. These results allow

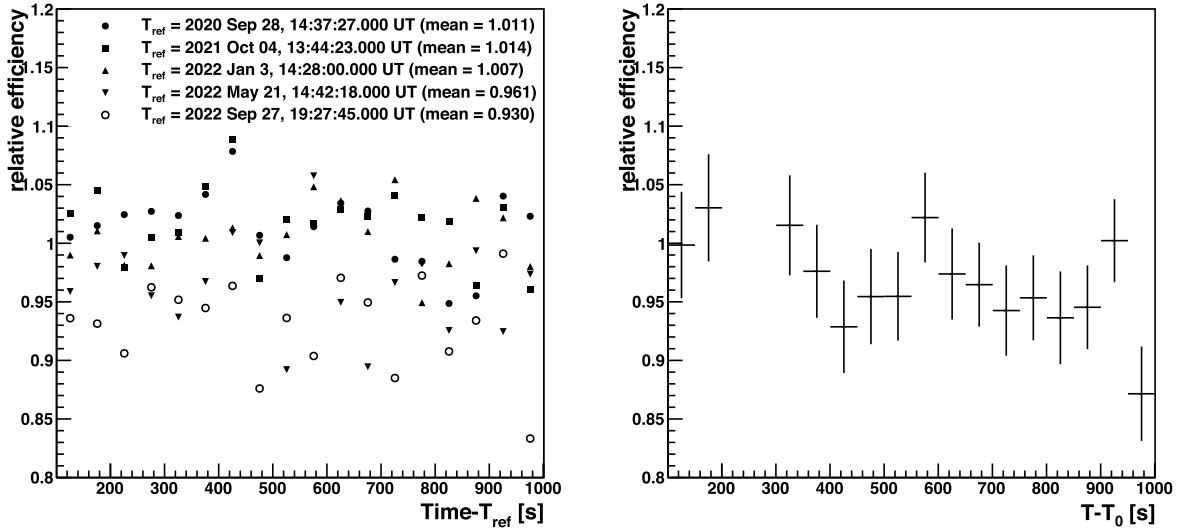


Figure 17. Left: relative efficiency in 50 s bins for five data subsets from 100–1000 s after T_{ref} , the time when the satellite is at the same position/orientation as at the time of the GRB trigger. All points have a $\sim 5\%$ uncertainty, which is not displayed for clarity's sake. The mean relative efficiency of each subset is indicated between parentheses. Right: relative efficiency in 50 s bins from $T_0 + 100$ to $T_0 + 1000$ s, except for the two bins corresponding to the BTI.

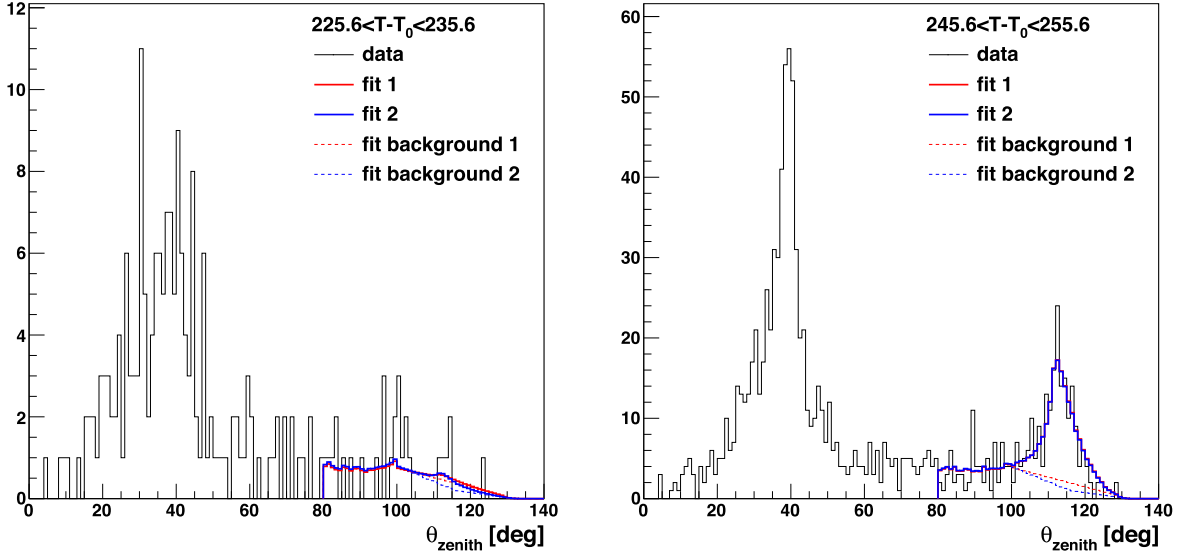


Figure 18. Left: θ_{zenith} distribution for the $[225.6 \text{ s}, 235.6 \text{ s}]$ time interval. Right: same for the $[245.6 \text{ s}, 255.6 \text{ s}]$ time interval. The solid red and blue curves correspond to the signal+background distribution predicted by the fits for the two background hypotheses, whereas the dashed red and blue curves show the corresponding background contributions. The Earth-limb peak at about 113° is clearly visible in the $[245.6 \text{ s}, 255.6 \text{ s}]$ time interval, whereas it seems absent in the $[225.6 \text{ s}, 235.6 \text{ s}]$ time interval.

us to characterize the relative efficiency variation with time (especially the efficiency drop during P1), but the derived efficiencies are not very precise. Furthermore, they change significantly when increasing the energy threshold, which is not the case for the 50 s time intervals, as demonstrated by Figure 19 (right). Another issue is that the efficiency during P1 is compatible with 0. Since there seems to be a GRB signal during P1, as suggested by the peak at approximately 40° zenith angle in Figure 18 (left), an efficiency compatible with 0 would not allow us to derive an upper limit of the GRB flux. To overcome this limitation, we develop an alternative method presented in the following Appendix section.

A.2. GRB Flux Measurement during the BTI

Measuring the GRB flux during the BTI requires an event selection and the estimation of its effective area. In the case of

fast transient signals like GRBs, good sensitivity can be achieved with a minimal event selection. For the prompt emission of GRB 221009A, using a minimal event selection is actually recommended because it helps us to mitigate the systematics produced by the extra noise induced by the GRB LE emission. We choose the simplest event selection: Engine 7 events passing the gamma filter, with at least one track and above a given E_{thr} threshold, which will be defined later.

As we previously explained, it is not possible to precisely estimate the event selection effective area with LAT data only. The only possibility is thus to use realistic simulations of individual HE photons on top of a background of LE photons. In order to do so, we need to know the GRB LE spectrum. This information is not provided by the GBM results due to the pulse pileup effect during P1 and P2 (S. Lesage et al. 2023). Here, we first describe how we constrain the GRB LE flux, and we derive the event selection effective area as a function of

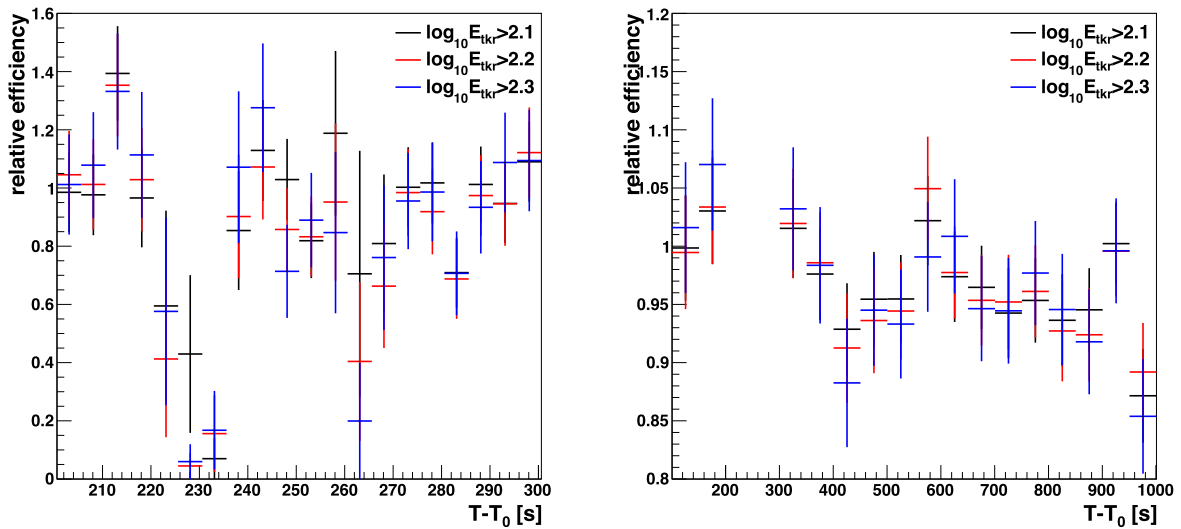


Figure 19. Left: relative efficiencies in 5 s bins from $T_0 + 200$ to $T_0 + 300$ s for three energy thresholds. The efficiencies decrease significantly during P1 and P2. Right: same for 50 s bins from $T_0 + 100$ to $T_0 + 1000$ s.

time during the BTI. We then present the GRB light-curve analysis.

A.2.1. Characterization of the Extra Noise in the Instrument

The photon absorption cross section strongly decreases with energy until it reaches a minimum at about 3 MeV, above which it is almost constant. So, the interaction of the GRB LE photons occurs very soon after the photons enter the LAT, while the interaction of HE photons occurs deeper in the instrument. Since the GRB is very far off-axis during the BTI ($\sim 74^\circ$ with respect to boresight), and its direction is close to the y -axis, as shown in Figure 20, the most exposed part of the tracker is the top planes of the $-Y$ -face towers. That is the reason why we use the information of the two top planes of the two central towers of the $-Y$ face of the LAT to monitor the extra noise level. We refer to this part of the tracker as the tracker corner. These two towers are highlighted in red in Figure 20.

We compute two quantities: N_{occ} , the corner occupancy (the average of the fractions of events with at least one fired strip in the corner planes), and N_{mns} , the corner mean number of fired strips. Figure 21 shows their variation, which makes apparent the features already seen in Figure 13, namely P1, IP, and P2. We note that, for individual HE photons, the expected levels of the corner occupancy and the mean number of fired strips are about 1% and 0.1, which is much lower than the levels reached during P1 and P2.

The average number of fired strips in the whole tracker could help us to characterize the extra noise, but it is likely biased by the signal induced by HE photons. To avoid this bias, we estimate the pedestal, that is to say the bottom edge, of this quantity, for any given time interval. To do so, we compute $N_{1\%}$ and $N_{20\%}$, the 1% and 20% quantiles of the distribution of the total number of fired strips, and define $N_{\text{ped}} = (N_{1\%} + N_{20\%})/2$ and its uncertainty $(N_{20\%} - N_{1\%})/2$. The P1, IP, and P2 features are also clearly apparent in the variation of N_{ped} , as can be seen in Figure 21.

Figure 22 shows the same information as in Figure 21, but with a y -axis range set to show the baselines of N_{occ} , N_{mns} , and N_{ped} .

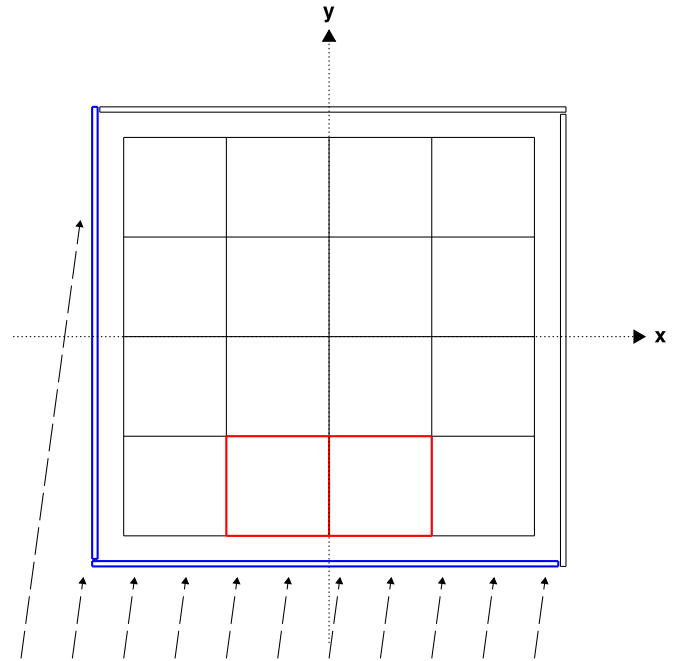


Figure 20. Top view of the LAT. The 4×4 square matrix corresponds to the 4×4 tracker towers. The two towers used to measure the corner occupancy and mean number of strips are highlighted in red. The two ACD $-X$ and $-Y$ bottom tiles are highlighted in blue. The dashed arrows illustrate the GRB photon direction, showing that the GRB photons first arrive at the $-Y$ face of the LAT.

The ACD information is less straightforward to use because its key role in the trigger and the onboard gamma-ray filter can very easily create a bias. We mitigate this problem by only using the information from the bottom tile of the $-X$ face and the bottom tile of the $-Y$ face. The four ACD bottom tiles (1.7 m long and 15 cm high, whose top parts cover the two bottom planes of the tracker) do not participate in the trigger decision and are not part of the most sensitive test of the gamma-ray filter. We use the $-X$ and $-Y$ bottom tiles and not the $+X$ and $+Y$ because the former face the GRB direction, and their signals are thus not biased by the GRB HE emission. As in the

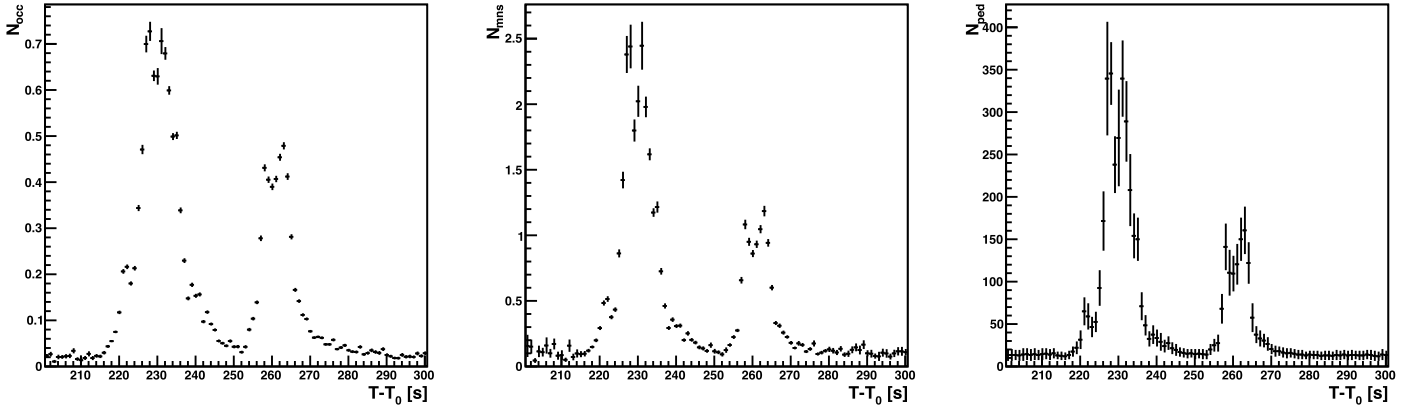


Figure 21. The time variation of the tracker-based quantities used to monitor the noise induced by the GRB LE emission. Left: the corner occupancy. Center: the corner mean number of strips. Right: the total number of strips pedestal. All quantities show the P1/IP/P2 structure.

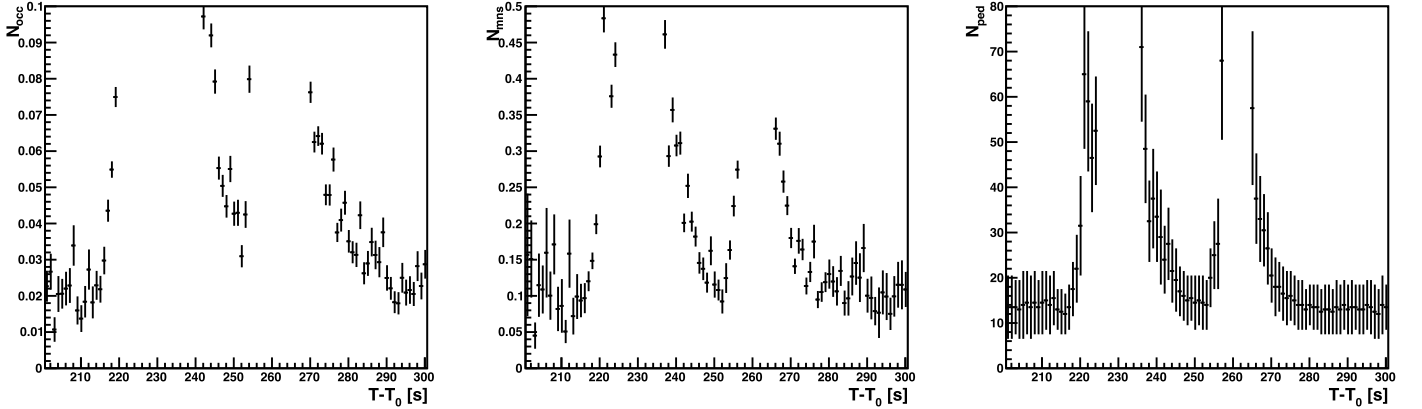


Figure 22. Same as in Figure 21 but with the y-axis ranges set to show the baseline levels.

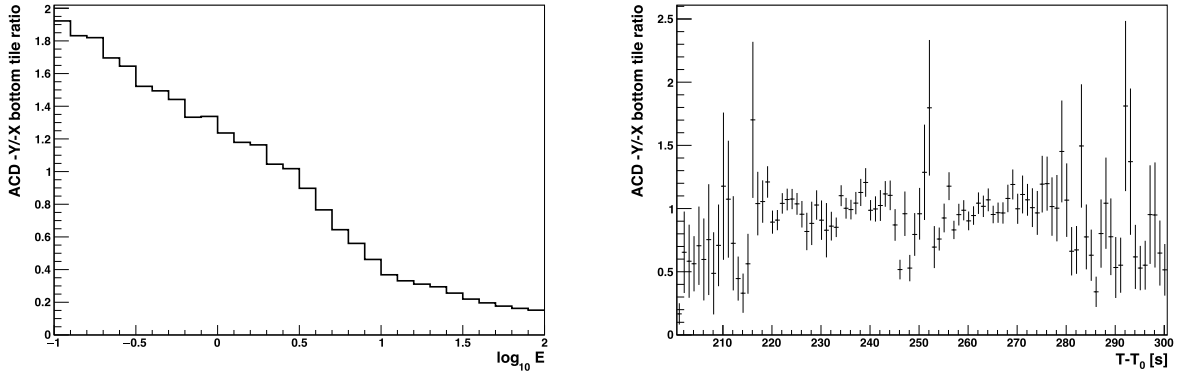


Figure 23. Ratio of the ACD $-Y/-X$ bottom tile signals. Left: dependence with energy in MeV derived from simulations. Right: observed time variation during the BTI. Because the ratio varies with energy, it is sensitive to a spectral change. The fact that it is almost constant during the BTI, especially during P1 and P2, shows that the GRB LE spectrum did not change much during the BTI.

tracker, the interaction of LE photons in the ACD depends on their energy. Using dedicated simulations, we find that the ratio of the signals in the $-Y$ and $-X$ bottom tiles is sensitive to the photon energy, as shown in Figure 23 (left). So, this ratio is sensitive to the GRB LE spectrum. Figure 23 (right) shows that this ratio does not vary much during the BTI, especially during P1 and P2. As a consequence, we assume that the shape of the GRB LE spectrum did not change significantly during the BTI.

This assumption allows us to use the tracker 1 s information during the BTI all together in order to constrain the LE spectrum. This is done by looking at the correlation of N_{occ} with N_{mns} and the correlation of N_{ped} with N_{mns} . These

correlations, shown in Figure 24, are both relatively tight, strengthening the assumption of a constant shape of the LE spectrum. As expected, the N_{occ} correlation exhibits an inflection, while the N_{ped} correlation is linear.

We model the GRB LE emission with a Band function (D. Band et al. 1993). It corresponds to two smoothly connected power laws and, in addition to its normalization, it is defined by E_p , the SED peak energy, and α and β , the spectral indices below and above E_p , respectively. For each set of parameters (E_p , α , β), we perform multiphoton simulations, with photons between 0.1 and 30 MeV coming from the GRB direction, randomly distributed over a 2.8 m^2 surface, large

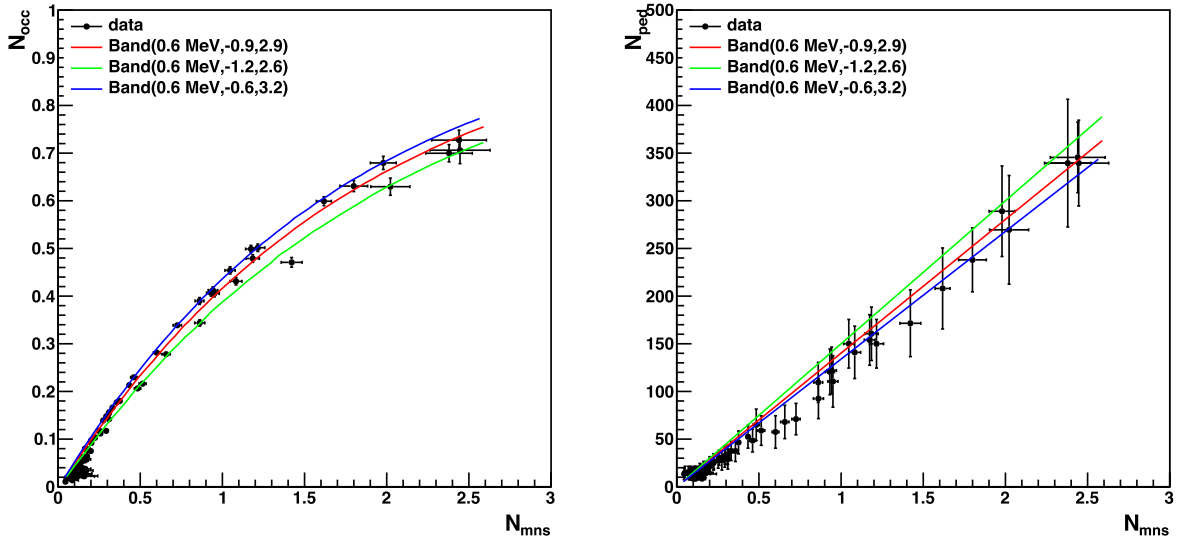


Figure 24. Correlations of the tracker-based quantities used to monitor the noise induced by the GRB LE emission. Left: corner occupancy vs. corner mean number of strips. Right: total number of strips pedestal vs. corner mean number of strips. The black dots correspond to the 1 s intervals in [200.6 s, 300.6 s]. The red, green, and blue curves correspond to simulations produced with Band models with $E_p = 0.6$ MeV.

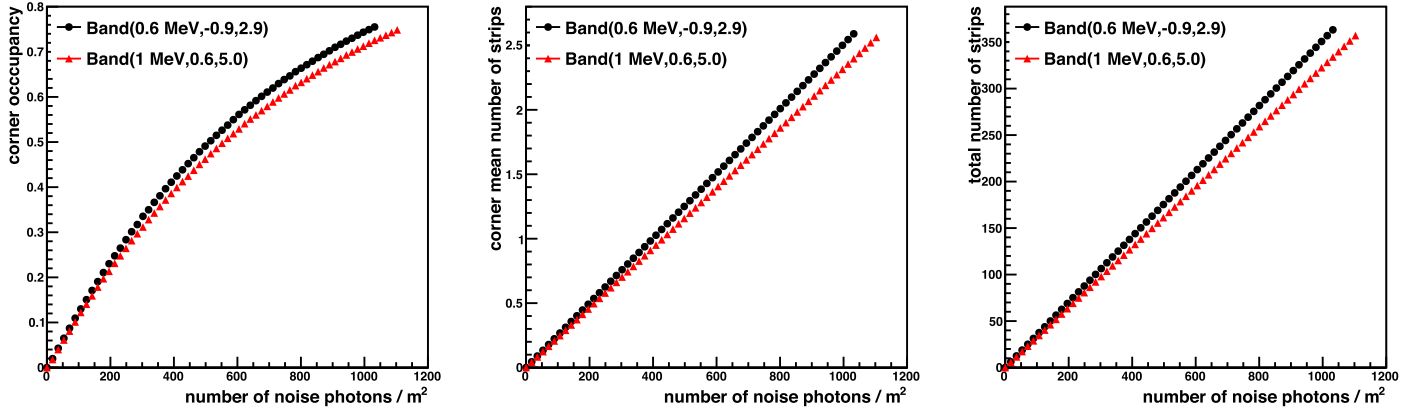


Figure 25. Tracker-based quantities as a function of the LE noise flux, as predicted with simulations. Left: the corner occupancy. Center: the corner mean number of strips. Right: the total number of strips. The black points correspond to $(E_p, \alpha, \beta) = (0.6 \text{ MeV}, -0.9, 2.9)$, and the red points correspond to $(1 \text{ MeV}, 0.6, 5.0)$. For a given LE spectrum hypothesis, these graphs can be used to estimate the LE noise flux (x-axis) from a measured quantity (y-axis).

enough to cover the entire LAT sensitive detectors. We can then predict N_{occ} , N_{mns} , and N_{ped} as a function of the incoming LE flux, as shown in Figure 25 for $(E_p, \alpha, \beta) = (0.6 \text{ MeV}, -0.9, 2.9)$ and $(1 \text{ MeV}, 0.6, 5.0)$. These results are then used to predict the same correlations as measured in the data.

For a given value of E_p , we can perform a fit to the data to find the optimal values of (α, β) . The fit for $E_p = 0.6$ MeV gives $(\alpha, \beta) \sim (-0.9, 2.9)$, providing a good data/prediction agreement as can be seen in Figure 24. One can also see that α and β have to be changed by 0.3 to clearly see a deviation from the data.

We find a good data/prediction agreement for $0.4 \text{ MeV} \lesssim E_p \lesssim 1 \text{ MeV}$, with the following trend: β decreases when E_p decreases. As will be shown in Section A.2.4, the HE power-law index during P1 and P2 is found to be $\gtrsim 3$. This constrains β to also be $\gtrsim 3$, which is reached for $E_p \sim 0.6$ MeV. The interval for E_p thus shrinks to $[0.6, 1 \text{ MeV}]$. The fit for $E_p = 1.0$ MeV leads to $(\alpha, \beta) \sim (0.6, 5.0)$, which also provides a good data/prediction agreement, as shown in Figure 26.

In order to assess the impact of the GRB LE flux, in the following appendix sections we will use two hypotheses for the

LE spectrum: $B_{0.6} = \text{Band}(0.6 \text{ MeV}, -0.9, 2.9)$ and $B_{1.0} = \text{Band}(1 \text{ MeV}, 0.6, 5.0)$.

A.2.2. Event Selection Effective Area

The event selection requires that a photon triggers the instrument, passes the gamma-ray filter, that at least one track is reconstructed, and that the reconstructed energy is above a given threshold. The corresponding effective area is estimated thanks to simulations of individual photons in the LAT.

Trigger engine 7 requires that the incoming photon triggers at least one tracker tower without vetoing any of the surrounding ACD tiles. Almost all photons below ~ 1 GeV do not have more than 100 MeV in one calorimeter crystal and are thus rejected at the gamma-ray filter level by any vetoing ACD tile, which is a more stringent requirement than the Engine 7 ACD veto requirement. As a consequence, we can divide the selection into the following three steps:

1. the tracker tower trigger;
2. the ACD veto by any tile above threshold;

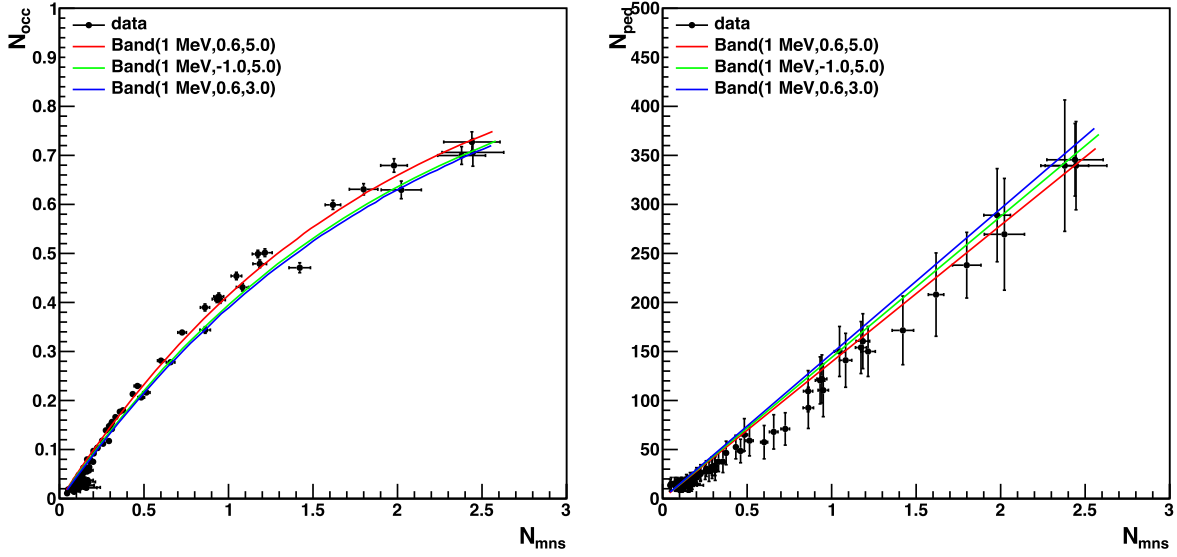


Figure 26. Same as Figure 24, except that the red, green, and blue curves correspond to simulations produced with Band models with $E_p = 1$ MeV.

- the track and energy requirements based on information provided by the event reconstruction.

The GRB LE flux impacts the event selection, and we need to estimate the resulting correction factor, that is to say the ratio of the effective area in the presence of LE photon background with respect to the effective area without background. This correction factor depends on time (because of the time variation of the LE background flux), and we can factorize it into three parts:

$$C_{\text{sel}}(t) = C_{\text{trig}}(t) \times C_{\text{veto}}(t) \times C_{\text{rec}}(t) \quad (\text{A1})$$

where C_{trig} , C_{veto} , and C_{rec} account for the three steps of the event selection. Since the LE background only adds activity in the instrument, it cannot prevent an HE photon from triggering a tracker tower, from which we conclude that $C_{\text{trig}} = 1$ and that it can be ignored when estimating C_{sel} . However, this trigger factor must be taken into account when estimating the false-positive rate, as will be discussed in Section A.2.3.

In the standard simulation of an individual photon in the LAT (like the one produced for the LLE analysis), all of the energy deposits in the various parts of the instrument are assumed to occur at the same time. The situation is more complex when simulating one individual photon on top of a background of many photons because the background photons are not in time with the signal photon. As a consequence, a realistic simulation has to take into account the characteristic readout times of the various detectors. For the tracker, the width of the trigger coincidence window is ~ 700 ns, while the average time over the threshold of the shaped signal is $\tau_{\text{tkr}} \sim 10$ μs . For the ACD, our analysis depends only on the trigger fast signal, whose shaping time is $\tau_{\text{ACD}} \sim 0.4$ μs . Rather than modifying the standard simulation to take into account these various characteristic times, we make use of the factorization of the effective area correction. Each part can be studied with a simulation performed with the number of LE photons that corresponds to the relevant characteristic time: τ_{ACD} for C_{veto} and τ_{tkr} for C_{rec} .

For a given time interval, the background LE flux is estimated using the tracker corner occupancy. Assuming a certain LE spectrum (either $B_{0.6}$ or $B_{1.0}$), we use the

information of Figure 25 (left) to derive n_{tkr} , the number of LE photons per m^2 in the simulation needed to reproduce the observed noise. Since the corner occupancy is based on the information of the fired strips recorded in the tracker, n_{tkr} actually corresponds to the time window τ_{tkr} . It means that we use a simulation with n_{tkr} LE photons to assess C_{rec} . To assess C_{veto} for the same LE flux level, we use a simulation with a number of LE photons set to $n_{\text{ACD}} = r_{\tau} n_{\text{tkr}}$, where $r_{\tau} = \tau_{\text{ACD}}/\tau_{\text{tkr}}$, the ratio between the characteristic times of the ACD fast signal and the tracker readout signal, which is expected to be ~ 0.04 .

Because of the importance of r_{τ} in the estimation of C_{veto} , we want to constrain it with the help of the Earth-limb relative efficiency presented in Section A.1.2. This requires that we compute C_{veto} and C_{rec} both for HE photons coming from the GRB direction and for HE photons coming from the Earth-limb direction, which corresponds more or less to the mirror opposite of the GRB direction with respect to the plane $y = 0$.

When estimating C_{rec} , we are only interested in the effect of the LE background on the tracker reconstruction capability. Therefore, we perform simulations in which we ignore the energy deposited by the background LE photons in the ACD. C_{rec} is given by the ratio of the selection efficiency with background compared to the efficiency without background. The selection threshold E_{tkr} is set to 100 MeV for the GRB direction, but we use 125 MeV for the Earth-limb direction in order to match the threshold used in Section A.1.2. We find that C_{rec} does not vary significantly with energy for HE photons between 100 MeV and 1 GeV. The variations of C_{rec} with n_{tkr} are shown in Figure 27. One can see that the GRB LE background impacts differently the HE photons of the GRB and Earth limb: the loss of efficiency at large n_{tkr} is greater for the former.

We also use simulations to estimate C_{veto} as a function of n_{ACD} , the number of LE photons per m^2 within τ_{ACD} . But in that case, the energy deposited by the background LE photons in the ACD is not ignored. As for C_{rec} , we do not see any significant dependence on the HE photon energy. We also do not see any significant difference between the GRB and Earth-limb directions, as can be seen in Figure 28.

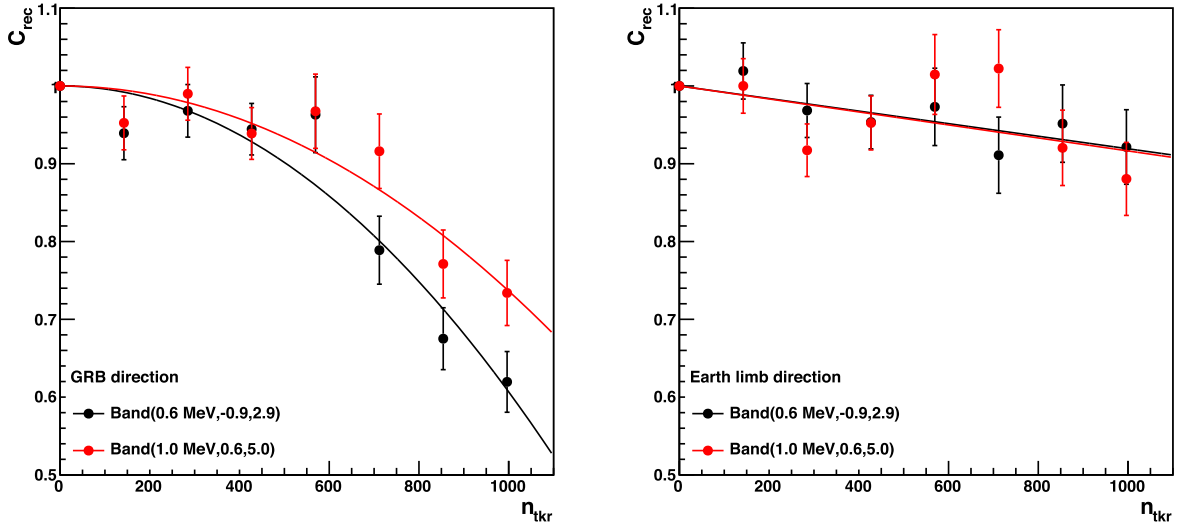


Figure 27. The effective area correction factor C_{rec} corresponding to the final part of the event selection (at least one track and above a given energy threshold) as a function of n_{tkr} , the number of LE photons per m^2 within τ_{tkr} , the tracker characteristic readout time. Left: for HE photons coming from the GRB direction and with $E_{\text{tkr}} > 100$ MeV. Right: for HE photons coming from the Earth-limb direction and with $E_{\text{tkr}} > 125$ MeV. For both cases, the black and red points correspond to $B_{0.6}$ and $B_{1.0}$, respectively.

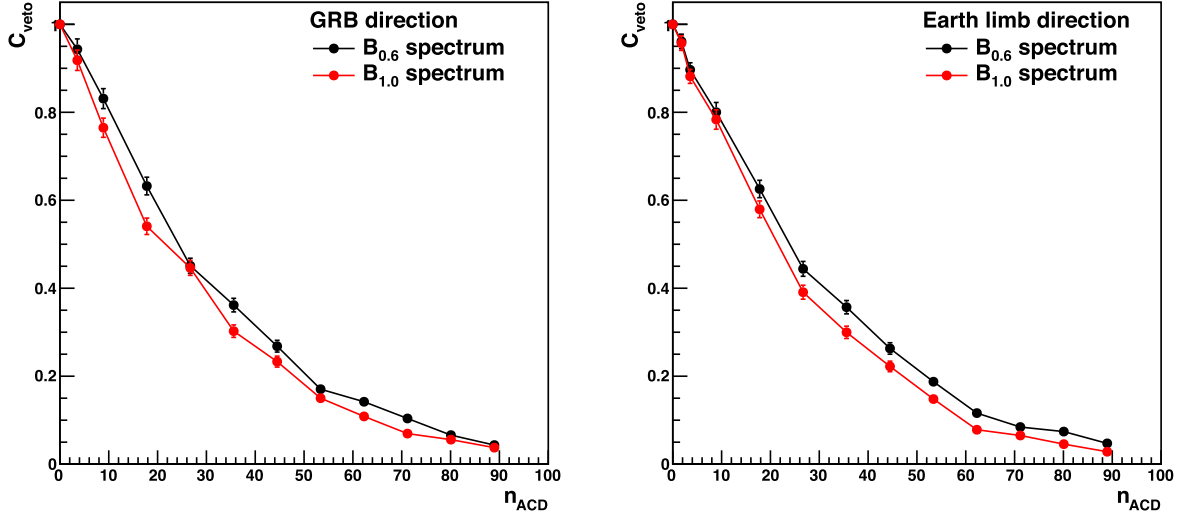


Figure 28. The effective area correction factor C_{veto} corresponding to the ACD veto part of the event selection as a function of n_{ACD} , the number of LE photons per m^2 within τ_{ACD} , the ACD fast signal characteristic time. Left: for HE photons coming from the GRB direction and with $E_{\text{tkr}} > 100$ MeV. Right: for HE photons coming from the Earth-limb direction and with $E_{\text{tkr}} > 125$ MeV. For both cases, the black and red points correspond to $B_{0.6}$ and $B_{1.0}$, respectively.

For each hypothesis of the LE spectrum, we can estimate n_{tkr} as a function of time from the corner occupancy shown in Figure 21. In normal conditions, the corner occupancy is about 0.02, and we consider that no selection correction is needed when the corner occupancy is < 0.035 . n_{tkr} allows us to know $C_{\text{rec}}(n_{\text{tkr}})$. We then use r_τ to compute $C_{\text{veto}}(r_\tau n_{\text{tkr}})$ and eventually obtain the selection correction factor as a function of time:

$$C_{\text{sel}}(t) = C_{\text{veto}}(r_\tau n_{\text{tkr}}(t)) \times C_{\text{rec}}(n_{\text{tkr}}(t)). \quad (\text{A2})$$

We constrain r_τ using the information of the Earth-limb relative efficiency. For each LE spectrum hypothesis, we perform a χ^2 fit to find the value of r_τ that provides the best prediction of the relative efficiency in nine time intervals chosen such that the noise variation is minimal within each of these intervals. For each time interval, we estimate n_{tkr} from the corner occupancy, and the predicted efficiency can be computed for any r_τ using Equation (A2). We find

$r_\tau \pm dr_\tau = 0.062 \pm 0.013$ for the $B_{0.6}$ spectrum and $r_\tau \pm dr_\tau = 0.050 \pm 0.012$ for the $B_{1.0}$ spectrum. The data/prediction agreement is good, with a $\chi^2 = 8.6$, as shown in Figure 29. One can see that the predicted efficiencies of the two LE spectrum hypotheses are almost identical. We note that the estimated r_τ values are not far from the expected value of 0.04.

For each LE spectrum hypothesis, we compute C_{sel} in three flavors: C_{cen} with r_τ , C_{min} with $r_\tau + dr_\tau$, and C_{max} with $r_\tau - dr_\tau$. We combine the results of the two LE spectrum hypotheses by taking the average of C_{cen} , as well as the minimum of C_{min} and the maximum of C_{max} . The resulting effective area correction during the BTI is shown in Figure 30.

A.2.3. False Positive

The previous appendix sections were devoted to the impact of the GRB LE flux on our ability to correctly detect HE photons. But the GRB LE flux alone can create a fake HE signal. In order to quantify the false-positive rate induced by

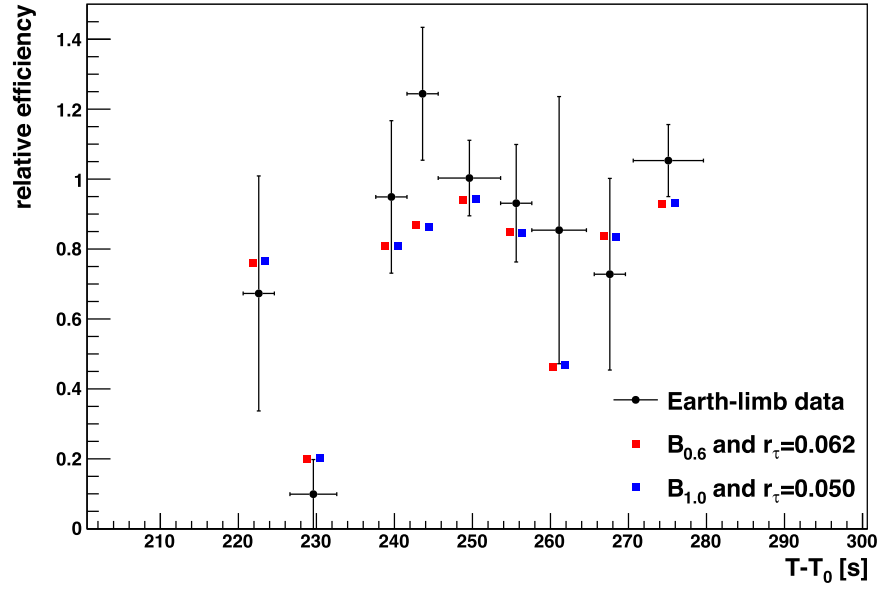


Figure 29. Result of the fit of the relative efficiency to constrain the time ratio r_τ . The black points correspond to the measurement obtained with Earth-limb data. The red points correspond to the relative efficiency predicted by the simulation with the $B_{0.6}$ spectrum and $r_\tau = 0.062$. The blue points correspond to the $B_{1.0}$ spectrum and $r_\tau = 0.050$. The red and blue points have been slightly shifted along the x-axis for clarity's sake.

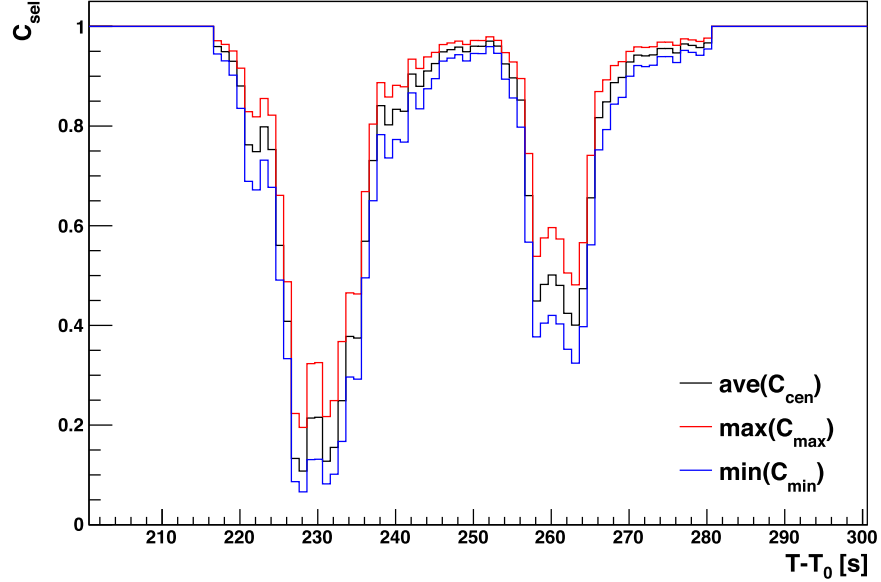


Figure 30. Effective area correction factor C_{rec} as a function of time during the BTI after combining the corrections of the $B_{0.6}$ and $B_{1.0}$ spectrum hypotheses. The black curve corresponds to the average of C_{cen} . The red and blue curves correspond to the maximum of C_{max} and to the minimum of C_{min} , respectively.

the GRB LE flux, we perform simulations with only background LE photons, between 0.1 and 30 MeV. In that situation, the background alone has to trigger a tracker tower, and we thus have to take into account τ_{trig} , the ~ 700 ns tracker trigger coincidence window, to estimate the rate of background events that trigger a tracker tower. As for the efficiency correction factor, we factorize the problem by assuming that the false-positive rate is

$$\rho = \frac{1}{\tau_{\text{trig}}} \times \epsilon_{\text{trig}} \times \epsilon_{\text{veto}} \times \epsilon_{\text{rec}}$$

where ϵ_{trig} is the fraction of events that trigger a tracker tower, ϵ_{veto} is the fraction of events with a tracker tower trigger that are not vetoed by the ACD, and ϵ_{rec} is the fraction of events for which a track is found and that pass the chosen energy

threshold. The $1/\tau_{\text{trig}}$ term approximates the number of independent time intervals during which the background can trigger a tracker tower.

For an LE background flux given by n_{trk} , we use simulations with $\tau_{\text{trig}}/\tau_{\text{tkr}} \times n_{\text{trk}}$ to estimate ϵ_{trig} . Regarding ϵ_{veto} , we can assume that it is equal to $C_{\text{veto}}(r_\tau n_{\text{trk}})$ because the tracker energy deposits and the ACD energy deposits are not correlated. ϵ_{rec} is derived from simulations with n_{trk} LE photons. We use two values for τ_{trig} , 700 ns and 1500 ns, and find no difference in false-positive rate.

As expected, the false-positive rate depends very much on β , the second spectral index of the LE spectrum. We actually find that for $\text{LE}_{1.0}$ with $\beta = 5.0$, it is always < 1 Hz. On the contrary, the $B_{0.6}$ spectrum with $\beta = 2.9$ predicts a significant false-positive rate, which can be considered as an upper limit.

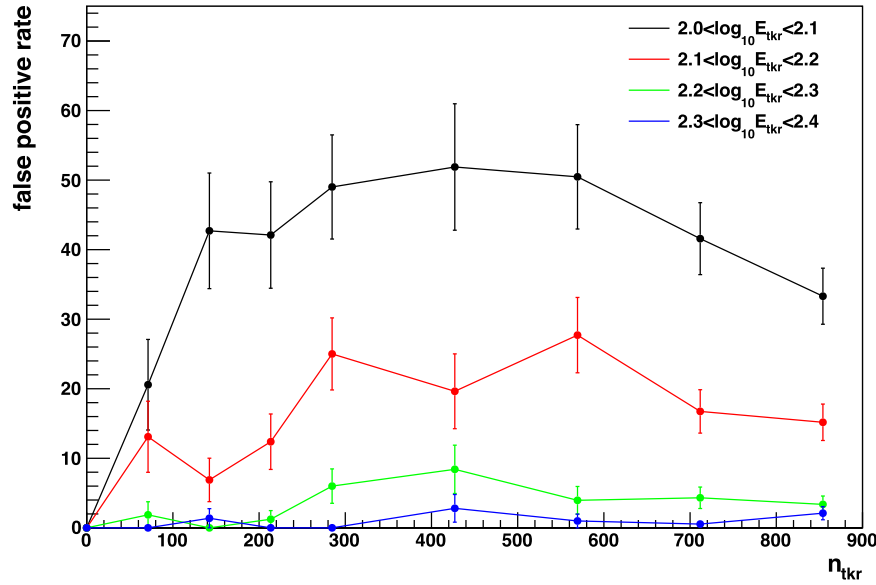


Figure 31. False-positive rate in Hz within 20° of the GRB for several $\log_{10} E_{\text{trk}}$ bins as a function of the number of LE photons per m^2 within $\sim 10 \mu\text{s}$, derived with the $B_{0.6}$ spectrum hypothesis.

Figure 31 breaks down the false-positive rate in $\log_{10} E_{\text{trk}}$ bins. One can see that it decreases very much with energy. As a consequence, we set the selection E_{trk} threshold to 160 MeV to ensure that the false-positive rate is < 10 Hz. We note that, as can be seen in Figure 15, a 160 MeV E_{trk} threshold corresponds to about a 100 MeV threshold in true energy.

A.2.4. BTI Light Curve

In order to determine the GRB HE energy flux for a given time interval, we perform a fit to the data with templates of the expected distribution of θ_{GRB} , the angular separation with respect to the GRB direction. We used two kinds of templates: one to model the GRB HE signal and the other to model the HE background induced by the gamma-ray sky (including the Galactic diffuse emission and the isotropic emission). The former is predicted by the LLE simulation, while the latter is estimated with data recorded between 0 and 180 s, that is to say before the GRB HE emission hits the LAT. The GRB HE emission is modeled with a power law with a spectral index Γ_{ph} . Since the LLE simulation was produced with a spectral index of -1 , it is weighted by $E^{\Gamma_{\text{ph}}+1}$ to predict the HE signal templates.

The fit is performed over 10 bins in $\log_{10} E_{\text{trk}}$ between 2.2 and 3.2. There are two parameters for the HE emission (normalization and Γ_{ph}) and one background scaling parameter per energy bin. The results of the fit for the time interval [245.6 s, 250.6 s] are displayed in Figure 32. For each time interval, we take into account the variation of the selection effective area during the BTI by computing the average C_{sel} . We use the uncertainty on C_{sel} to estimate the systematic uncertainty on the HE emission.

To estimate n_{fp} , the expected upper limit on the number of false-positive events, for each time interval, we multiply the live time by the false-positive rate of the first fit energy bin ($2.2 < \log_{10} E_{\text{trk}} < 2.3$). We then compare this number with n_{obs} , the number of observed events within 20° in the same energy bin. The correction factor that we use to account for the false-positive rate (by multiplying the normalization of the HE

signal) is therefore assumed to be in the interval $[1 - n_{\text{fp}}/n_{\text{obs}}, 1]$.

We compute the light curve of the GRB HE emission during the BTI in 5 s time intervals. We find a significant HE emission after 215.6 s. The energy flux as well as the spectral index are shown in Figure 33 and included in Table 3. The most striking result is that the HE emission exhibits a unique peak, occurring during IP, as discussed in Section 3.2. The spectrum during this peak is rather hard, with $\Gamma_{\text{ph}} = -1.63 \pm 0.09$, whereas the spectral index during P1 and P2 is ~ -3 . After $T_0 + 275.6$ s, the spectral index is about -2 . We note that the template fit results after $T_0 + 280.6$ s are compatible with the results obtained with the LLE+TRANSIENT_010 joint fit with ThreeML and reported in Table 3.

A.2.5. Conclusion

The GRB LE emission is so bright during a time interval of 64 s (BTI) that it is unfortunately not possible to perform a standard analysis of the LAT data. In this appendix section, we have presented all of the solutions and methods that we needed to develop in order to be able to analyze the LAT data and to eventually characterize the GRB HE emission during this BTI. Here is a summary of the main items:

1. we replace the standard reconstructed energy with a new energy estimator, E_{trk} , based on the number of fired strips in a cone along the track axis;
2. we use Earth-limb data to constrain the selection efficiency;
3. we use the information in the top corner of the tracker and the information in the bottom ACD tiles to constrain the LE spectrum and precisely define the boundaries of the BTI;
4. we perform simulations of individual HE photons on top of a background of LE photons to estimate the selection effective area as a function of time, as well as the false-positive rate due to the LE background;
5. we apply a template fit approach to derive the HE emission light curve.

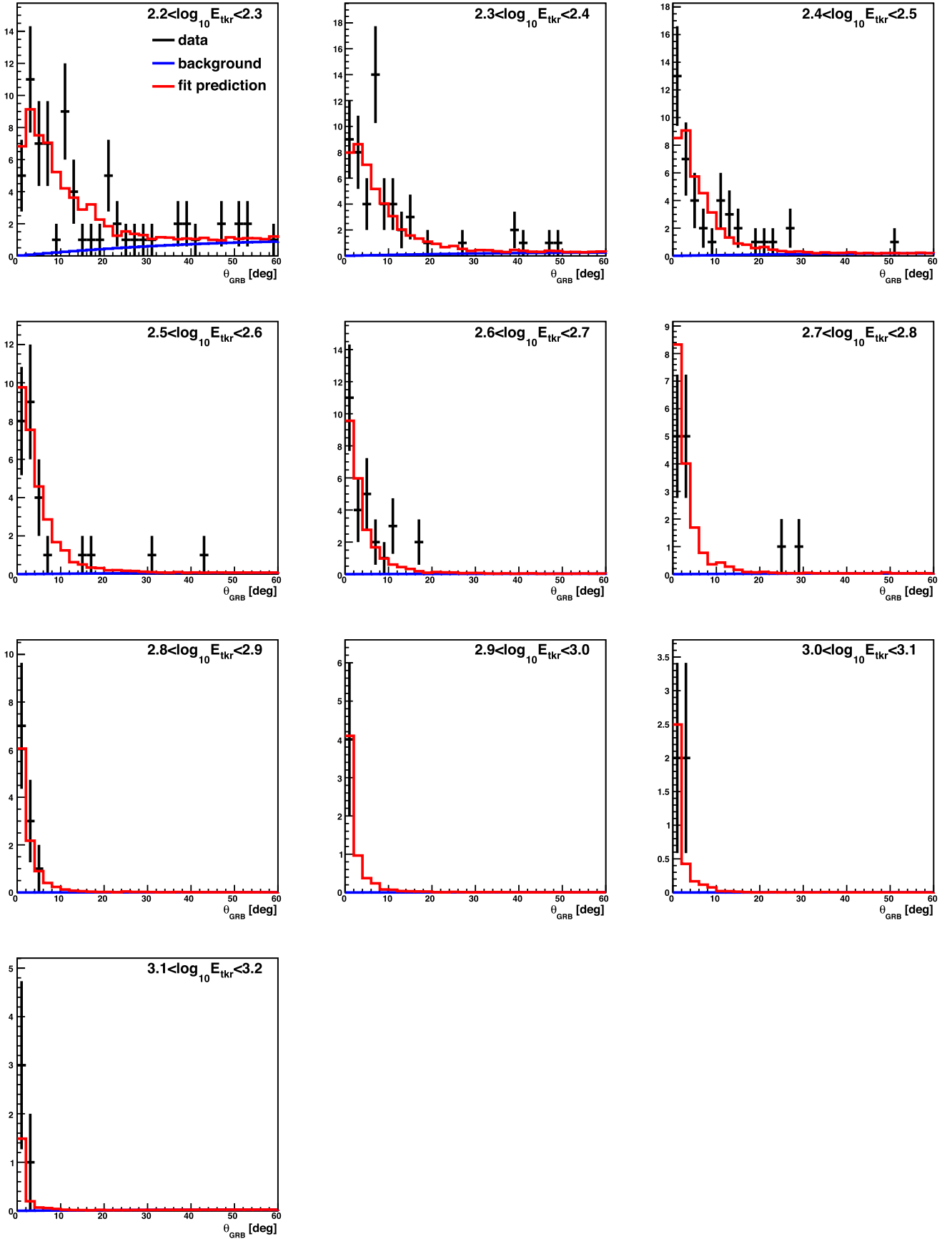


Figure 32. Distribution of θ_{GRB} , the angular separation to the GRB direction for the time interval [245.6 s, 250.6 s]. The black points correspond to the data, while the blue (background) and the red (background + GRB signal) histograms correspond to the result of the template fit.

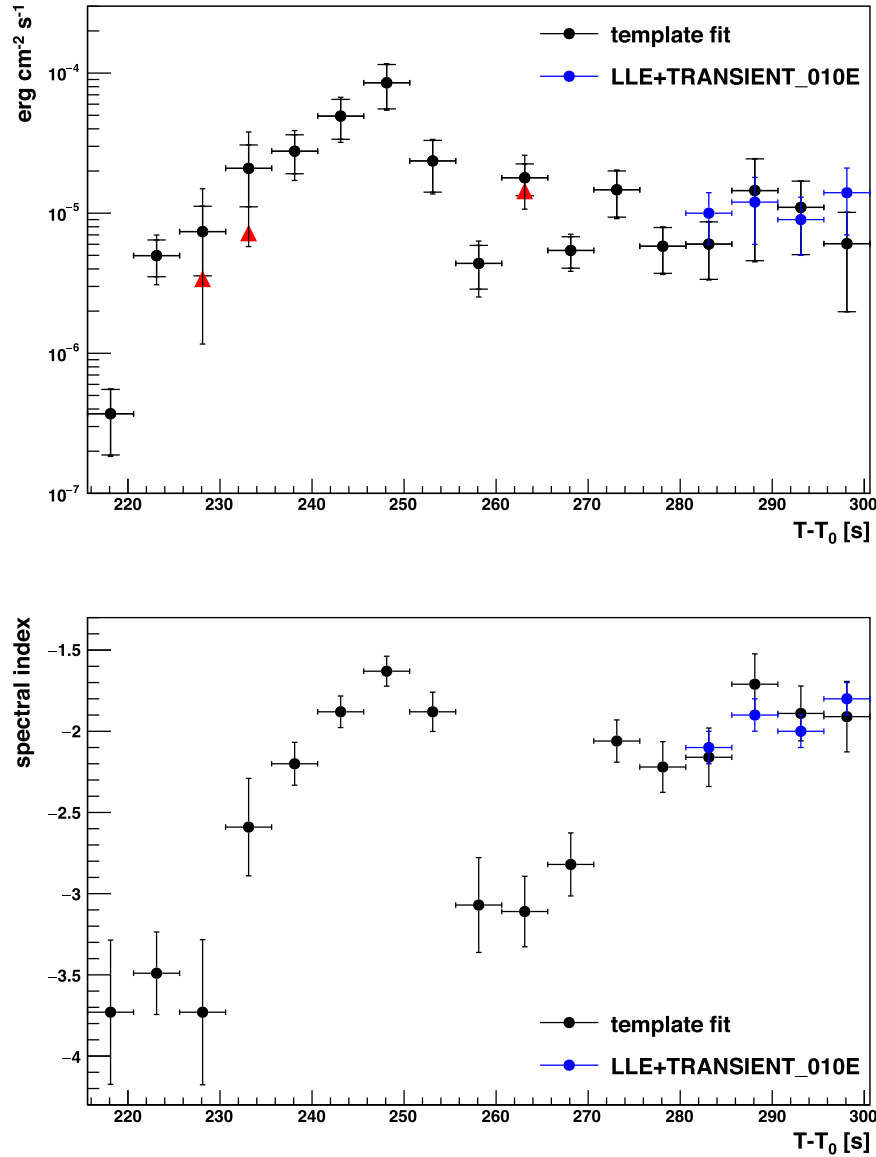


Figure 33. Light curve of the GRB HE emission during the BTL. Top: energy flux between 100 MeV and 10 GeV. The inner and outer error bars correspond to the statistical uncertainty and to the sum of the statistical and systematic uncertainties, respectively. The red triangles show the energy flux after subtraction of the contribution of the false-positive maximum rate. For clarity's sake, the red triangles are only shown when the induced difference is greater than half the statistical uncertainty. Bottom: spectral index of the HE power-law spectrum. The blue points correspond to the results of the LLE+TRANSIENT_010E joint fit with *ThreeML* reported in Table 3.

Appendix B

Time-resolved Joint Analysis between GBM and LAT Data

In Section 3 we presented the results of the time-resolved spectral analysis of the GBM and LAT data to analyze the triggering pulse (Section 3.1) and the prompt emission (Section 3.2). Here we provide some more details about the analysis, clarifying some technical aspects related to the joint spectral analysis. All of the models used in this paper are available in the *astromodels* package of *ThreeML*, and we refer to its documentation for their specific implementation. We performed a time-resolved spectral fit of the triggering pulse in five time intervals, using the CPL model (Cutoff_power-law_Ep model in *astromodels*). Figure 34 shows the count spectra and residual for the first two time intervals, which displayed the highest value of E_{peak} .

For the prompt phase, a time-resolved spectral fit was performed in seven time intervals, using Bayesian analysis available in *ThreeML*, selecting *multinest* as the sampler. We compared the models using the Bayesian evidence estimator ($\log Z$). In Table 8 we summarize the priors defined in the analysis.

Numerical values of the parameters of the best-fit model (SBPL+G+SBPL and SBPL+SBPL in the last interval) are in Table 9. In order to compare the residuals of the time-resolved spectral analysis, we show count spectra and residuals for all of the time intervals, to show the progression from top to bottom of SBPL, SBPL+SBPL, and SBPL+G+SBPL models in Figures 35–38. Note that the LHASO-WCDA spectrum is not displayed in the plots, but it is included in the fits.

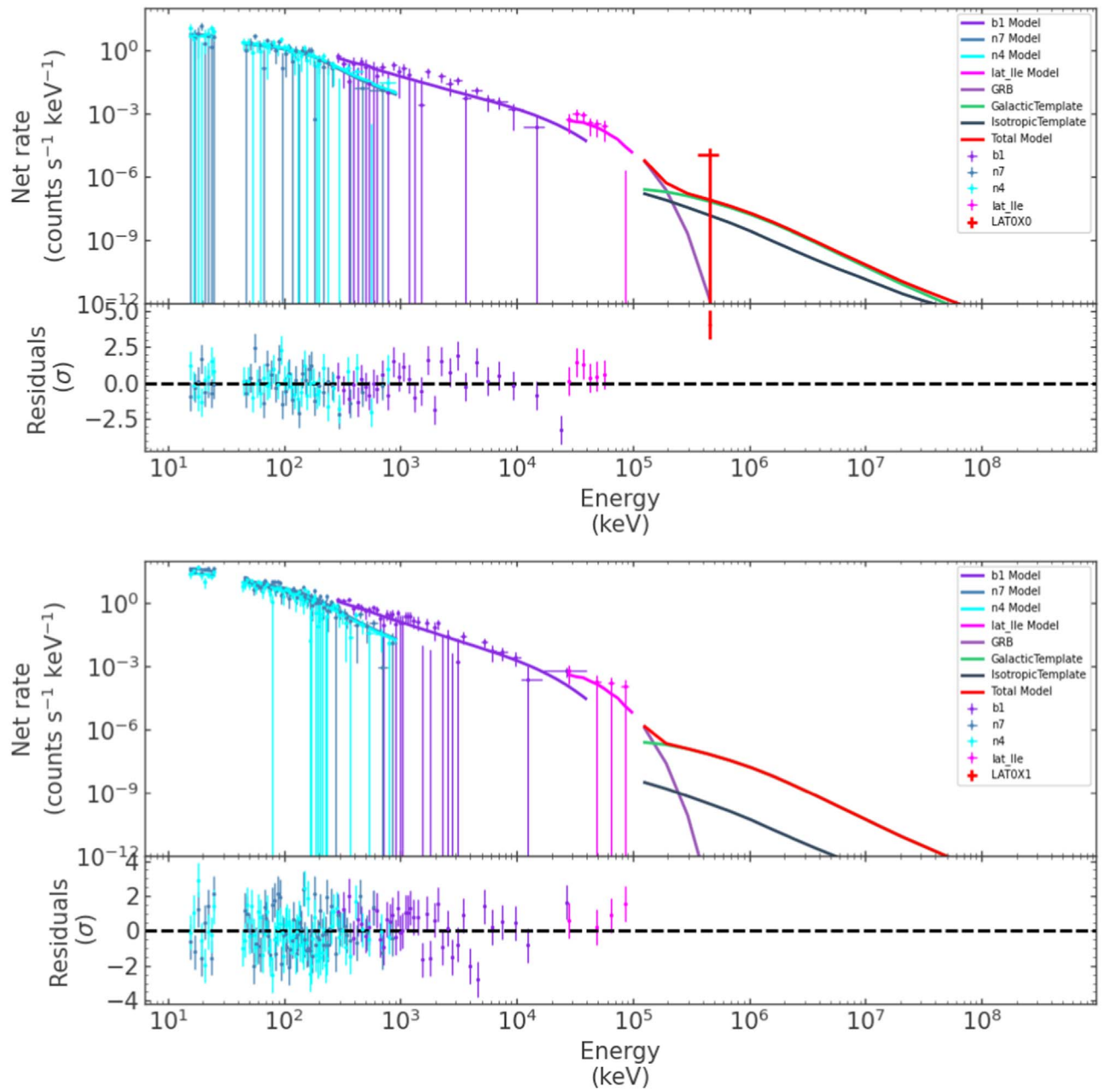


Figure 34. Count spectra (in counts $s^{-1} \text{ keV}^{-1}$) and residuals (in sigma units) for the CPL model for the $[T_0 - 0.69, T_0 + 0.23]$ (top) and $[T_0 + 0.23, T_0 + 1.0]$ (bottom) time intervals.

Table 8
Priors Used in the Bayesian Fit of GBM and LAT Data

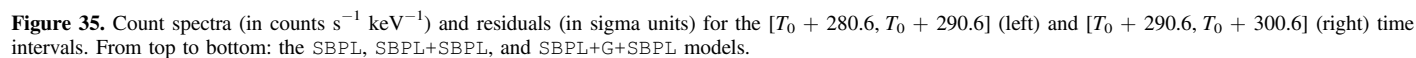
Function	Parameter	Prior	Bounds
SBPL	K_1	Log uniform	$(10^{-6}-10^6) [\text{cm}^{-2} \text{keV}^{-1} \text{s}^{-1}]$
	α_1	Uniform	$(-2, 2)$
	$E_{b,1}$	Log uniform	$(1 \text{ keV}-10 \text{ GeV})$
	β_1	Uniform	$(-10, 1)$
G	F	Log uniform	$(10^{-6}-10^6) [\text{cm}^{-2} \text{s}^{-1}]$
	μ	Uniform	$(1 \text{ MeV}-20 \text{ MeV})$
	σ	Uniform	$(1 \text{ MeV}-10 \text{ MeV})$
PL	K	Log uniform	$(10^{-6}-10^6) [\text{cm}^{-2} \text{keV}^{-1} \text{s}^{-1}]$
	Γ_{ph}	Uniform	$(-2, 0)$
SBPL _{HE}	K_2	Log uniform	$(10^{-15}-10^{-3}) [\text{cm}^{-2} \text{keV}^{-1} \text{s}^{-1}]$
	α_2	Uniform	$(-2, 2)$
	$E_{b,2}$	Log uniform	$(1 \text{ GeV}-100 \text{ TeV})$
	β_2	Uniform	$(-10, 1)$

Note. We highlighted the second smoothly broken power law as SBPL_{HE} to distinguish it from the SBPL at low energies. In both cases, the scale parameter is fixed to 0.5. The pivot energy for the SBPL is fixed to its default value of 1 keV, while it is fixed to 1 GeV for the SBPL_{HE}.

Table 9
Parameters for the Best-fit Model

Parameter	Interval from T_0 (s)						
	280.6–290.6	290.6–300.6	300.6–325.6	325.6–340.6	340.6–355.6	355.6–380.6	380.6–435.6
$K_1 [\text{cm}^{-2} \text{keV}^{-1} \text{s}^{-1}]$	$0.729^{+0.006}_{-0.008}$	$0.319^{+0.002}_{-0.01}$	$0.135^{+0.001}_{-0.007}$	$0.1390^{+0.0002}_{-0.004}$	$0.1186^{+0.0004}_{-0.004}$	$(8.21^{+0.02}_{-0.1}) \times 10^{-2}$	$0.179^{+0.001}_{-0.003}$
α_1	$-1.499^{+0.002}_{-0.004}$	$-1.682^{+0.005}_{-0.002}$	$-1.926^{+0.001}_{-0.006}$	-1.79 ± 0.02	$-1.75^{+0.03}_{-0.02}$	$-1.24^{+0.2}_{-0.07}$	$-1.689^{+0.001}_{-0.004}$
$E_{b,1} [\text{MeV}]$	$0.90^{+0.06}_{-0.02}$	$1.16^{+0.2}_{-0.04}$	$2.121^{+0.4}_{-0.005}$	$0.10^{+0.02}_{-0.01}$	$(8 \pm 1) \times 10^{-2}$	$(2.0^{+0.1}_{-0.4}) \times 10^{-2}$	$0.677^{+0.1}_{-0.004}$
β_1	$-2.84^{+0.03}_{-0.09}$	$-2.78^{+0.02}_{-0.3}$	$-3.02^{+0.02}_{-5}$	$-2.36^{+0.04}_{-0.03}$	$-2.52^{+0.04}_{-0.05}$	$-2.273^{+0.01}_{-0.006}$	$-2.99^{+0.02}_{-0.2}$
$F [\text{cm}^{-2} \text{s}^{-1}]$	$0.52^{+0.6}_{-0.06}$	$0.198^{+0.1}_{-0.003}$	$0.254^{+0.1}_{-0.003}$	$0.29^{+0.06}_{-0.1}$	$0.23^{+0.2}_{-0.01}$	$(6.9^{+10.0}_{-0.9}) \times 10^{-2}$...
$\mu [\text{MeV}]$	$6.5^{+0.6}_{-5}$	$11.5^{+0.2}_{-2}$	$8.8^{+0.5}_{-1}$	3^{+3}_{-1}	$5.8^{+0.5}_{-4}$	$5.13^{+0.03}_{-3}$...
$\sigma [\text{MeV}]$	$5.3^{+2}_{-0.1}$	$2.0^{+1}_{-0.1}$	$3.2^{+1}_{-0.1}$	$4.0^{+1}_{-0.9}$	$3.5^{+2}_{-0.2}$	$2.2^{+1}_{-0.2}$...
$K_2 [10^{-11} \times \text{cm}^{-2} \text{keV}^{-1} \text{s}^{-1}]$	$3.1^{+0.9}_{-1}$	$2.0^{+0.8}_{-0.9}$	$1.84^{+0.06}_{-0.8}$	$2.12^{+0.02}_{-0.3}$	$1.4^{+0.4}_{-0.3}$	$0.28^{+0.03}_{-0.2}$	$0.5^{+0.3}_{-0.2}$
α_2	-1.3 ± 0.2	-1.5 ± 0.2	$-1.51^{+0.04}_{-0.2}$	$-1.2^{+0.3}_{-0.2}$	-1.5 ± 0.1	-1.4 ± 0.1	-1.4 ± 0.2
$E_{b,2} [\text{MeV}]$	$(1^{+2}_{-0.7}) \times 10^4$	$(2^{+8}_{-1}) \times 10^4$	$(2^{+6}_{-0.1}) \times 10^4$	$(4^{+3}_{-2}) \times 10^3$	$(1^{+1}_{-0.8}) \times 10^4$	$(7.0^{+10.0}_{-2}) \times 10^4$	$(2^{+4}_{-1}) \times 10^4$
β_2	$-2.35^{+0.02}_{-0.01}$	$-2.33^{+0.01}_{-0.04}$	$-2.32^{+0.02}_{-0.01}$	$-2.308^{+0.02}_{-0.002}$	$-2.32^{+0.01}_{-0.02}$	$-2.304^{+0.008}_{-0.04}$	$-2.252^{+0.002}_{-0.02}$

Note. For each time interval, we show the parameters for the SBPL+G+SBPL model, except for 380.6–435.6, where we show the ones for SBPL+SBPL, as the additional G did not significantly improve the fit.



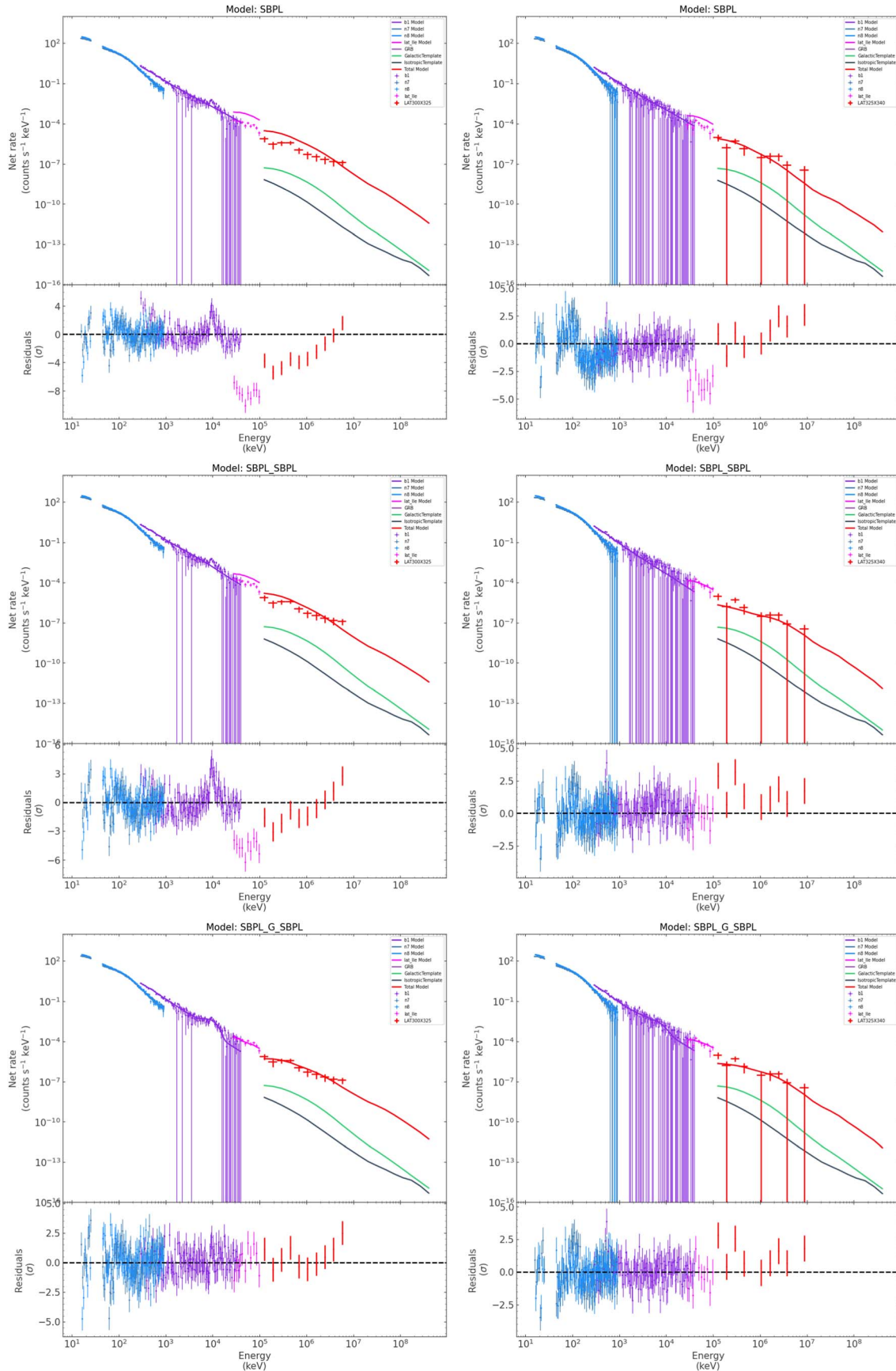


Figure 36. Count spectra (in counts $s^{-1} \text{ keV}^{-1}$) and residuals (in sigma units) for the $[T_0 + 300.6, T_0 + 325.6]$ (left) and $[T_0 + 325.6, T_0 + 340.6]$ (right) time intervals. From top to bottom: the SBPL, SBPL+SBPL, and SBPL+G+SBPL models.

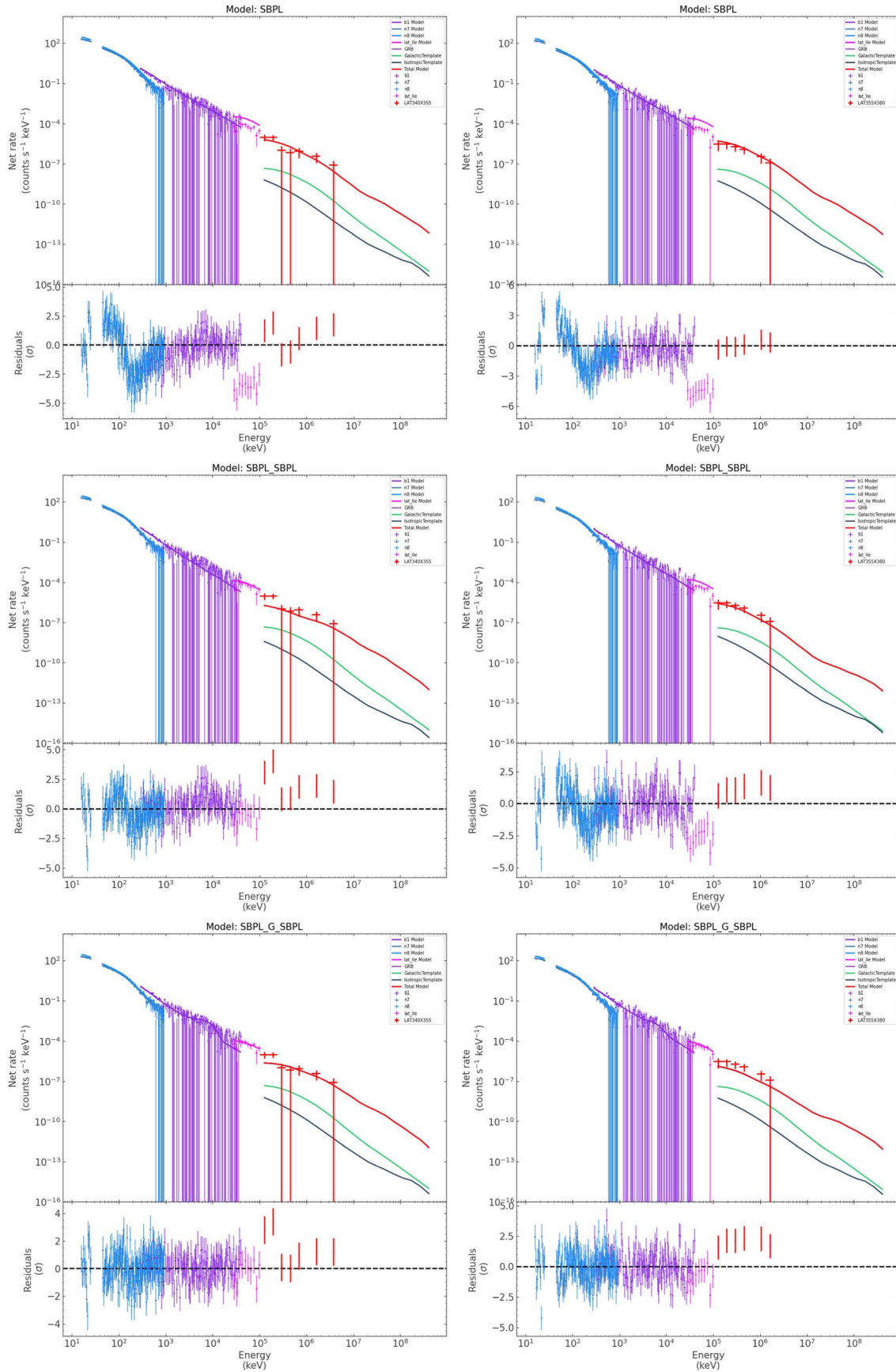


Figure 37. Count spectra (in counts $s^{-1} keV^{-1}$) and residuals (in sigma units) for the $[T_0 + 340.6, T_0 + 355.6]$ (left) and $[T_0 + 355.6, T_0 + 380.6]$ (right) time intervals. From top to bottom: the SBPL, SBPL+SBPL, and SBPL+G+SBPL models.

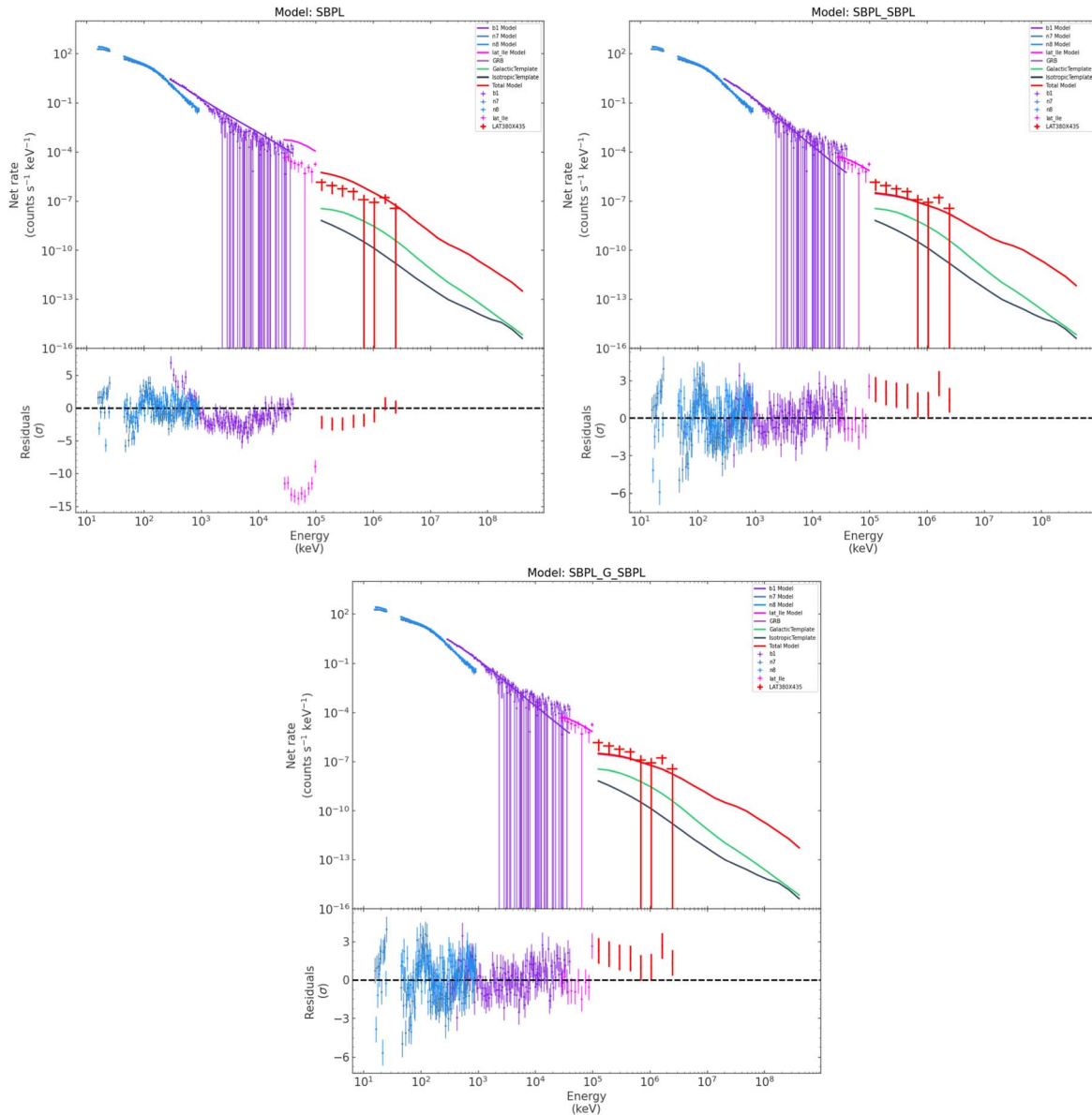


Figure 38. Count spectra (in $\text{counts s}^{-1} \text{keV}^{-1}$) and residuals (in sigma units) for the $[T_0 + 380.6, T_0 + 435.6]$ time interval. From top to bottom: the SBPL, SBPL+SBPL, and SBPL+G+SBPL models.

ORCID iDs

M. Axelsson <https://orcid.org/0000-0003-4378-8785>
M. Ajello <https://orcid.org/0000-0002-6584-1703>
M. Arimoto <https://orcid.org/0000-0003-1250-7872>
L. Baldini <https://orcid.org/0000-0002-9785-7726>
J. Ballet <https://orcid.org/0000-0002-8784-2977>
M. G. Baring <https://orcid.org/0000-0003-4433-1365>
C. Bartolini <https://orcid.org/0000-0001-7233-9546>
D. Bastieri <https://orcid.org/0000-0002-6954-8862>
J. Becerra Gonzalez <https://orcid.org/0000-0002-6729-9022>
R. Bellazzini <https://orcid.org/0000-0002-2469-7063>
E. Bissaldi <https://orcid.org/0000-0001-9935-8106>
R. D. Blandford <https://orcid.org/0000-0002-1854-5506>
R. Bonino <https://orcid.org/0000-0002-4264-1215>
P. Bruel <https://orcid.org/0000-0002-9032-7941>
S. Buson <https://orcid.org/0000-0002-3308-324X>
R. A. Cameron <https://orcid.org/0000-0003-0942-2747>

R. Caputo <https://orcid.org/0000-0002-9280-836X>
P. A. Caraveo <https://orcid.org/0000-0003-2478-8018>
E. Cavazzuti <https://orcid.org/0000-0001-7150-9638>
C. C. Cheung <https://orcid.org/0000-0002-4377-0174>
G. Chiaro <https://orcid.org/0009-0004-4271-3153>
N. Cibrario <https://orcid.org/0000-0003-3842-4493>
S. Ciprini <https://orcid.org/0000-0002-0712-2479>
G. Cozzolongo <https://orcid.org/0009-0001-3324-0292>
P. Cristarella Orestano <https://orcid.org/0000-0003-3219-608X>
M. Crnogorčević <https://orcid.org/0000-0002-7604-1779>
A. Cuoco <https://orcid.org/0000-0003-1504-894X>
S. Cutini <https://orcid.org/0000-0002-1271-2924>
F. D'Ammando <https://orcid.org/0000-0001-7618-7527>
S. De Gaetano <https://orcid.org/0000-0002-3358-2559>
N. Di Lalla <https://orcid.org/0000-0002-7574-1298>
R. Di Tria <https://orcid.org/0009-0007-1088-5307>
L. Di Venere <https://orcid.org/0000-0003-0703-824X>

- A. Domínguez  <https://orcid.org/0000-0002-3433-4610>
 S. J. Fegan  <https://orcid.org/0000-0002-9978-2510>
 E. C. Ferrara  <https://orcid.org/0000-0001-7828-7708>
 A. Fiori  <https://orcid.org/0000-0003-3174-0688>
 A. Franckowiak  <https://orcid.org/0000-0002-5605-2219>
 Y. Fukazawa  <https://orcid.org/0000-0002-0921-8837>
 S. Funk  <https://orcid.org/0000-0002-2012-0080>
 P. Fusco  <https://orcid.org/0000-0002-9383-2425>
 G. Galanti  <https://orcid.org/0000-0001-7254-3029>
 F. Gargano  <https://orcid.org/0000-0002-5055-6395>
 C. Gasbarra  <https://orcid.org/0000-0001-8335-9614>
 S. Germani  <https://orcid.org/0000-0002-2233-6811>
 F. Giacchino  <https://orcid.org/0000-0002-0247-6884>
 N. Giglietto  <https://orcid.org/0000-0002-9021-2888>
 M. Giliberti  <https://orcid.org/0009-0007-2835-2963>
 R. Gill  <https://orcid.org/0000-0003-0516-2968>
 F. Giordano  <https://orcid.org/0000-0002-8651-2394>
 M. Giroletti  <https://orcid.org/0000-0002-8657-8852>
 J. Granot  <https://orcid.org/0000-0001-8530-8941>
 D. Green  <https://orcid.org/0000-0003-0768-2203>
 I. A. Grenier  <https://orcid.org/0000-0003-3274-674X>
 S. Guiriec  <https://orcid.org/0000-0001-5780-8770>
 M. Hashizume  <https://orcid.org/0009-0003-4534-9361>
 E. Hays  <https://orcid.org/0000-0002-8172-593X>
 J. W. Hewitt  <https://orcid.org/0000-0002-4064-6346>
 D. Horan  <https://orcid.org/0000-0001-5574-2579>
 T. Kayanoki  <https://orcid.org/0000-0002-6960-9274>
 M. Kuss  <https://orcid.org/0000-0003-1212-9998>
 A. Laviro  <https://orcid.org/0000-0003-1521-7950>
 J. Li  <https://orcid.org/0000-0003-1720-9727>
 I. Liodakis  <https://orcid.org/0000-0001-9200-4006>
 F. Longo  <https://orcid.org/0000-0003-2501-2270>
 F. Loparco  <https://orcid.org/0000-0002-1173-5673>
 L. Lorusso  <https://orcid.org/0000-0002-2549-4401>
 B. Lott  <https://orcid.org/0000-0003-2186-9242>
 M. N. Lovellette  <https://orcid.org/0000-0002-0332-5113>
 P. Lubrano  <https://orcid.org/0000-0003-0221-4806>
 S. Maldera  <https://orcid.org/0000-0002-0698-4421>
 D. Malyshev  <https://orcid.org/0000-0002-9102-4854>
 A. Manfreda  <https://orcid.org/0000-0002-0998-4953>
 G. Martí-Devesa  <https://orcid.org/0000-0003-0766-6473>
 R. Martinelli  <https://orcid.org/0009-0004-0133-7227>
 I. Martinez Castellanos  <https://orcid.org/0000-0002-2471-8696>
 M. N. Mazziotta  <https://orcid.org/0000-0001-9325-4672>
 I. Mereu  <https://orcid.org/0000-0003-0219-4534>
 M. Meyer  <https://orcid.org/0000-0002-0738-7581>
 P. F. Michelson  <https://orcid.org/0000-0002-1321-5620>
 N. Mirabal  <https://orcid.org/0000-0002-7021-5838>
 W. Mitthumsiri  <https://orcid.org/0000-0002-3776-072X>
 T. Mizuno  <https://orcid.org/0000-0001-7263-0296>
 P. Monti-Guarnieri  <https://orcid.org/0000-0002-1434-1282>
 M. E. Monzani  <https://orcid.org/0000-0002-8254-5308>
 T. Morishita  <https://orcid.org/0009-0001-2227-3507>
 A. Morselli  <https://orcid.org/0000-0002-7704-9553>
 I. V. Moskalenko  <https://orcid.org/0000-0001-6141-458X>
 M. Negro  <https://orcid.org/0000-0002-6548-5622>
 N. Omodei  <https://orcid.org/0000-0002-5448-7577>
 M. Orienti  <https://orcid.org/0000-0003-4470-7094>
 E. Orlando  <https://orcid.org/0000-0001-6406-9910>
 D. Paneque  <https://orcid.org/0000-0002-2830-0502>
 G. Panzarini  <https://orcid.org/0000-0002-2586-1021>
 M. Persic  <https://orcid.org/0000-0003-1853-4900>
 M. Pesce-Rollins  <https://orcid.org/0000-0003-1790-8018>
 V. Petrosian  <https://orcid.org/0000-0002-2670-8942>
 R. Pillera  <https://orcid.org/0000-0003-3808-963X>
 F. Piron  <https://orcid.org/0000-0001-6885-7156>
 T. A. Porter  <https://orcid.org/0000-0002-2621-4440>
 G. Principe  <https://orcid.org/0000-0003-0406-7387>
 J. L. Racusin  <https://orcid.org/0000-0002-4744-9898>
 S. Rainò  <https://orcid.org/0000-0002-9181-0345>
 R. Rando  <https://orcid.org/0000-0001-6992-818X>
 B. Rani  <https://orcid.org/0000-0001-5711-084X>
 M. Razzano  <https://orcid.org/0000-0003-4825-1629>
 S. Razzaque  <https://orcid.org/0000-0002-0130-2460>
 A. Reimer  <https://orcid.org/0000-0001-8604-7077>
 O. Reimer  <https://orcid.org/0000-0001-6953-1385>
 F. Ryde  <https://orcid.org/0000-0002-9769-8016>
 M. Sánchez-Conde  <https://orcid.org/0000-0002-3849-9164>
 P. M. Saz Parkinson  <https://orcid.org/0000-0001-6566-1246>
 D. Serini  <https://orcid.org/0000-0002-9754-6530>
 C. Sgrò  <https://orcid.org/0000-0001-5676-6214>
 V. Sharma  <https://orcid.org/0000-0002-4394-4138>
 E. J. Siskind  <https://orcid.org/0000-0002-2872-2553>
 G. Spandre  <https://orcid.org/0000-0003-0802-3453>
 P. Spinelli  <https://orcid.org/0000-0001-6688-8864>
 D. J. Suson  <https://orcid.org/0000-0003-2911-2025>
 H. Tajima  <https://orcid.org/0000-0002-1721-7252>
 D. Tak  <https://orcid.org/0000-0002-9852-2469>
 J. B. Thayer  <https://orcid.org/0000-0002-9051-1677>
 D. F. Torres  <https://orcid.org/0000-0002-1522-9065>
 J. Valverde  <https://orcid.org/0000-0002-8090-6528>
 G. Zaharijas  <https://orcid.org/0000-0001-8484-7791>
 S. Lesage  <https://orcid.org/0000-0001-8058-9684>
 M. S. Briggs  <https://orcid.org/0000-0003-2105-7711>
 E. Burns  <https://orcid.org/0000-0002-2942-3379>
 S. Bala  <https://orcid.org/0000-0002-6657-9022>
 P. N. Bhat  <https://orcid.org/0000-0001-7916-2923>
 W. H. Cleveland  <https://orcid.org/0009-0003-3480-8251>
 S. Dalessi  <https://orcid.org/0000-0003-1835-570X>
 C. de Barra  <https://orcid.org/0009-0003-7797-1243>
 R. Hamburg  <https://orcid.org/0000-0003-0761-6388>
 B. A. Hristov  <https://orcid.org/0000-0001-9556-7576>
 D. Kocevski  <https://orcid.org/0000-0001-9201-4706>
 C. M. Hui  <https://orcid.org/0000-0002-0468-6025>
 B. Mailyan  <https://orcid.org/0000-0002-2531-3703>
 C. Malacaria  <https://orcid.org/0000-0002-0380-0041>
 S. McBreen  <https://orcid.org/0000-0002-1477-618X>
 S. Poolakkil  <https://orcid.org/0000-0002-6269-0452>
 O. J. Roberts  <https://orcid.org/0000-0002-7150-9061>
 L. Scotton  <https://orcid.org/0000-0002-0602-0235>
 P. Veres  <https://orcid.org/0000-0002-2149-9846>
 A. von Kienlin  <https://orcid.org/0000-0002-0221-5916>
 C. A. Wilson-Hodge  <https://orcid.org/0000-0002-8585-0084>
 J. Wood  <https://orcid.org/0000-0001-9012-2463>

References

- Abbasi, R., Ackermann, M., Adams, J., et al. 2023, *ApJL*, 946, L26
 Abdalla, H., Adam, R., Aharonian, F., et al. 2019, *Natur*, 575, 464
 Abdollahi, S., Acero, F., Ackermann, M., et al. 2020, *ApJS*, 247, 33
 Abe, H., Abe, S., Acciari, V. A., et al. 2024, *MNRAS*, 527, 5856
 Ackermann, M., Asano, K., Atwood, W. B., et al. 2010, *ApJ*, 716, 1178

- Ackermann, M., Ajello, M., Albert, A., et al. 2012, *ApJS*, **203**, 4
- Ackermann, M., Ajello, M., Asano, K., et al. 2014, *Sci*, **343**, 42
- Ackermann, M., Ajello, M., Albert, A., et al. 2016, *PhRvL*, **116**, 151105
- Ackermann, M., Ajello, M., Baldini, L., et al. 2018, *ApJS*, **237**, 32
- Agostinelli, S., Allison, J., Amako, K., et al. 2003, *NIMPA*, **506**, 250
- Aharonian, F., Benkhali, F. A., Aschersleben, J., et al. 2023, *ApJL*, **946**, L27
- Ai, S., & Gao, H. 2023, *ApJ*, **944**, 115
- Ajello, M., Albert, A., Allafort, A., et al. 2014, *ApJ*, **789**, 20
- Ajello, M., Arimoto, M., Axelsson, M., et al. 2019, *ApJ*, **878**, 52
- Ajello, M., Arimoto, M., Axelsson, M., et al. 2020, *ApJ*, **890**, 9
- Aliu, E., Aune, T., Barnacka, A., et al. 2014, *ApJL*, **795**, L3
- Allison, J., Amako, K., Apostolakis, J., et al. 2006, *ITNS*, **53**, 270
- An, Z.-H., Antier, S., Bi, X.-Z., et al. 2023, arXiv:2303.01203
- Arimoto, M., Asano, K., Tachibana, Y., & Axelsson, M. 2020, *ApJ*, **891**, 106
- Atri, P., An, T., Giroletti, M., et al. 2022, GCN, **32907**, 1
- Atwood, W., Albert, A., Baldini, L., et al. 2013, arXiv:1303.3514
- Atwood, W. B., Abdo, A. A., Ackermann, M., et al. 2009, *ApJ*, **697**, 1071
- Ayala, H. & HAWC Collaboration 2022, GCN, **32683**, 1
- Band, D., Matteson, J., Ford, L., et al. 1993, *ApJ*, **413**, 281
- Bissaldi, E., Omodei, N., Kerr, M. & Fermi-LAT Team 2022, GCN, **32637**, 1
- Broderick, A. E., Chang, P., & Frommer, C. 2012, *ApJ*, **752**, 22
- Burns, E., Svinkin, D., Fenimore, E., et al. 2023a, *ApJL*, **946**, L31
- Burns, E., Svinkin, D., Fenimore, E., et al. 2023b, *ApJL*, **946**, L31
- Cao, Z., Aharonian, F., An, Q., et al. 2023a, *Sci*, **380**, 1390
- Cao, Z., Aharonian, F., An, Q., et al. 2023b, *SciA*, **9**, ead2778
- Castro-Tirado, A. J., Sanchez-Ramirez, R., Hu, Y. D., et al. 2022, GCN, **32686**, 1
- Corsi, A., Guetta, D., & Piro, L. 2010, *ApJ*, **720**, 1008
- Da Vela, P., Martí-Devesa, G., Saturni, F. G., et al. 2023, *PhRvD*, **107**, 063030
- de Ugarte Postigo, A., Izzo, L., Pugliese, G., et al. 2022, GCN, **32648**, 1
- Dichiara, S., Gropp, J. D., Kennea, J. A., et al. 2022, GCN, **32632**, 1
- Dzhappuev, D. D., Afshokov, Y. Z., Dzaparova, I. M., et al. 2022, ATel, **15669**, 1
- Feroz, F., Hobson, M. P., & Bridges, M. 2009, *MNRAS*, **398**, 1601
- Finke, J. D., Razzaque, S., & Dermer, C. D. 2010, *ApJ*, **712**, 238
- Frederiks, D., Svinkin, D., Lysenko, A. L., et al. 2023, *ApJL*, **949**, L7
- Fulton, M. D., Smartt, S. J., Rhodes, L., et al. 2023, *ApJL*, **946**, L22
- Ghirlanda, G., Nappo, F., Ghisellini, G., et al. 2018, *A&A*, **609**, A112
- Ghisellini, G., Ghirlanda, G., Nava, L., & Celotti, A. 2010, *MNRAS*, **403**, 926
- Ghisellini, G., Tavecchio, F., & Chiaberge, M. 2005, *A&A*, **432**, 401
- Giroletti, M., Giovannini, G., Feretti, L., et al. 2004, *ApJ*, **600**, 127
- H.E.S.S. Collaboration, Abdalla, H., Aharonian, F., et al. 2021, *Sci*, **372**, 1081
- Hakkila, J., & Preece, R. D. 2014, *ApJ*, **783**, 88
- Huang, Y., Hu, S., Chen, S., et al. 2022, GCN, **32677**, 1
- Jeffreys, H. 1939, *Theory of Probability* (Oxford: Oxford Univ. Press)
- Kann, D. A., Agayeva, S., Aivazyan, V., et al. 2023, *ApJL*, **948**, L12
- KM3NeT Collaboration 2022, GCN, **32741**, 1
- Kobayashi, S. 2000, *ApJ*, **545**, 807
- Kumar, P., & Barniol Duran, R. 2009, *MNRAS*, **400**, L75
- Kumar, P., & Panaitescu, A. 2000, *ApJL*, **541**, L51
- Laing, R. A., & Bridle, A. H. 2002, *MNRAS*, **336**, 328
- Laskar, T., Alexander, K. D., Margutti, R., et al. 2023, *ApJL*, **946**, L23
- Lesage, S., Veres, P., Roberts, O. J., et al. 2022, GCN, **32642**, 1
- Lesage, S., Veres, P., Briggs, M. S., et al. 2023, *ApJL*, **952**, L42
- Levan, A. J., Cenko, S. B., Perley, D. A., & Tanvir, N. R. 2013, GCN, **14455**, 1
- Li, T. P., & Ma, Y. Q. 1983, *ApJ*, **272**, 317
- MAGIC Collaboration, Acciari, V. A., Ansoldi, S., et al. 2019, *Natur*, **575**, 455
- Meegan, C., Lichti, G., Bhat, P. N., et al. 2009, *ApJ*, **702**, 791
- Meliani, Z., Keppens, R., & Giacomazzo, B. 2008, *A&A*, **491**, 321
- Murase, K., Zhang, B., Takahashi, K., & Nagataki, S. 2009, *MNRAS*, **396**, 1825
- Nakar, E., & Piran, T. 2004, *MNRAS*, **353**, 647
- Nappo, F., Ghisellini, G., Ghirlanda, G., et al. 2014, *MNRAS*, **445**, 1625
- Negro, M., Di Lalla, N., Omodei, N., et al. 2023, *ApJL*, **946**, L21
- Neronov, A., & Semikoz, D. V. 2009, *PhRvD*, **80**, 123012
- Norris, J. P., Bonnell, J. T., Kazanas, D., et al. 2005, *ApJ*, **627**, 324
- O'Connor, B., Troja, E., Ryan, G., et al. 2023, *SciA*, **9**, eadi1405
- Omodei, N., Bruel, P., Bregeon, J., et al. 2022, GCN, **32760**, 1
- Pe'er, A., & Zhang, B. 2024, *ApJL*, **973**, L51
- Pelassa, V., Preece, R., Piron, F., et al. 2010, arXiv:1002.2617
- Pillera, R., Bissaldi, E., Omodei, N., et al. 2022, GCN, **32658**, 1
- Piron, F., Longo, F., Axelsson, M., et al. 2019, GCN, **25574**, 1
- Poolakkil, S., Preece, R., Fletcher, C., et al. 2021, *ApJ*, **913**, 60
- Racusin, J. L., Liang, E. W., Burrows, D. N., et al. 2009, *ApJ*, **698**, 43
- Ravasio, M. E., Oganessian, G., Ghirlanda, G., et al. 2018, *A&A*, **613**, A16
- Ravasio, M. E., Salafia, O. S., Oganessian, G., et al. 2024, *Sci*, **385**, 452
- Razzaque, S. 2010, *ApJL*, **724**, L109
- Razzaque, S., Mészáros, P., & Zhang, B. 2004, *ApJ*, **613**, 1072
- Sari, R., & Piran, T. 1999, *ApJ*, **520**, 641
- Scargle, J. D., Norris, J. P., Jackson, B., & Chiang, J. 2013, *ApJ*, **764**, 167
- Schnoor, P. W., Nicholson, P., & Welch, D. L. 2022, GCN, **32744**, 1
- Tak, D., Omodei, N., Uhm, Z. L., et al. 2019, *ApJ*, **883**, 134
- Tak, D., Uhm, Z. L., Paek, G. S. H., et al. 2025, *ApJ*, **978**, 29
- Tavani, M., Piano, G., Bulgarelli, A., et al. 2023, *ApJL*, **956**, L23
- Tiago, A., Pintore, F., Vaia, B., et al. 2023, *ApJL*, **946**, L30
- Vasilopoulos, G., Karavola, D., Stathopoulos, S. I., & Petropoulou, M. 2023, *MNRAS*, **521**, 1590
- Vianello, G., Gill, R., Granot, J., et al. 2018, *ApJ*, **864**, 163
- Vianello, G., Omodei, N. & Fermi/LAT collaboration 2015a, arXiv:1502.03122
- Vianello, G., Lauer, R. J., Younk, P., et al. 2015b, arXiv:1507.08343
- Williams, M. A., Kennea, J. A., Dichiara, S., et al. 2023, *ApJL*, **946**, L24
- Wood, M., Caputo, R., Charles, E., et al. 2017, *ICRC (Busan)*, **35**, 824
- Xia, Z.-Q., Wang, Y., Yuan, Q., & Fan, Y.-Z. 2022, GCN, **32748**, 1
- Xia, Z.-Q., Wang, Y., Yuan, Q., & Fan, Y.-Z. 2024, *NatCo*, **15**, 4280
- Zhang, B. 2019, *The Physics Of Gamma-Ray Bursts* (Cambridge: Cambridge Univ. Press)
- Zhang, B., Wang, X.-Y., & Zheng, J.-H. 2024, *JHEAp*, **41**, 42
- Zhang, Y.-Q., Xiong, S.-L., Mao, J.-R., et al. 2024, *SCPMA*, **67**, 289511